Fakultät für Physik und Astronomie

Ruprecht-Karls-Universität Heidelberg

Diplomarbeit

im Studiengang Physik

vorgelegt von

Sabrina Roßberger

aus Wiesbaden

2010

Vielfarben Lokalisationsmikroskopie mit einem einzelnen Anregungs-Laser unter Verwendung Infraroter Fluorophore

Die Diplomarbeit wurde von Sabrina Roßberger
ausgeführt am
Kirchhoff Institut für Physik Heidelberg
unter der Betreuung von

Herrn Prof. Christoph Cremer

sowie

Herrn Associate Prof. Christian Soeller

Fakultät für Physiologie, Universität Auckland (Neuseeland)

Department of Physics and Astronomy

University of Heidelberg

Diploma Thesis

in physics

submitted by

Sabrina Roßberger

born in Wiesbaden

2010

Multi-color Localization Microscopy with a Single Excitation Laser Line using Far-Red Dyes

This diploma thesis has been carried out by Sabrina Roßberger
at the
Kirchhoff Institute for Physics Heidelberg
under the supervision of

Herrn Prof. Christoph Cremer

and

Herrn Associate Prof. Christian Soeller

Department of Physiology, University of Auckland (New Zealand)

Zusammenfassung

Erst kürzlich wurde gezeigt, dass konventionelle fluoreszierende Moleküle für hochauflösende Mikroskopie mittels Einzelmolekül-Detektion genutzt werden können. Jedoch traten bisher einige Schwierigkeiten bei der Verwendung dieser Fluorophore auf. In dieser Arbeit wird eine Charakterisierung des photophysikalische Verhaltens der kommerziell erhältlichen infraroten Alexa Fluorophore (647, 680, 700, 750), welche an Antikörper gebunden sind, durchgeführt. Diese verfügen über einige Vorteile gegenüber anderen Fluorophoren, die in letzter Zeit verwendet wurden (z.Bsp. Alexa 488 and GFP). Die Hintergrund-Fluoreszenz wird deutlich reduziert und es ist relativ einfach eine passende chemischen Umgebung für alle infraroten Alexa Fluorophore herzustellen. Zusätzlich können sie alle mit der gleichen 671 nn Laser Wellenlänge angeregt werden. Diese Eigenschaften der infraroten Fluorophore werden ausgenutzt, um mehrfarbige Bilder mit der erst kürzlich entwickelten Methode der reversiblen Fotobleichungsmikroskopie aufzunehmen. Trotz der längeren Wellenlänge ist es möglich, Auflösungen von ca. 30 nm (FWHM) zu erreichen, welche mit theoretischen Lokalisierungsgenauigkeiten verglichen werden. Darüber hinaus werden Methoden vorgestellt, um die chromatischen Verschiebungen zu korrigieren. Die Software Analyse und der Mikroskopie Versuchsaufbau, welche es ermöglichen zwei verschiedene Farben gleichzeitig mit nur einem Anregungslaser aufzunehmen, werden vorgestellt. Schließlich werden Anwendungen von Zweifarben-Lokalisations-Mikroskopie in biologischen Proben präsentiert, welche die relative Verteilung von β-Tubulin, Caveolin-3, Natrium-Calcium-Austauscher und Ryanodin-Rezeptoren in fixierten kardialen Myozyten illustrieren.

Abstract

It has recently been shown that conventional fluorescent dyes can be used to achieve super-resolution by single-molecule localization. Some difficulties still remain with these dyes. In this thesis a characterization of the photophysical behavior of the commercially available antibody linked far-red Alexa dyes (647, 680, 700, 750), is conducted. They provide several advantages compared to other dyes used in the past (e.g. Alexa 488 or GFP) in terms of background reduction and a relatively easy handling of the chemical environment. All these dyes can be excited with the same laser wavelength and are exploited in order to perform two color imaging with the recently developed reversible photobleaching microscopy method with single laser excitation. Despite the longer wavelength, a resolution of approximately 30nm (FWHM) is achieved, which was compared with theoretical predicted localization precisions. Moreover methods to correct the chromatic shifts are presented. Software analysis and the microscope setup, which enables simultaneous imaging of two colors with a single laser excitation wavelength, are explained and finally several applications for two color imaging in biological samples are demonstrated. We present two color images showing the relative distributions of β-tubulin, caveolin-3, sodium-calcium-exchanger and ryanodine receptors in fixed cardiac myocytes.

Contents

Chapter 1

Introduction

The intention in this thesis was to improve the method RPM in order to perform multi-color imaging. This method, based on the idea of fluorescence microscopy, is heavily dependent on the characteristics of the fluorescent dyes used as markers in a biological sample.

Research in biology, physiology and medical science is often heavily dependent on gaining information about structures in cells on the molecular level, their location, functionality and also processes associated with these. Therefore one of the main fields in biophysics and medical physics deals with the development and improvement of imaging techniques. For visualizing structures in the nanometer range microscopy has been proven to be a successful technique.

Several different microscopy techniques have been developed in the past. Diffraction as a nature of light was long believed to be an absolute resolution limit for far field microscopy and was first formulated by Ernst Abbe([Abbe, 1873]):

$$d = \frac{\lambda}{2 \cdot NA} \tag{1.1}$$

In first place it is obvious that resolution is linearly dependent on the wavelength. Therefore classically a lateral resolution of $\backsim$ 200 nm and an axial resolution of $\backsim$ 500 nm are achievable while using visible light. As a result approaches like x-ray and electron microscopy have been invented, which benefit from the very small wavelength of x-rays and electrons compared to visible light. As a result x-ray microscopy

can provide a resolution in the atomic range and electron microscopy theoretically is able to resolve structures having a size of $3.7*10^{-12}$ m = 3.7 pm using a electron energies of 100 keV. This is enough to visualize for example protein distributions in cells ([Koster and Klumperman, 2003]). First attempts of imaging biological samples with electron microscopes have already taken place in 1934 ([Marton, 1934]) and lots of interesting biological discoveries have been done by using electron microscopy. Remaining issues with this technique include the high effort in preparing the sample, the impossibility to use this technique in-vivo and the difficulty of achieving a specific contrast. Disadvantages of x-ray microscopy are the difficulty of focusing the rays, because most lenses have a refractive of nearly one for x-rays. Therefore complex manufactured lenses (Fresnel lenses) are required and in-vivo observations are difficult, because of the biological damage occurring during the irradiation.

Fluorescence microscopy seemed to be the a useful method in order to image biological samples. This method relies on specific labeling of a target within a cell with fluorescent tags. Several different labeling methods have been proven to be successful in fluorescence microscopy. Fluorescence-In-Situ-Hybridization (FISH), immunolabeling, DAPI and Wheat Germ Agglutinin (WGA) are only a very few of those. DAPI binds to DNA whereas WGA binds to membrane sugar residues respectively. The FISH method is designed for labeling specific DNA sequences. After denaturation DNA molecules carrying a fluorescent tag bind specifically to a DNA sequence of interest. Using an appropriate light source to excite the tag will show the position of the DNA sequence ([Levsky and Singer, 2003]). Immunolabeling, an also widely used method, is based on fluorescent tags, which are mounted on antibodies. Those will bind specifically to the target of interest, usually another antibody, which is bound to a specific protein structure (see [Alberts et al., 2008], chapter 9: Visualizing Cells). These methods are not as invasive as for example the sample preparation in electron microscopy, have the potential to be used for in-vivo imaging and fluorescence microscopy has the potential to 'break' the diffraction limit by various changes ([Hell, 2007],[Bates et al., 2008]).

Due to the numerous practical advantages there is an obvious demand for fluorescence imaging below the diffraction limit. As diffraction is a internal characteristic of light, it is not possible to 'break' the Abbe-limit but to circumvent it. Having this idea in mind various different so called 'super-resolution' imaging techniques

have been developed. As this thesis will deal with far-field microscopy the following overview of imaging techniques will be limited to far-field microscopes.
At first several attempts have improved the resolution, but are still limited by diffraction. An example is the confocal microscopy ([Wilhelm et al.,]), which illuminates only a point like area of the sample due to an inserted pinhole into the beam path. According to this the sample needs to be scanned and a later reconstruction of the measured intensities for the single points shows the whole image. Structured Illumination Microscopy (SIM) narrows the PSF by using two opposite located laser beams, which interfere with each other and thereby produce a inhomogeneous excitation pattern, which interacts with the information gained of the sample ([Gustafsson, 2000]). Thus the frequency range is extended and results finally in a sharper PSF ([Bates et al., 2008]). The resolution is only improved by a factor two, which is not enough to study protein distributions. A variation of SIM is Spatially Modulated Illumination (SMI), which is extended with a second objective and provides no better resolution than the classical limit, but can be a successful method for size and distance measurements between molecules. 4Pi, a variation of the confocal microscope, attempts another idea ([Hell and Stelzer, 1992a], [Hell and Stelzer, 1992b]). Instead of one objective, two objectives placed opposite of each other, increase the Numerical Aperture (NA) and therefore considerably the resolution (see equation 1.1).
The methods explained in this passage improve the resolution by performing changes in the microscope setup, but they are still limited by diffraction and are not able to provide a resolution below $\backsim 100\,\mathrm{nm}$.

There are two main approaches, which yield true super-resolution: The first one deals with modifying the Point Spread Function (PSF) by using non-linear excitation whereas the second one is based on temporal and spectral separation and detection of single molecule events.

Two-photon excitation benefits from reducing out-of focus fluorescence. Only in the focus area high enough photon densities are provided to achieve a multi photon excitation. But this technique also improves the resolution only by a factor 2 ([Denk et al., 1990]). A good example of non-linear PSF engineering is Stimulated Emission Depletion fluorescence microscopy (STED). Here the diffraction limit is circumvented by reducing the PSF with a certain trick: In brief, the excitation laser

pulse is followed immediately by a second 'donut-shaped' laser pulse, which depletes the excited state by stimulated emission except for a very small area in the middle. As a result the fluorescent light detected arises from an area much smaller than the classic resolution limit ([Klar et al., 2000], [Hell and Wichmann, 1994]). The further improved version of SIM is Saturated Structured Illumination Microscopy (SSIM), which is also worth a mention it in this context ([Heintzmann et al., 2002], [Gustafsson, 2005]). Saturating intensities are used to excite the fluorophores, which results in in excitation pattern of very high frequencies. Theoretically there is no limit for the frequency and therefore the resolution can be improved significantly. STED and as well SSIM provide a theoretically unlimited resolution.

Temporal and spectral separation and detection of single molecule events profits from a slightly different approach. Structures of interest can be labeled with fluorescent dyes, which bind specifically. These dyes still have a diffraction limited PSF, but this technique excites only a very sparse number of the photo-switchable dyes at the same time. The fluorophores are in a 'dark' (non-fluorescent) state in the beginning. By illuminating the sample with a pulsed laser or by using lower laser intensities only a few fluorophores can be excited at the same time and which finally results in the bleaching of the fluorophores. The detected diffraction limited PSF is not overlapping with any other PSF and therefore the exact location of the dye can be evaluated by an appropriate fitting algorithm, which estimates the centroid of the PSF. The actual image has to be reconstructed out of all fluorophore positions detected over time. The result is a high-resolution image with a resolution on the molecular level. This principle is known as Stochastic Optical Reconstruction Microscopy (STORM, [Rust et al., 2006]) or Photoactivated Localization Microscopy (PALM, fPALM, [Betzig et al., 2006], [Hess et al., 2006]). PALM and STORM do not attempt to sharpen the PSF, but to separate the PSF's of the fluorescent dyes over time. A very recently developed variation of STORM is a method called Reversible Photobleaching Microscopy (RPM) or dSTORM. These methods relies on fluorophores, which are able to recover from bleaching. High illumination intensities push fluorophores into a 'dark-state' from where they can recover very slowly. The result is also a limited number of fluorophores, which are fluorescent at the same time. Image reconstructions are comparable to STORM and PALM. Recently structures down to $\backsim$ 30 nm have been resolved with this technique ([Baddeley et al., 2009b], [Heilemann et al., 2008], [Huang et al., 2008],

[Fölling et al., 2008]).
Spectral Precision Distance Microscopy (SPDM) is a method using fluorescence light microscopy and is also relying on single molecule detection, which enables measurements of distances and angles below the diffraction limit. Molecules labeled with different fluorescent tags can be separated in a multi-channel detection. The center calculation of a fitted Gaussian to the PSF provides a resolution far below the limit ([Lemmer et al., 2008]).

From the biological point of view a motivation for this thesis was found in statistics, which claim that heart diseases have become a mayor cause of death. In 2008 43 % of all cases of death occurring in Germany ([Bundesamt, 2009]) were directly caused by cardivascular diseases. According to a survey by the World Health Organization nearly 50 % of people did die of cardiovascular diseases in the industrial nations and it is also the leading cause of death worldwide ($\backsim$ 12 %, [WHO, 2009]). In order to treat these diseases fundamental knowledge about heart cells is indispensable. Based on information gained in healthy heart cells, changes in structure and functionality can be extracted. For this purpose it is useful to be able to visualize different protein distributions within the cell at the same time in order to work out their correlations to each other as well as any possible interaction. The origin of the changes in the cell can be investigated in further experiments and as a result treatment for several heart diseases can be developed. Without fundamental research improved medical treatment won't be possible.

Chapter 2

Background

2.1 Physics of Imaging

2.1.1 Important Characteristics of Light

As first recognized by Abbe ([Abbe, 1873]) diffraction is the limiting factor for resolution. It is an internal characteristic of imaging with light, that is important when considering applications in order to achieve higher resolutions in microscopy. Diffraction describes the behavior of a electromagnetic wave (em-wave), which propagates in space or encounters a barrier and which alters the amplitude or phase of the light wave. The electric and the magnetic field strength E and B are changing over time, which is mathematically described by Maxwell's equations. Therefore the wave changes its original way of propagation, which results in secondary waves and these form a new shape of the wavefront (Huygens' principle). Light can therefore be observed in regions, which are impossible to reach in geometrical optics.
The superposition principle states that all amplitudes of the partial waves in a certain point are added. The superposition of partial waves is called interference. Constructive or destructive interference lead to an energy-density distribution of alternating maxima and minima, which is known as the diffraction pattern of a wave. A wavefront, which impinges a single slit, is the easiest example to explain interference based on the classical wave theory. Each point in the slit is the source of a spherical wavefront, which interfere with each other by adding the amplitudes of the electromagnetic wave in each point. The intensity distribution in the image plane is then given by the following equation, which depends on the diffraction angle Θ (see figure 2.1):

$$I(\Theta) = I_0 \frac{\sin^2(x)}{x^2} \; with \; x = \frac{\pi \cdot b}{\lambda} \sin(\Theta) \tag{2.1}$$

with b describing the slit width and λ the wavelength. A derivation of the equation can be found in [Demtröder, 2004] (chapter 8) or in [Hecht, 1998]. The distribution I(Θ) is zero (minimum) when $\sin(\Theta) = \lambda/b$ is fulfilled. Figure 2.1 shows the geometrical relations for a em-wave encountering a single slit. For destructive interference the diffracted light is divided into two halves (see figure 2.1). For each partial wave in one half a partial wave in the other half can be found, which have a path difference of exactly $\Delta s = \lambda/2$. They annihilate with each other and a intensity minimum is detected in the image plane. For constructive interference the diffracted light can be divided into three parts. Two parts annihilate with each other, whereas the third part of the wave is the maximum detected in the image plane. The result is an alternating intensity distribution in the image plane consisting of maxima ($\Delta s = k \cdot \lambda$ with $k \in \mathbb{N}$) and minima ($\Delta s = (2k-1) \cdot \frac{\lambda}{2}$ with $k \in \mathbb{N}$), which is depending on the diffraction angle Θ (see figure 2.1). A characteristic diffraction pattern can be observed (figure 2.1, right diagram). Most of the intensity can be found in the central maximum (Θ=0). The central maximum tends to be narrower, when the slit gets broader or the wavelength gets smaller.

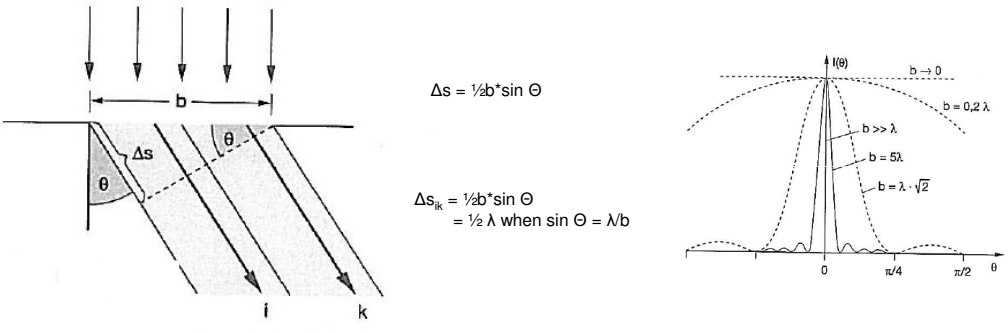

Figure 2.1: The geometrical relations for a em-wave encountering a single slit are demonstrated ([Demtröder, 2004]). b is the width of the slit and Δs is the optical path difference between two partial waves propagating under the same angle Θ. The trigonometrical relations are evaluated. The wave can be divided into partial waves, which fulfill the requirements for constructive and destructive interference (see text). Here the mathematical derivation for destructive interference is shown. The resulting characteristic interference pattern consisting of maxima and minima is also illustrated.

A circular aperture (e.g. lens in the microscope) with a radius R has a rotation-symmetric intensity distribution I(Θ) in the lateral directions (x-y). A derivation can be found in [Demtröder, 2004] (chapter 10):

$$I(\Theta) = I_0 \left(\frac{2 \cdot J_1(x)}{x} \right)^2 \; with \; x = \frac{2\pi R}{\lambda} \sin(\Theta) \tag{2.2}$$

J_1(x) is the Bessel function of first order. The intensity distribution in the axial direction (z) is slightly different:

$$I(\Theta) = I_0 \left(\frac{\sin\left(\frac{x}{4}\right)}{\frac{x}{4}} \right)^2 \tag{2.3}$$

The equation for the axial intensity distribution has a broader maximum of zero order than in the lateral directions, which leads to less resolution in the axial direction. The definition of resolution will be explained in the next chapter.

The diffraction pattern for an arbitrary shape of the aperture can be calculated based on the Kirchhoff-Fresnel diffraction integral. Figure 2.2 (left illustration) shows a random aperture σ at the position z = 0 and the image plane at position z_0. Assuming an incident wave with an amplitude of $E_\sigma = E_0(x, y) \exp(-i\phi(x, y))$, each infinitesimal element dσ is sending out spherical waves, which contribute a part of the energy detected in a point P(x',y') in the image plane:

$$dE_P = C \cdot \frac{E_\sigma \cdot d\sigma}{r} \cdot \exp(-ikr), \tag{2.4}$$

with C = proportionality factor. The total amplitude in P is then:

$$E_P = \int\int C \cdot E_\sigma \frac{\exp(-ikr)}{r} \, dxdy \tag{2.5}$$

This is the Kirchhoff-Fresnel diffraction integral. Two limiting cases can be derived, which are the near-field approximation (z small, Fresnel diffraction) and far-field approximation (z big, Fraunhofer diffraction). When z_0>>b, r in the denominator can be approximated by z_0. The exponent can be developed in a Taylor expansion:

$$r = \sqrt{z_0^2 + (x - x')^2 + (y - y')^2)} = z_0 \left(1 + \frac{(x - x')^2}{2z_0^2} + \frac{(y - y')^2}{2z_0^2} + ...\right) \quad (2.6)$$

Further simplifications can be proceeded if $z_0 >> b^2/\lambda$, which simplifies the exponent as follows:

$$r \approx z_0 \left(1 + \frac{xx'}{z_0^2} + \frac{yy'}{z_0^2} + \frac{x'^2 + y'^2}{2z_0^2}\right) \quad (2.7)$$

With $C=(1/i\lambda)$ this derivation the resulting integral is:

$$E_P = \frac{\exp(-ikz_0)}{i\lambda z_0} \exp(\frac{-i\pi}{\lambda z_0}(x'^2+y'^2)) \int\int E(x,y) \exp(\frac{-ik}{z_0}(xx'+yy'))\, dx\, dy \quad (2.8)$$

which describes the Fraunhofer diffraction in a far-field approximation. In the near field $z_0 >> b^2/\lambda$, which is called Fresnel diffraction. A derivation can be found in [Demtröder, 2004]. Figure 2.2 illustrates the diffraction pattern in near- and far-field including the requirements made above.

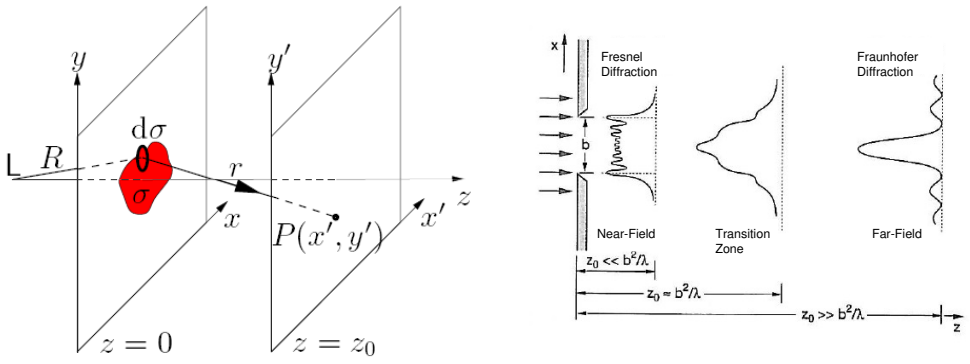

Figure 2.2: The left figure shows a derivation for the diffraction pattern for a random aperture. Detailed explanations can be found in the text. In the right figure diffraction is demonstrated on a single slit (figure: [Demtröder, 2004]): The diffraction pattern of the light wave obtained after the wave passes through a slit is shown in the near-field (Fresnel diffraction), in the transition zone and in the far-field (Fraunhofer diffraction). z_0 is the distance between aperture and the image plane, where the diffraction pattern is observed.

The objective of an optical system typically has a circular aperture. As lenses do not have infinite diameter surfaces edge effects (diffraction) occur. As a result a point

like object appears as a spot of a certain size in the detection plane, which shows a far-field diffraction pattern due to Fraunhofer diffraction. Assuming a perfect lens and a circular aperture the diffraction pattern will look like the pattern illustrated in figure 2.3 (left diagram).

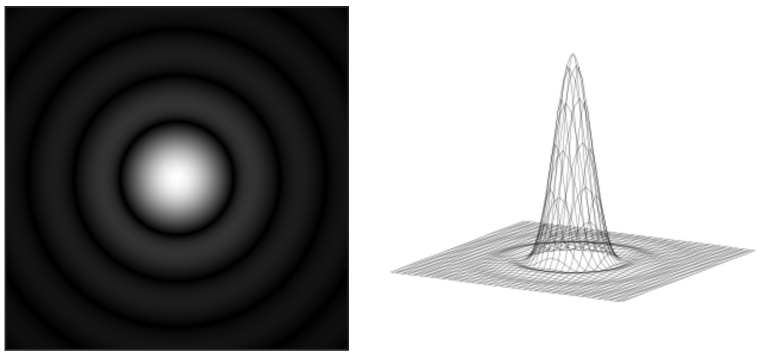

Figure 2.3: The left diagram illustrates the Fraunhofer diffraction pattern of a circular aperture. The central maximum is called the Airy disc. The pattern is generated by constructive and destructive interference of the light. A 3D illustration can be found in the right diagram. The central maximum contains a main fraction of the intensity ([Wikipedia, 2009]).

The very bright region in the center represents the main maximum of zeroth order and is known as the airy disc. A surface plot of the diffraction pattern and its Airy disc can also be found in figure 2.3 (right diagram). The size of the Airy disc is depending on the wavelength of the incident light and on the size of the aperture. It defines the resolution achievable with the optical system limited by diffraction.

2.1.2 PSF and Resolution

Diffraction limits the resolution of an optical system. A point source of light imaged with an optical system always appears as a spot of a certain size as explained in the previous section. The intensity profile of such a spot is described by the Point Spread Function (PSF). Figure 2.4 shows the PSF of a point like objective in the lateral direction (left), which is the Fraunhofer diffraction pattern as expected from a circular aperture. The intensity profile in the axial (z) direction is illustrated on the right side. The diffraction limited intensity profile of a point like source or PSF can mathematically be described by a Gaussian or normal distribution, which approximates the Airy disc. The Full Width of Half Maximum (FWHM) of the Gaussian distribution quantifies the achievable resolution of the optical system. This is the

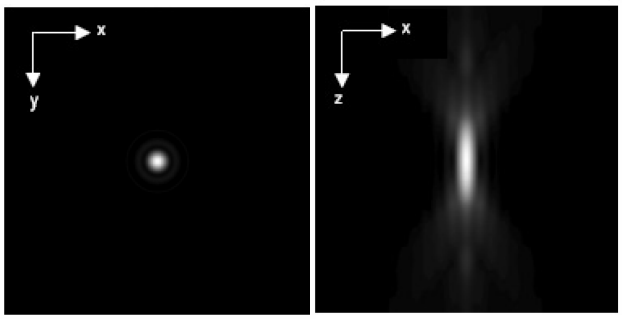

Figure 2.4: The intensity profile or PSF of a point like object after the imaging process. The lateral PSF is illustrated on the left side, whereas the axial (z) PSF is demonstrated on the right side. It is clearly visible that the resolution in the axial direction is smaller than in the lateral direction ([Wilhelm et al.,]).

width of the distribution when the intensity has decreased by 50 %. To gain the FWHM or resolution of a optical system the x value at half heights of a Gaussian or normal function is calculated.

$$\exp\left(\frac{x^2}{2\sigma^2}\right) = \frac{1}{2} \tag{2.9}$$

with 2x=FWHM and $2 \cdot \sqrt{2 \ln 2}$=2.35. After a few mathematical conversions the following expression can be derived:

$$FWHM \approx \sigma \cdot 2.35 \tag{2.10}$$

As the central maximum in the diffraction pattern is broader in the axial direction than in the lateral directions, the axial resolution is lower than the lateral resolution.

2.1.3 Fluorescence and Photobleaching

In quantum mechanics light consists of elementary quanta of energy, the photons, whose energy is defined by Planck's law:

$$E = h \cdot \nu = \frac{h}{\lambda} \tag{2.11}$$

where h is the Planck constant, ν the frequency of the electromagnetic wave and λ its corresponding wavelength. Fluorescence is the result of the absorption and emission of photons, which cause discrete electron transitions within an atom or molecule. A atom/molecule consists of several discrete electronic states. Each electronic state can be split into various rotational states and vibrational states, which are also discrete. The ground-state is the state of minimal energy, which is naturally preferred as it is more stable.

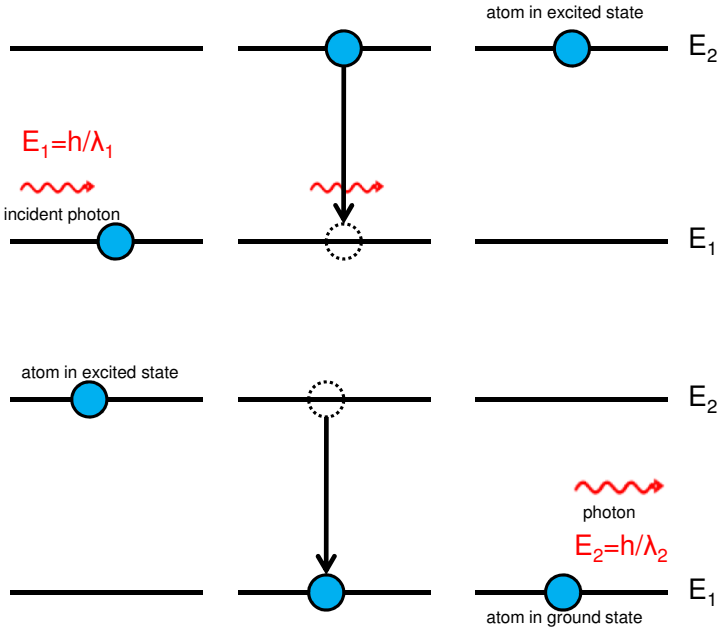

Figure 2.5: An incident wave interacts with an atom/molecule: One photon of an appropriate energy $E_1 = h \cdot \nu_1$ is absorbed and results in an electron transition from the ground-state to an excited state. Afterwards the atom/molecule relaxes back into the ground-state by another electron transition. As a result a (fluorescent) photon is emitted due to energy preservation, which has an energy of $E_2 = h \cdot \nu_2$. The energy difference of the absorbed photon compared to the emitted photon can be found in vibration or rotation of the atom/molecule.

As electrons within an atom/molecule can interact with the oscillating field vector of an incident electromagnetic wave by absorbing a photon, which leads to an electronic transition within the atom/molecule to a electron state of higher energy (excited state, see figure 2.5). As atoms/molecules only consist of discrete energy states, the absorbed photon must have an energy in consistency with Plank's law, which fits one of the possible transitions in the atom/molecule. The hydrogen atom

(H) is the easiest example for describing electron transitions. Assuming no external magnetic fields the following equation describes the energy-difference between the initial state and the final state within a hydrogen atom. This is the energy a photon must have in order to be absorbed:

$$E = h \cdot \nu = \frac{h}{\lambda} = h \cdot c \cdot R_H \cdot (\frac{1}{m^2} - \frac{1}{n^2}) \tag{2.12}$$

R_H is the Rydberg constant, n is the main quantum number and m is the angular momentum quantum number. The main quantum number n numbers the electronic states, whereas the angular momentum quantum number m numbers the rotational levels. If additionally the transition dipole moment of the atom/molecule is parallel to the oscillation plane of the electromagnetic wave, it is more likely that the atom/molecule absorbs the energy and passes into an excited state. For all other atoms and molecules it is much more complicated to describe the energy levels mathematically.
Depending on the state and the energy the atom/molecule relaxes after the 'lifetime' of the state either by emitting a photon or by transferring the energy into vibrations and rotations. The lifetime of a state is the characteristic mean time an atom/molecule stays in this state before it relaxes into the ground-state (see also figure 2.5).
Usually electron transitions occur between states of the same multiplicity, which means that changes in the electron-spin-paring are unlikely due to a disadvantageous energy consumption. The multiplicity (2S+1) defines the number of possible orientations the spin (S) of the atom/molecule can adopt. A spin state of S=0, a singlet state, has only paired electron-spins, whereas a S=3, a triplet state, has parallel orientated, which is energetically less favorable. Theoretically a transition from a singlet state to a triplet state is forbidden due to the selection rule $\Delta S = 0$ and is therefore very unlikely. Nevertheless it is possible to enter a triplet state when the atom/molecule undergoes an electron-spin conversion to produce unpaired electron-spins.

The Jablonski Diagram shown in figure 2.6 illustrates some typical electron transitions and the different ways of relaxation. Each electronic state is split in vibrational states (rotational states not shown). An atom/molecule absorbs a photon

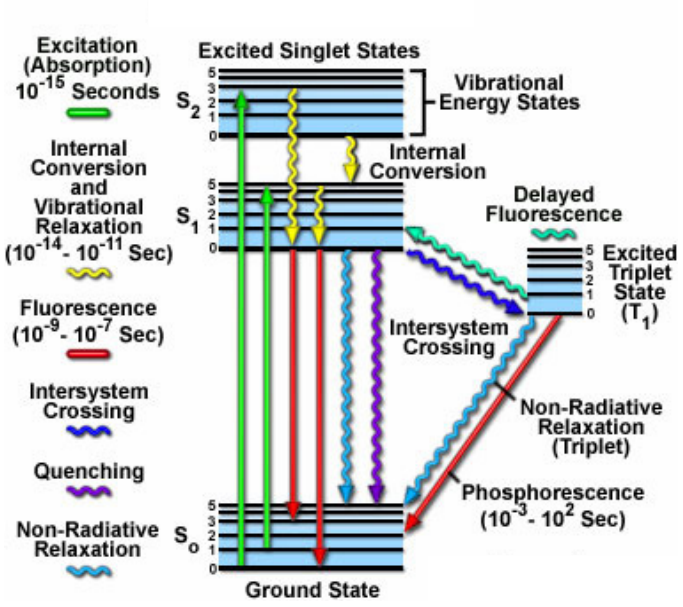

Figure 2.6: Overview: The Jablonski diagram shows possible electron transitions within the atom/molecule and several different ways of relaxation. The fluorescent relaxation between two singlet states is exploited in fluorescence microscopy. A detailed explanation of the diagram can be found in the text (diagram: [Davidson, 2009]).

(10^{-15} nanoseconds), which pushes on of its electrons from the ground state (S_0) into an excited state (S_1 or S_2). Excess energy of the absorbed photon results in an electron pushed to a higher vibrational energy levels within the excited electronic state. Internal Conversions (IC) between two excited states and vibrational relaxations between two different vibrational energy levels within the same electronic state can already lead to an energy loss compared to the energy absorbed. IC and vibrational relaxations take place within 10^{-14} to 10^{-11} seconds and the energy gained in this process is converted into heat. In this example fluorescent light occurs when the atom/molecule relaxes back to its ground state (S_0) from the lowest excited state (S_1). The excited state lifetime is typically exists 10^{-9} to 10^{-7} seconds. Besides fluorescent relaxation quenching (see later explanation) and other non-radiative relaxations can occur, which are often not desirable for fluorescence microscopy. Intersystem Crossings (ISC) are less likely due to the forbidden transition between a singlet and a triplet state. The electron stays in a triplet state for a much longer time period (10^{-3} to 10^{-2}) and relaxes afterwards either in a radiative process known as phosphorescence or in a non-radiative process. There is no interference between fluorescence and phosphorescence in fluorescence microscopy due to

the much longer lifetime of the excited triplet state compared to the excited singlet state. The ratio of the competing processes for the relaxation of the atom/molecule is the quantum yield, which describes the probability of a fluorescent emission after an atom/molecule has been excited.

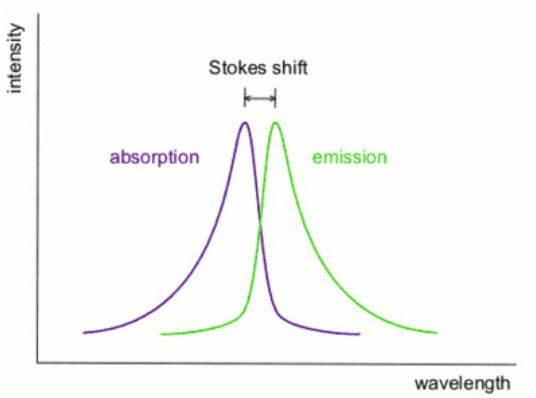

Figure 2.7: The Stokes Shift: Photons, absorbed (excitation light) by an atom/molecule and causing an electron transition, have a higher energy (smaller wavelength) than the emitted photons by the same atom/molecule (lower energy, longer wavelength). The difference in the wavelength of the intensity maxima is the Stokes shift. The requirement of energy conservation is still fulfilled: The energy difference can be found in vibrations of the atom/molecule ([Wikipedia, 2009]).

As the criterion of energy conservation must be fulfilled the emitted fluorescent photon must have either the same energy as the photon absorbed by the atom/molecule or it has less energy, because of non-radiative relaxations. The wavelength of the emitted photon is therefore generally longer compared to the absorbed photon, which is called the Stokes Shift (see figure: 2.7):

$$\lambda_{Stokes} = \lambda_{in} - \lambda_{out} \tag{2.13}$$

This enables to separate the excitation light from the emitted light, which will be exploited in fluorescence microscopy (see section: 2.1.4).

Fluorophores are functional groups of a molecule, which are able to fluoresce after they absorbed a photon. Due to the splitting of the electronic states into vibrational and rotational states, a fluorophore has a certain excitation bandwidth and

also an emission spectrum of a certain range of wavelength's. Autofluorescence is a unwanted source of fluorescence in fluorescence microscopy, which overlays with the desired fluorescent light.
The ability to fluoresce can be influenced by two processes. Photobleaching is the irreversible photo-induced chemical destruction of a fluorophore due to the high energy during the light exposure. The fluorophore undergoes a irreversible chemical reaction with another molecule, which leads to a conformation change in its structure. As the triplet state of an fluorophore lasts much longer and is chemically highly reactive, it is more likely that a fluorophore is bleached in this state. To avoid the destruction of the fluorophore, triplet-state quencher can be added to the chemical environment. β-mercaptoethylamine is an example for a triplet-state quencher and it also functions as a reducing agent, which quenches unwanted triplet states and is able to recover photoionized fluorophores ([Vogelsang et al., 2008]).
Quenching is the decreasing intensity of the fluorescent light emitted by fluorophores without destroying the fluorophore. A few processes can quench fluorescence. Quenching is in comparison to photobleaching usually reversible. The most important process is the energy transfer from the fluorophore in its excited state to another molecule (quencher) in a collision. The energy is mostly converted into heat and the fluorophore goes back into its ground state without a fluorescent radiation. Other collisions cause a complex between quencher and fluorophore, which also decreases its ability to fluoresce. In biological samples oxygen is a typical quencher. It can be excited from its triplet ground state into a reactive excited singlet state and is then able to react with the fluorophore. It is most likely that the fluorophore undergoes ISC into a triplet state under the influence of the oxygen and is then quenched by it into its ground state ([Lakowicz, 2006]). Phosphorescence is not observed. This reaction can also generate free reactive singlet oxygen, which itself can react with other molecules. Other mechanism, which result in fluorescence quenching can be found in [Lakowicz, 2006] (chapter 8).

The chemical environment (mounting medium) influences single molecule detection very sensitively. Certain agents can be responsible for an unwanted quenching of the fluorescent emission. Oxygen is probably the most likely quencher in a biological sample. To remove oxygen from the chemical environment, which is used to mount the sample on the slide, oxygen scavenger like glucose oxidase and catalase are added ([Heilemann et al., 2008]). Additionally reducing agents and triplet-quencher

like β-mercaptoethylamine, which are able to recover photoionized fluorophores, can be added ([Vogelsang et al., 2008]). A 'switching buffer' is a mounting medium containing oxygen scavenger as well as reducing agents, which support the switching of the fluorophores between the bright- and the dark-state.

2.1.4 Fluorescence Microscopy

Abbe defined the resolution of a microscope as follows: Two points of an object are still resolved if the objective is able to capture the first order maximum of the diffraction pattern. The mathematical expression for this definition was already explained in section 1 in formula 1.1.

Numerical Aperture and Oilimmersion

Resolution is also depending on the amount of light emitted by the sample that can be collected. The ideal case would be lenses with an infinite surface, which is able to capture all light rays, and a infinite small working distance. In reality the objective is only able to capture a certain fraction of the light emitted by a sample. This translates into less information and less detailed resolution. The more light is captured by the objective, the higher the resolution.
The resolution an objective can achieve is not only dependent on the angle of the objective, it is also depending on the refractive index of the medium between objective and cover slip. Therefore the Numerical Aperture (NA) characterizes the resolution achieved by an objective. It specifies the maximal angle under which light rays will be still captured by the objective taking the refractive index of the medium between into account:

$$NA = n * sin\alpha \tag{2.14}$$

where n is the refractive index of the medium and α is only half of the complete angle, which can be captured by the objective. As the angle is limited resolution can be improved by using an immersion medium between objective and cover slip, which has a similar refractive index as the glass. Without any refraction compensation light rays occurring under a high angle are refracted or even reflected by passing through the cover slip (see figure 2.8). Using an immersion medium reduces refraction highly,

avoids reflected rays and even light rays on the very edges can be collected (see figure 2.8).

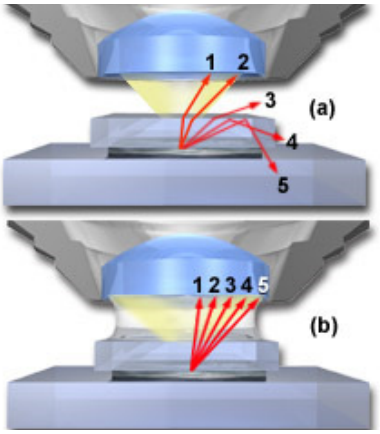

Figure 2.8: Without any refraction compensation light rays occurring under a higher angle are refracted (top: rays 3 and 4) and rays on the edges are even reflected (top:ray 5). Using an immersion medium between objective and cover slip, which has a similar refractive index as glass, reduces refraction highly and rays on the edges are capable (bottom: ray 5). Resolution is therefore increased by a factor of the refractive index, which is expressed in the definition of the numerical aperture ([Davidson, 2009]).

Dichroic Beamsplitter and Emission Filter

A dichroic beamsplitter reflects only a certain part of the electromagnetic spectrum and transmits the remaining part. The separation conducted by the wavelength of the incident light, which enables to separate the light by color. The whole process is based on interference of partial waves on the surface of the beamsplitter. Several very thin layers of different refractive indices are evaporated on the surface of the beamsplitter (usually glass), which leads to interference of the incident partial light waves. The result are constructive and destructive interference of partial light waves, which leads to a wavelength-selective transmission spectrum. The principle of interference was already explained in section 2.1.1. Partial waves are either reflected or transmitted on each layer depending on their wavelength and on the refractive index of the layer. As a result constructive and destructive interference enables to split the incident light wave into one reflected and one transmitted beam, which consists only of a certain range of the light spectrum.
Depending on the wavelength, which should be transmitted or reflected, a individual optical coating of the beamsplitter for different applications can be generated. The

angle of the incident light wave is also important for the characteristic transmission spectrum. Slight variations in the angle can already produce a different transmission spectrum. Therefore they are usually designed for an incoming light wave under an angle of 45°. Fluorescence microscopy is based on the principle of separating excitation light and the fluorescent emission light of the sample, which is performed by using a dichroic beamsplitter as described in this section.
Usually beamsplitter do not transmit or reflect 100 % of the light. To avoid unwanted light being transmitted by the beamsplitter an additional emission filter can be used to filter the light. This emission filter is of a higher optical density, which leads to nearly 100 % transmission in the wavelenght range of interest and blocks the remaining part of the spectrum. The emission filter is also based on the principle of constructive and destructive interference of partial waves. The difference to the beamsplitter is only the angle of the incident light, which usually is 0°.

The Fluorescence Microscope

The wide-field fluorescent microscope is a far-field imaging technique, which exploits the stokes shift between excitation light and the emitted fluorescent light. Figure 2.9 shows the pathway of the light in such a microscope. A light source (e.g. arc lamp, laser) can be filtered for a specific wavelength (λ_2) by an excitation filter (EX), which fits the excitation spectrum of the fluorophores used to label the sample. Other wavelengths are blocked (λ_1 and λ_3). The selected excitation light is reflected on a dichroic beamsplitter (DB) in an angle of 45° into the direction of the sample. Scattered excitation light is reflected back into the direction of the light source by the dichroic beamsplitter (λ_2), whereas fluorescent light emitted by the sample due to excitation passes through the dichroic (λ_4). Unwanted spectral components of the fluorescent light or fractions of the excitation light (λ_5) are blocked by an emission filter (EM), which is of a higher optical density then the dichroic beamsplitter.

2.1.5 RPM and Dark-State Engineering

Reversible Photobleaching Microscopy (RPM) is a wide-field fluorescence microscopy method based on STORM (see section 1 and [Baddeley et al., 2009b]). STORM excites only a spare number of fluorophores at the same time by using a low excitation energy, records those and then they are bleached. Ideally only one fluorophore is excited in a diffraction limited area. As a result the PSF´s of the single fluorophores

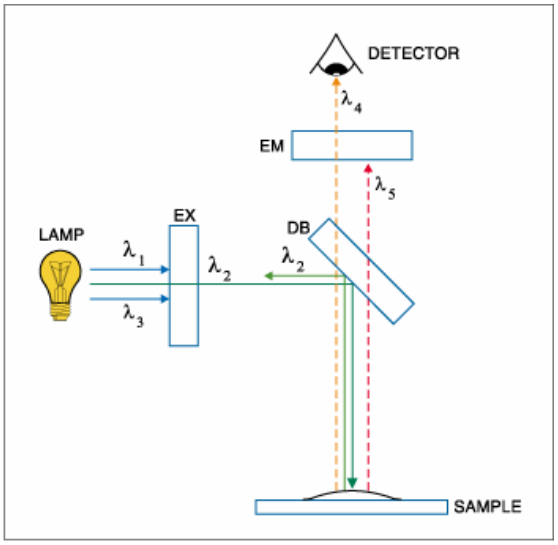

Figure 2.9: The light path in a fluorescence microscope: The excitation filter (EX) is able to select a certain wavelength, which is suitable for exciting the fluorescent sample, and blocks all other wavelengths. The dichroic beamsplitter (DB) reflects the excitation light in an angle of 45° in the direction of the sample, whereas the fluorescent light emitted by the sample is transmitted by the and can be detected. Scattered excitation light is mainly reflected by the dichroic beamsplitter. Unwanted fluorescent light or fractions of the excitation light, which were able to pass the dichroic beamsplitter are blocked by an additional emission filter (EM), which is of high optical density ([Invitrogen, 2008]).

do not overlap. Therefore it is possible to evaluate their position quite accurately by calculating the center of the approximated Gaussian distribution. The limit is then no longer the diffraction and a theoretically infinite resolution can be achieved. A major difference of RPM compared to STORM is the high excitation energies used in this method. Using high excitation energies pushes most of the fluorophores into a 'dark state' from where they recover stochastically and only a small number at the same time. As the fluorophores are able to 'recover' from the dark state several switching cycles of the same fluorophore can be recorded, which is an advantage in terms of more accurate localization precisions.

A 'dark state' is not well understood yet. Its is a non fluorescent state the fluorophore can spontaneously enter after being excited to a 'bright state' (B). The dark state (D) can not be excited by the excitation wavelength and therefore appears as a non-fluorescent or 'dark state'. The fluorophore is not destroyed and is

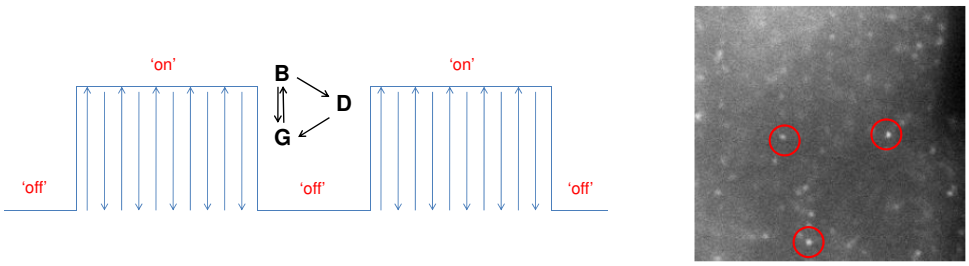

Figure 2.10: Electron transitions between ground state (G) and bright state (B) result in fluorescence. One event detected by the camera consist of several thousand electron transitions. The fluorophore enters a bright - it is 'on'. When the fluorophore enters a triplet state, a dark state (D) or is photobleached, the fluorophore is detected as 'off'. One fluorophore can undergo several of those switching cycles between 'on' and 'off' until it is photobleached or undergoes chemical reactions with other molecules. If the fluorophore enters a dark state it is able to recover slowly from this state. The right figure shows single molecule events as they appear during the recording.

able to recover slowly from this state back to its ground state (G) from where it can be excited again (see figure 2.10. The lifetime of a dark state can be in the range of msec and up to several minutes ([Vogelsang et al., 2008]), which suggests that is not a triplet state as explained in section 2.1.3). A few suggestions for a dark state can be found in [Vogelsang et al., 2008]. As the recovery from the dark state happens at a much slower rate than the transitions between ground and bright state, it is possible to detect only a few fluorophores at the same time ($\tau_{on} << \tau_{off}$).
The whole number of absorption-emission cycles an fluorophore can undergo before it either enters a dark state or is photobleached is detected as one 'event'. As those transitions are very fast, the camera is not able to distinguish between absorption and emission and therefore sums all cycles as one event. The fluorophore is 'on' while it undergoes absorption-emission cycles and otherwise it is detected as 'off' (see figure 2.10). Several switching cycles between 'on' and 'off', which is recognized as 'blinking', can occur before the fluorophore is either photobleached or has reacted with other molecules. An example of single molecule events is also presented in figure 2.10.

2.1.6 Localization Prediction

In the past an equation was published ([Thompson et al., 2002]), which describes the localization precision of single molecule events for a wide range of circumstances. Before beginning to derive an equation for that purpose the two localization limiting factors 'photon-counting noise' and 'background noise' are considered. As the vari-

ances of the limiting factors are independent of each other it is allowed to add them. The square root of the sum of the variances for each pixel i is then the expected uncertainty:

$$\sigma_i{}^2 = N_i(x) + b^2 \tag{2.15}$$

The quantum nature of light produces fluctuations in detected photon numbers and implies that detection of light emission is a statistical process. Therefore photon counting is to be Poisson distributed (see section 2.1.7). The variance of a Poisson distribution is equal to its expectation value, in this case the photon number N per pixel. The background noise b^2 due to out-of-focus fluorescence, autofluorescence and CCD read-out noise, is assumed to be constant across the region of the spot. A least-squares fit of a Gaussian intensity distribution of the event results in following expression:

$$\langle(\Delta x)^2\rangle = \frac{(\sigma_{PSF})^2 + \frac{a^2}{12}}{N} + \frac{8\pi(\sigma_{PSF})^4 b^2}{a^2 N^2} \tag{2.16}$$

This variance in the localized position consists of two main terms. The first one describes the photon-noise limited case for the detection accuracy, the second term the background limited one. The photon-counting term is extended taking 'pixelation-noise' into account. As the pixel size a (70 nm x 70 nm) is not infinitesimal an uncertainty in where the photon actually hits within the pixel area is created. Integration over a top-hat distribution produces the variance $\frac{a^2}{12}$ which is included into the first term of the formula. σ_{PSF} can be replaced by following expression, which is derived from calculating the FWHM (spot size) of the PSF approximated by a Gaussian curve (see section 2.1.2):

$$(\sigma_{PSF})^2 = \frac{(FWHM_{PSF})^2}{2.35} \tag{2.17}$$

The background arises mainly from out-of-focus fluorescence and autofluorescence, which is taken into account by measuring the level of background photons N_b. The second component that influences the background, is caused by the read-out noise of the camera. This noise source appears after the electron multiplication. Therefore

the standard deviation describing the dimension of the read-out noise needs to be divided by the True-EM-Gain.

$$b^2 = N_b + \left(\frac{\sigma_{readoutnoise}}{em - gain}\right)^2 \tag{2.18}$$

Then the actual error in localization is given by the square root of the variance: $\Delta x = \sqrt{\langle(\Delta x)^2\rangle}$. A detailed derivation of formula 2.16 can be found in [Thompson et al., 2002]. The presented theoretical approach for calculating the localization precision is used in later analysis in order to compare experimental results with the literature and theory.

2.1.7 EMCCD-Camera

Electron Multiplying Charged Coupled Device (EMCCD)-camera is able to produce high quality image data and therefore can be used to detect single molecule event. The chip is usually a semi-conductor and its functionality can be explained with the band theory for solid-state physics (for detailed explanation see [Kittel, 2006]). An incident photon hits a pixel and raises a electron from the valence band into the conduction band (inner photoelectric effect). The energy of the photon must be greater than the band gap between valence and conduction band. By applying an external voltage to the pixels a quantum well can be created, which stores these electrons. The number of the stored electrons is then equal to the number of incident photons or proportional to the light intensity. Each pixel can contain a maximum number of electrons. Is the number of incident photons too high, excrescent electrons can cross over to neighboring potential wells.
The CCD-chip consists of a grid of pixels. Each pixel stores the primary electrons in a potential well. The whole grid is read-out line by line. This is done by shifting the electrons from one line to the next by reversing the polarity of the quantum wells (see left figure 2.11). As a result one line of pixels is shifted into the read-out register. There the stored electrons are run through an Electron Multiplying process (EM-gain), where primary detected electrons are multiplied by impact ionization. Afterwards the Analog-to-Digital converter (A/D converter) converts the number of electrons per pixel into a digital number proportional to the magnitude of the voltage (see right figure 2.11). The integration time of the camera is the time pe-

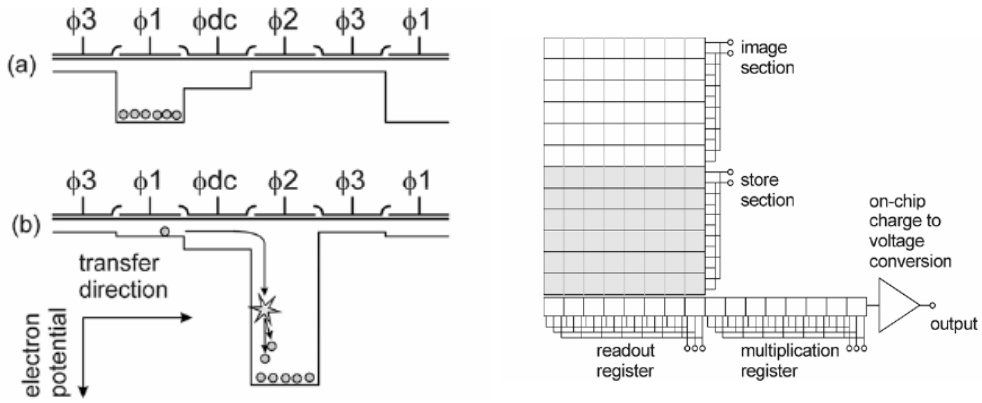

Figure 2.11: The left figure illustrates the electron transfer from pixel to pixel during the read-out process. At first the electrons are stored in the potential well Φ_1. During the proceeding read-out process potentials of the wells are reversed, which results in the shifting of the electrons into the next potential well (Φ_2). The whole read-out process is summed up in the right figure. Each pixel stores the detected electrons. The grid is read-out line by line and each line is running through an electron multiplying process. Finally a A/D-converter produces a digital signal out of the incoming analog signal (both figures [Robbins and Hadwen, 2002]).

riod over which the camera accumulates all detected photons, reads out the pixels after this time period and gives out the resulting digital image as one frame of the whole recording. The integration time is chosen according to the 'on-time' of the fluorophore in order to gain the maximal intensity possible. This leads to a more accurate localization precision of the position in the later analysis. If the integration time is chosen to be shorter than the 'on-time', the intensity of the event would be less due to the additionally accumulated dark period. The same applies to a integration time longer than the 'on-time'. Additionally the relative magnitude of the background could increase, which also leads to a lower intensity profile of the detected fluorophore.

Noise are unwanted variations in the pixel values, which influences the detection and the image reconstruction negatively. Noise can be modeled as a Poisson distribution and is characterized as the standard deviation of the mean pixel value. It's the variation in the number of electrons/photons detected in the same pixel over time. The signal-to-noise describes the signal power of an event compared to the noise power related to background noise. A high ratio leads an signal/event, which is well separated from the background. Ideally high photon numbers per event are desirable without overdriving the camera. The background becomes more important

when detecting lower photon numbers, which usually result in a greater localization error.

Photon shot noise is caused by statistical fluctuations in the detection of photons when dealing with smaller numbers of photons. A Poisson distribution describes the variations in the pixel value due to shot noise.

Dark current is the number of additional electrons introduced by thermal photons, which are not part of the incoming light. Cooling down the CCD-chip reduces the dark current. By subtracting a dark frame, which is not exposed to any light, the noise introduced by dark current can be partially removed. The additional shot noise the dark current possesses is remaining. By using an em-gain, which increases the number of electrons, the negative influence of noise on the detection can be reduced.

Read-out noise defines the number of additional electrons in the final signal caused by the read-out process of the CCD-chip. The A/D conversion introduces noise as well as the electronic devices of the camera. As the electronic current is consisting of discrete charges, which leads to fluctuations, shot noise also occurs in the electronic devices. John-Nyquist noise appears in the electronics of the camera without the influence of photons and are due to random thermally generated electron-hole-pairs. Additional electrons also occur during the shift of the electrons from pixel to pixel by reversing the polarity of the potential wells.

2.2 Biological Model: Cardiac Muscle Cells

Three different types of muscle cells can be distinguished: skeletal, smooth and cardiac muscle. All three are translating a chemical or electrical signal into force. As a result the muscle contracts. The trigger always is a rise in the free cytosolic Ca^{2+} concentration ($[Ca^{2+}]_i$). But there are various differences in structure and functionality, which allows them to fulfill different purposes. All experiments in this thesis were performed with rat ventricular myocytes.

2.2.1 Structure of Cardiac Myocytes

The structure of cardiac myocytes bears some resemblance to skeletal muscle cells, but there are substantial differences in their functionality. Each myocyte (fiber) contains several parallel, cylindrical myofibrils, which are densely packed (see figure 2.12). Intercalated disks are the areas at the ends of cells in contact with adjacent cells. There they are connected to each other by desmosomes. Gap junctions in this area allow an exchange of ions between cells and thus provide an electrical coupling. Between myofibrils mitochondria, the 'cellular power plants', are embedded. The repeating units in the myofibrils are the sarcomeres, separated from each other by the Z disks. They are highly organized, which gives them a striated appearance (striated muscle).
Two types of myofilaments, within the sarcomeres, can be distinguished: The thick filaments primarily consisting of myosin and the thin filaments primarily consisting of actin. The thin filaments are anchored in the Z disks, which are perpendicular to the fiber axis and contain alpha-actin. Thin filaments have a diameter of 5 to 8 nm and a length of 1μm. The thick filaments have a diameter of 10 nm and a length of 1.6 μm. They are interdigitated with the thin filaments and connect those next to each other as well as those thin filaments originating from opposite Z disks. The A-band (anisotropic to polarized light) is the area where thin and thick filaments overlap, the H-band is the area containing only thick filaments and the I-band (isotropic to polarized light) contains only thin filaments. During contraction the I-band shortens, while the A-band stays unaltered. The cross-bridges between the filaments are established by the pivoting heads of the myosin.

The backbone of the thin filaments is a double-stranded α-helical F-actin poly-

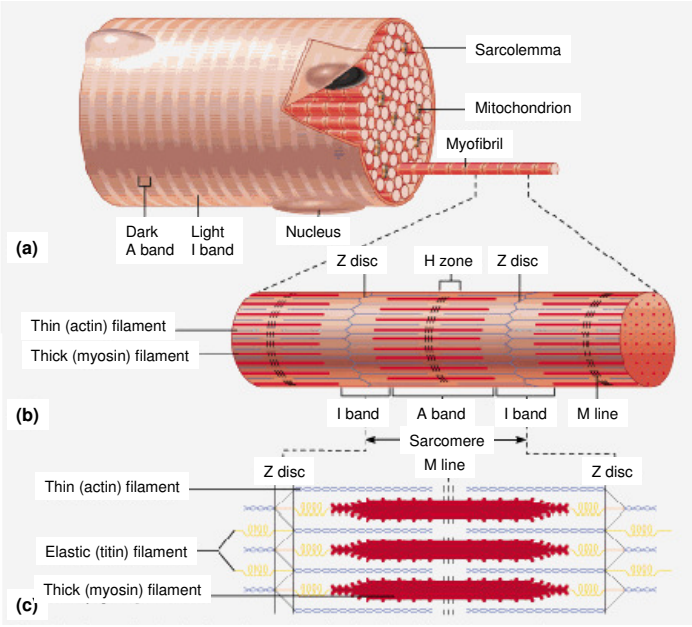

Figure 2.12: Structure of a muscle cell ([Cummings, 2009]): A muscle fiber, surrounded by the sarcolemma (membrane) contains of several cylindrical myofibrils, which itself consists of sarcomeres. Sarcomeres are separated from each other within the myofibril by the Z disks. The substructure of the sarcomeres are the thin (actin) filaments and the thick (myosin) filaments. The A-band is the area where thin and thick filaments overlap, whereas the H-band only contains thick filaments and the I-band only thin filaments. The M-line represents the middle of the sarcomere. Further and more detailed explanation can be found in the text.

mer. Each turn consists of 13 actin monomers and is approximately 70 nm long. Troponin and tropomysosin are actin-binding proteins and play an important regulatory role in cardiac contraction. Tropomysoin consist of two α-helices coiled around each other and located in the two grooves formed by the actin double helix. One molecule has an approximate length of 35 nm and is associated at each end with another tropomyosin molecule. One molecule of tropomyosin interacts with seven actin molecules and each troponin-molecule interacts with one tropomyosin-molecule and also directly with the actin filaments. The troponin-complex has a substructure of three different molecules. The subunit troponin-T binds to tropomyosin and assures interaction between those. The subunit troponin-I binds to actin and inhibits contraction of the sarcomere, whereas the subunit troponin-C is the Ca^{2+} binding unit and is also related to the Ca^{2+}-binding protein calmodulin. All interactions between thick and thin filaments are triggered via changes in the Ca^{2+} concentration.

The thick filaments consist of polymers of bipolar myosin-II molecules, which itself is a double trimer. Each molecule consists of two intertwined heavy chains (rod, hinge and head region), two regulatory light chains and two alkali light chains. The head region (S1 fragments) of the heavy chains connect thick and thin filaments by binding to the myosin binding site of the actin molecules. It possesses also a ATP binding domain, where ATP can be hydrolyzed and the energy can be used for contraction. The alkali light chain plays a role in stabilizing the head region and the regulatory light chain regulates the ATPase activity of the myosin, whereas the ATPase activity is regulated by Ca^{2+}-dependent and Ca^{2+}-independent kinases, which regulated via phosphorylation ([Boron and Boulpaep, 2005]).

Additional components have to be mentioned, which are also part of cardiac myocytes (see figure 2.13). Transverse invaginations of the sarcolemma can be found in carciac myocytes, which is known as the t-tubule system. It is an extension of the extracellular space containing Ca^{2+}. Ca^{2+}-channels are embedded into the sarcolemma, which are able to release Ca^{2+} into the cell (cytoplasm). Ca^{2+}-ATPase (ATP) and Sodium-Calcium-Exchanger (NCX), also embedded into the sarcolemma, transport Ca^{2+} from the cytoplasm into the extracellular space against an electrochemical gradient. The ATPase obtains the required energy for this process by converting an ATP-molecule into ADP, whereas the Sodium-Calcium-Exchanger gains the energy by transporting a Na^{2+}-ion in an antiport-mechanism. Moreover NCX is able to bring Ca^{2+} into the cell. A big Ca^{2+}-reservoir inside the cell is the sarcoplasmic reticulum (SR). It is connected with the cytoplasm by ryanodine receptors (RyR), which can release Ca^{2+} from the SR into the cytoplasm. In the mitochondria membrane embedded are a Ca^{2+}-uniporter, which transport Ca^{2+}-ions into the mitochondria. They produce ATP, which is the energy supplier for many biological processes such as the ATPase or the activation of the Phospholamban (PLB) a regulatory protein. The cytoskeleton is the scaffolding of the cell, which is a dynamic structure of actin filaments, intermediate filaments and microtubules. Microtubules (not shown in figure 2.13) have a diameter of 25 nm and a length of 200 nm to 25 μ m. It is a polymer consisting of α- and β-tubulin. It plays an important role in processes such as mitosis and vesicular transport. Motor proteins like kinesin and dynein can move along the tubules. Caveolae are invaginations in the sarcolemma, which contain the small proteins caveolin-1,-2 and -3 and have a size of $\backsim$ 80 nm,. They are associated with a range of functions, which vary from membrane transport and signal transduction

over endocytosis to regulations in the Ca^{2+}-metabolism.

2.2.2 Functionality

Excitation Contraction Coupling (ECC) is the mechanism a cardiac myocyte goes through during a cycle of excitation, the resulting contraction and the final relaxation of the muscle cell. The trigger for the whole process is the electrical depolarization of the membrane.

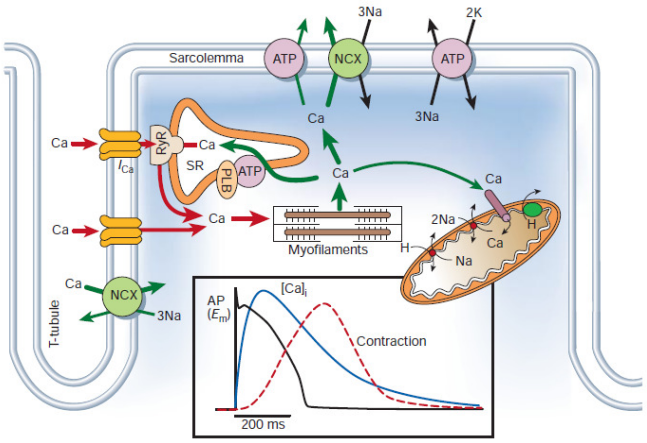

Figure 2.13: The Ca^{2+}-transport within cardiac myocytes is illustrated. Ca^{2+} enters the cell through Ca^{2+}-channels or NCX in an antiport mechanism. Ca^{2+} triggers additional Ca^{2+}-release from the SR by activating the RyR-channels. Then Ca^{2+} binds to myosin, which activates it and results in a contraction of the muscle cell. After an action potential has subsided Ca^{2+} is extruded into the extracellular space by NCX and into the SR by PLB. A detailed explanation can be found in the text. The diagram shows the time-correlation between the action potential, which excites the cell, and the following Ca^{2+}-release ([Bers, 2002]).

In ventricular myocytes electrical depolarization of the membrane and gap junctions (electrical synapses) are present. Gap junctions, which connect the sarcolemma of neighboring cells, forward electrical impulses (electrical current) from cell to cell, which is faster than chemical transmissions. Therefore it is possible to initiate simultaneous contractions of the heart cells, which is absolutely essential for a steady pumping heart and simultaneous relaxation to preclude frequency summation. The electrical impulses (action potentials) are periodically generated at the sinoatrial node placed in the pacemaker region of the heart. After an action potential is generated and is able to overcome a certain threshold, the electrical current flows

through the gap junctions from cell to cell and depolarizes the cells. As a result of the depolarization of the sarcolemma, voltage gated Ca^{2+} channels (L-type channels, dihydropyridine receptors: DHPR) in the membrane open and release extracellular Ca^{2+} into the cytoplasm. Thus, the Ca^{2+} can reach all cytosolic regions in the heart by diffusion. $[Ca^{2+}]_i$ (inner cell Ca^{2+} concentration) itself induces Ca^{2+} release (CICR) from the SR through ion-gated Ca^{2+} release channels (ryanodine receptors: RyR) into the cytoplasm. The Ca^{2+} release from the SR, which amplifies the inner cell Ca^{2+} concentration sufficiently, is absolutely necessary for contraction. In the rat much more Ca^{2+} influx into the cytoplasm is contributed by SR release compared to extracellular influx. In skeletal muscle cells DHPR and RyR are mechanically linked, whereas in myocytes they appear to be located in close proximity. Ca^{2+} released through DHPR seems to be unable to trigger any other RyRs in the SR membrane than the ones in immediate vicinity. Therefore Ca^{2+} release under normal conditions does not propagate along the myocytes and contraction is always a result of the summation of lots of CIRC events occurring at virtually the same time ([Boron and Boulpaep, 2005], [Bers, 2002]).

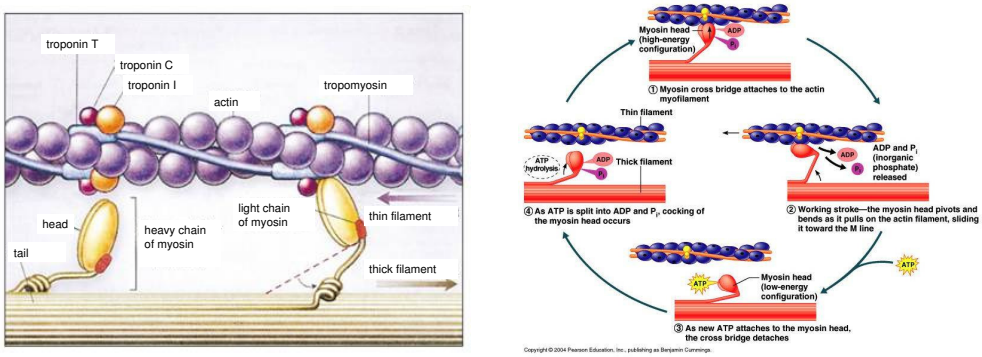

Figure 2.14: Ca^{2+} binds to the troponin complex, which stops the inhibition of tropomyosin. As a result tropomyosin can move away from the myosin binding sites on the thin (actin) filaments and expose those to the myosin heads in the thick filaments. The myosin binds to the actin. Hydrolysis of ATP into ADP provides the energy for a power stroke of the myosin. As a result the Z discs are pulled towards each other and the sarcomere shortens. When new ATP is bound the myosin relaxes. This cycle can be performed as long as the $[Ca^{2+}]_i$-concentration is high enough ([Cummings, 2009]).

After $[Ca^{2+}]_i$ increases Ca^{2+} forms a complex with troponin-C, which switches on the excitation-contraction mechanism. This complex initiates 'cross-bridge cycling'. Troponin-C has two high-affinity Ca^{2+}-binding sites and one low-affinity site. Dur-

ing activation the Ca^{2+}-binding to the low-affinity site induces a conformational change in the troponin complex, which firstly causes troponin-I to move away from the actin/tropomyosin filament, which stops the inhibition of the tropomyosin and allows it to move. As a result the myosin binding site on the thin (actin) filament is exposed. The myosin (thick) filaments can now bind to the actin filaments and the cross-bridge cycling can start. The myosin head is now able to bind strongly to the exposed myosin binding site on the actin filament. The myosin is able to hydrolyze Adenosin Tri Phosphate (ATP) into Adenosin Di Phosphate (ADP) and phosphate (P_i), which provides the myosin with energy for a 'power stroke'. As a result the Z discs are pulled towards each other, which shortens the sarcomere and also the I-band. New ATP binds to myosin, which leads to a disconnection of the actin and the myosin. This cycle can be repeated as long as $[Ca^{2+}]_i$ is high enough and ATP is present at sufficient concentration. If the $[Ca^{2+}]_i$-concentration is decreasing, tropomyosin will change its conformation again and blocks the myosin binding sites. The cell relaxes ([Müller-Erstel, 2004]).
ATP is essential for the movement of the myosin along actin filaments. Myocytes are never allowed to rest. Therefore they must assure a constant supply with ATP by having a very high density of mitochondria, which are responsible for the ATP-supply.
Ca^{2+} always interacts through regulatory proteins and never directly with the contractile proteins. In the absence of Ca^{2+} those regulatory proteins inhibit the cross-bridge cycling, which results in relaxation of the myocyte. As long as the Ca^{2+}+ concentration is high, the heart cell is contracted. The contractile force can be influenced by changing the amplitude and time course of Ca^{2+}, which is released into the cell and by altering the Ca^{2+} sensitivity of the regulatory proteins.

After termination of the excitation Ca^{2+} has to be removed from the cytoplasm, so the cell can relax. Sarcolemmal NCX, which operates strongly at high Ca^{2+} concentrations, and sarcolemmal Ca^{2+}-pumps (PMCA), which function also at low Ca^{2+} level, extrude Ca^{2+} into the extracellular lumen. A detailed description of the termination of the ECC process and the regulative proteins associated with ECC can be found in ([Boron and Boulpaep, 2005]).

Chapter 3

Materials and Methods

3.1 Cell Isolation and Fixation

The biological goal of this project is to image proteins involved in calcium signaling in heart cells. As the distribution and expression of these proteins changes significantly if the cells are taken into culture ([Lipp et al., 1996]), it is generally needed to obtain cells acutely from animal hearts (in this case rat). To extract the single cells needed for labeling and imaging from the rat tissue, an enzymatic isolation is used.

This cell isolation follows a protocol, which has to be observed very carefully. Adult rats are given a lethal injection of pentobarbitone (100ml/kg), which is used in veterinarian medicine as anesthetic as well as a drug for euthanasia. After removing the heart and washing it briefly in Ca^{2+}-free Tyrode's solution to remove the remaining blood, a cannula is inserted to the aorta of the heart and connected to a modified Langendorff perfusion system. This system enables to perfuse the heart with a nominally Ca^{2+}-free Tyrode's solution (containing 120 mM NaCl, 5.4 mM KCl, 10 mM Hepes, 5 mM pyruvate, 20 mM glucose, 20 mM taurine, pH 7.4 with NaOH) for 5 min to remove all Ca^{2+} to break up the glycocalix. It also results in stopping the cells from contracting. Afterwards cells are isolated enzymatically by changing the perfusion solution for 10 min to Tyrode's solution containing CaCl, collagenase and protease (200 μM $CaCl_2$, 1.0 mg/mL collagenase, 0.1 mg/mL protease). Those enzymes dissolve the inter cellular connections between cells. Ventricular tissue cut from the heart is further incubated into Tyrode's solution (200 μM $CaCl_2$) at 37°C again for 10 min. After triturating the tissue in order to extract single ventricular

myocytes, the suspension is filtered in the following step and afterwards diluted with a solution containing 200 μM $CaCl_2$. For further details see protocol in appendix and [Kong, 2007] as well as [Jayasinghe et al., 2009].

After isolating the ventricular myocytes an immediate fixation is necessary to preserve shape and structure and in particular protein distributions. As the cells are still alive after the isolation process it is advantageous to treat them gently in order to avoid destruction or cell death. A fixation with 2 % paraformaldehyde (PFA, a polymer of formaldehyde) has been proven very successful and compartible with subsequent fluorescent labeling. The very reactive carbonyl group of PFA undergoes reactions with the proteins within the cells, which immobilizes and cross-links them ([Melan, 1995], chapter 8). After fixation and a washing step, cells were stored in a solution containing NaN_3 (400 μl of 10 % NaN_3, 0.2 g BSA and 40 ml PBS), which inhibits bacteria growth. Details are explained in the standard protocol (see appendix: Cell Fixation).
In a good fixation run the striated structure of the myocytes is preserved and the cells remains rod-shaped. Round edges and a grainy pattern is generally an indication for a less successful fixation. Those cells will typically not show a satisfying structure after labeling and imaging.

3.2 Cell Immunolabeling

Immunolabeling is a widely used technique to mark a target of interest within a cell. Antibodies identify a specific target (antigen) and bind to it according to an antigen-antibody reaction. A secondary antibody, having a fluorescent tag, is then able to recognize the primary antibody and binds to it as well. As the size of an antibody is only $\backsim$ 12 nm a very precise localization of the target can be achieved (see [Alberts et al., 2008], chapter 9: Visualizing Cells).
Dependent on the application, different combinations of primary and secondary antibodies were chosen for labeling structures in cells. For multi-color labeling it is important to carefully choose a combination of primary and secondary antibodies: On one hand they should ideally be raised in different species to avoid complications in the labeling protocol and on the other hand, in terms of multi-color imaging, the emission spectra should be easy to separate.

Firstly 2 %PFA fixed cells were permeabilized with 0.1 % Triton X100 for 10 min. Triton X100 creates holes in the lipid membrane, which makes the cell more permeable for the later used antibodies. Then a blocking buffer containing 0.05 % Triton X100 as well as normal goat serum (NGS) was added for one hour. Afterwards the blocking solution was washed off and the primary antibodies, dissolved in the 'incubation solution' (PBS, 0.05 % Na Azide, 2 % Bovine Serum Albumin (BSA), 2 % NGS, 0.05 % Triton X100), were added. The ingredients of the incubation solution include components which support the specific binding of the antibodies. In accordance with prior observed effective labeling dilutions (private communication with Isuru Dilshan), RyR primary antibodies were diluted 1:100, whereas β-tubulin and Caveolin-3 antibodies have been proven to work better at a concentration of 1:500. Cells were then incubated over night at 4°C. After several washing steps the secondary, fluorescent labeled antibodies were applied in a concentration of 1:100 over two hours at room temperature. Three washing steps were performed and finally cells were stored in the storage solution. A range of the commercial available secondary antibodies provides lots of different combinations, which can be used for doub le labels.
Control experiments were following the same procedure except the step, where the primary antibody is added, was excluded. Very little fluorescent labeling was observed compared to regular achieved label intensities in cells when adding only the secondary antibodies. This shows that the secondary antibodies mainly bind specifically to the respective primary antibody.

3.3 Mounting Media

There are several reasons why a biological sample needs to be mounted on the slide in a suitable solution. First of all the biological sample may dry out over time, which will destroy, for example, the cell structure and let cells shrink. Then it is not possible to get reliable information about compartments, distances within the cell or information about protein distributions. Therefore biological samples for microscopy are generally mounted with an environmental solution that favors sample preservation as well as the imaging process. The mounting medium has typically a pH in the physiological range (7.0 - 7.4). In terms of imaging a refraction index match it is often desirable to collect as much light as possible and to minimize aberrations

(see chapter 2: numerical aperture). To avoid high refraction index variations and to minimize aberrations in the PSF, a mounting medium needs to be chosen, which is able to spread throughout the cell and matches the designed refraction index of the objective, immersion oil and cover slip (170 μm thickness, Menzel) as closely as possible.

Besides the requirements mentioned above additional demands in terms of the fluorophore properties are made on the mounting medium. Generally photo-chemical and photo-physical destruction of the fluorophores are not desirable for single molecule detection. As detailed explained in section 2.1.3 photochemical destruction is caused by reactions of the fluorophore with free oxygen in the solution. Therefore oxygen scavenger can be used to remove oxygen in the solution. Alternatively reducing agents can be added to the mounting medium, which remove oxygen as well as recover photoionized fluorophores (see also section 2.1.3).

Based on all these requirements, several different mounting media were tested. The one, which favors the 'fluorophore-blinking' behavior the best and provides a good refraction index match, was chosen for all further experiments. This mounting medium is glycerol based and contains oxygen scavenger as well as reducing agents. The mounting medium contains 80 % glycerol, glucose (10 % w/v), 50 mM β-mercaptoethylamine and the enzymes glucose oxidase (0.5 mg/ml) and catalase (40 μg/ml). Glycerol was used, because it provides a high viscosity and has a refractive index of 1.4729, which is a resonable match to the refractive index of glass (standard cover slip: 170 μm, n = 1.515 see [Nikon, 2009]) and objective or respectively the immersion oil (Zeiss, 518F, n=1.518). Measuring the refractive index of the solution with a refractometer (Atago, Japan) results in a refractive index of n = 1.451, which is expected as the solution is mainly consisting of glycerol and only slightly diluted. This solution was established for all further experiments (see appendix: Switching Buffer and Mounting Medium).

The mixed components of the mounting solution were used only for a few days. Anecdotal observations suggest that solutions older than 1-2 weeks do not support the 'blinking-behavior' of the fluorophores anymore and mounted slides, which were imaged again after a few days, loose quite a lot of their 'blinking'-capability.

Before the actual mounting procedure it is necessary to wash cover slip and slide in a 'cleaning-solution' consisting of sodium hydroxide (NaOH) dissolved in methanol (CH_3OH). Afterwards cover slip and slide are washed in deionized water to wash off the 'cleaning-solution'. It is preferable that cells are in direct contact with the

cover slip too. Therefore 10 μl of poly-L-lysine solution was added to the cover slip, which should help to stick the cells to the cover slip. After 10 min the poly-L-lysine solution is briefly washed off in deionized water and a volume of 20 μl cells in PBS are pipetted on the cover slip. Again after waiting for 10 min the cells should have stuck and the remaining PBS can be removed with filter paper to avoid a dilution of the following mounting medium. The cells were then mounted with 15 μl of the switching-buffer solution and cover slip and slide were sealed with nail polish.

3.4 Microscope Setup

All experiments were performed on a commercially available inverted Nikon TE2000-E inverted microscope (Figure 3.1), which has been extensively modified for high resolution microscopy. Objective holder and stage are directly coupled with each other to reduce thermal and mechanical drift as much as possible. A Nikon oil immersion TIRF objective (Nikon, Japan) provides a magnification of 60x and a numerical aperture of 1.49. Easy manual switching between different dichroic beamsplitters - all mounted in either metal or plastic filter cubes - is provided by a rotatable T-FLC-HQ cassette holder.

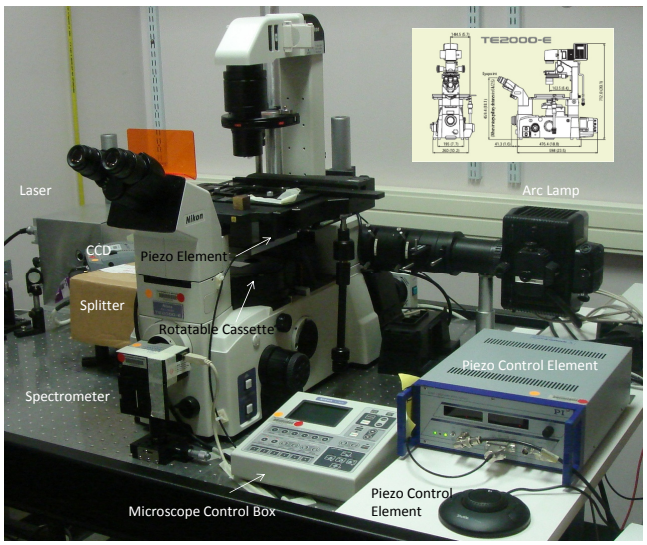

Figure 3.1: Setup: Nikon TE2000-E inverted microscope used for all high-resolution localization measurements. The dimensions of the microscope are illustrated in the schematic ([Nikon, 2004]).

Three different laser lines are provided. Two laser diodes (Viasho VA-I-N-671 and VA-I-LNS-532, China) excite fluorescent samples at a wavelength of 671 nm (red) and 532 nm (green) providing maximal laser output powers of $\backsim$ 800 mW and $\backsim$ 200 mW. Generally the red laser was operating at $\backsim$ 200 mW in nearly all experiments. The third one is an ion laser (Argon, Laser Physics, 150m Ar^+)) operating at a wavelength of 488 nm (blue) and providing $\backsim$ 40 mW. The 488 and 532 lasers can be controlled by a fast shutter (Laser Physics, LST18) manually as well as computer-controlled, whereas the 671 is controlled by a home built slow shutter.
To adjust the illumination angle of the laser, several custom illumination components are provided. Measurements are done with an illumination angle just below TIRF. To run the microscope in TIRF mode flattening of the cells would be needed, which could result in the destruction of cell structures. This is due to the exponential decay of the evanescent wave in TIRF mode, which allows no deeper irradiation than 200 nm. Adjusting the laser to an angle just below TIRF still has the advantage of a low background signal, but also provides an illumination, strong enough to illuminate deeper layers in cells. Table 3.1 lists the dichroic and emission filters used in experiments with the appropriate fluorophores and laser lines.

Table 3.1: This table lists the fluorophores used in this project. The dichroic and emission filters, which were used for each fluorophore are listed as well as the laser line used to excite the dyes.

Dye	Laser Line	Dichroic Filter(1)	Emission Filter
Alexa 488	488	T495LP	ET525/50m(1)
Alexa 532	532	T570LP	ET620/60m(1)
Alexa 568	532	T570LP	ET620/60m
Alexa 594	532	T570LP	ET620/60m
Alexa 647	671	Q680LP	HQ710/50m(1)
Alexa 680	671	Q680LP	HQ710/50m
Alexa 700	671	Q680LP	XF3104,690ALP(2)
Alexa 750	671	Q680LP	XF3104,690ALP

*: Chroma Technology
*: Omega Optics

Additionally the microscope is extended with a highly sensitive piezo element(Physik Instrumente P-725, Germany) to enable focusing in the nanometer range. An Andor IXon DV887DCS-BV electron multiplying charge-coupled device camera (Andor Technology, UK) completes the setup. A vibration-free motorized five-way light port allows to switch between ocular, CCD-Camera and an additionally installed spectrometer. The attached spectrometer (Ocean Optics, USB2000+) was used

for measurements of dye and filter spectra. Labeling checks or spectra measurements have been done in 'metal chambers'. The metal chambers, developed by Isuru Dilshan (University of Auckland) have a cover slip attached on the bottom, which is exchangeable. The advantage is that there is no need to mount the sample beforehand. Spectra measurements benefit from the diffusional replacement of photobleached molecules, which increases the signal immensely.

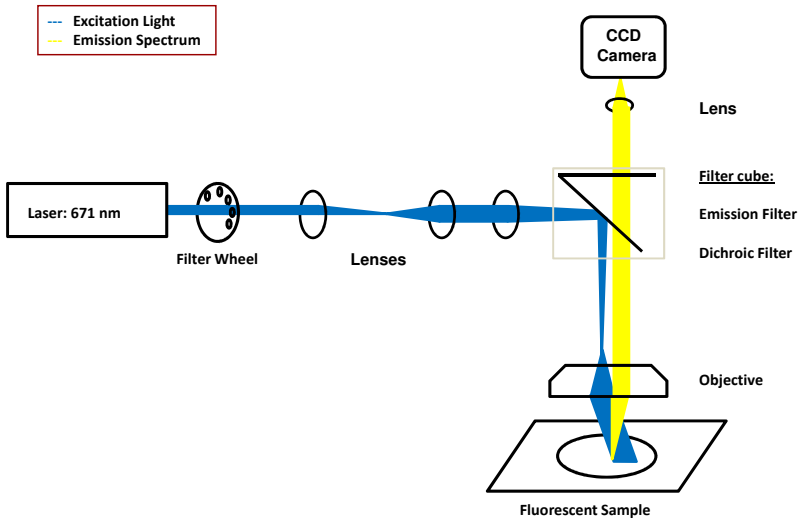

Figure 3.2: Schematic Setup: Nikon TE2000-Eclipse microscope. A laser beam travels through a filter wheel, which allows the intensity to be adjusted. The dichroic beamsplitter reflects the beam on an angle of 45° in the direction of the sample. Passing through the objective the laser beam excites the sample, which as a result emits fluorescent light in the longer wavelength range due to the Stokes shift. The emission light is able to pass through the dichroic beamsplitter as well as emission filter and is then detected on a electron multiplying charge-coupled device camera.

Figure 3.2 is a schematic of the beam path. Two light sources are available: The laser-lines mentioned already above and alternatively an xenon arc lamp. The spectra of the arc lamp can be filtered to the excitation spectrum of the fluorophores, which have been used for labeling. The purpose of the arc lamp is typically checking on labellings with negligible bleaching of the sample at the same time. The intensity provided by the arc lamp is typically much lower than the laser intensity and therefore generally not strong enough to push dyes effectively in a dark state. First of all the laser beam passes through a filter wheel, which provides variable attenuation with different neutral densities. A high neutral density filter allows to

illuminate and select a certain part of the sample with little bleaching during this time. As a result of the highly reduced laser intensity 'blinking' is generally not observed. Exposing the sample with the filter setting on empty results in high laser intensities, which enables pushing most of the fluorophores in the 'dark-state'. The 'blinking-behavior' necessary for high resolution localization microscopy can then be observed. After passing the filter wheel, the laser beam enters the microscope itself. There the beam is widened by a couple of lenses and reflected by a dichroic beamsplitter in the direction of the sample, passing through the objective and illuminating the sample with a spot size of $\backsim$ 10 μm.
The emitted light of each fluorophore travels through the objective, passes through the dichroic beamsplitter and emission filter exploiting the stokes shift of the emission spectrum. The emission filter is of a higher optical density in the blocking regime and rejects any excitation light that was able to pass through the dichroic beamsplitter. By using this additional emission filter it is ensured that no laser light, which is generally of much higher intensity than the fluorescent light, hits the CCD-chip, which can cause a potentially overexposures of the chip and also a drowning of the fluorescence signal. Finally a lens focuses the fluorescent light in an image plane, where the CCD-Chip is placed.

3.5 Imaging

PYME Acquire

Figure 3.3 shows the user interface of the fitting software PYME written by Dr. David Baddeley (University of Auckland) in the software environment of the python programming language. The very sensitive piezo element allows to focus on the sample in the nm range under software control (see control panel (1) in figure 3.3). Ideally a focus near the cover slip interface is chosen. On the left side a viewer panel (2) shows the sample in real time. For imaging it is useful to select a Region Of Interest (ROI) to restrict the amount of data and match the illumination spot size of the laser. The spot size is nearly a quarter of the CCD-chip (512 x 512 pixels). One pixel is 70 nm, which allows to record an area of $\backsim$ 300 μm^2. The display (3) optimizes automatically the visual appearance of the viewer by adjusting the range between the minimal and maximal gray values of the image on to a scale of 256 gray values. The first setting that needs to be done is cooling the CCD-chip (5) of the camera

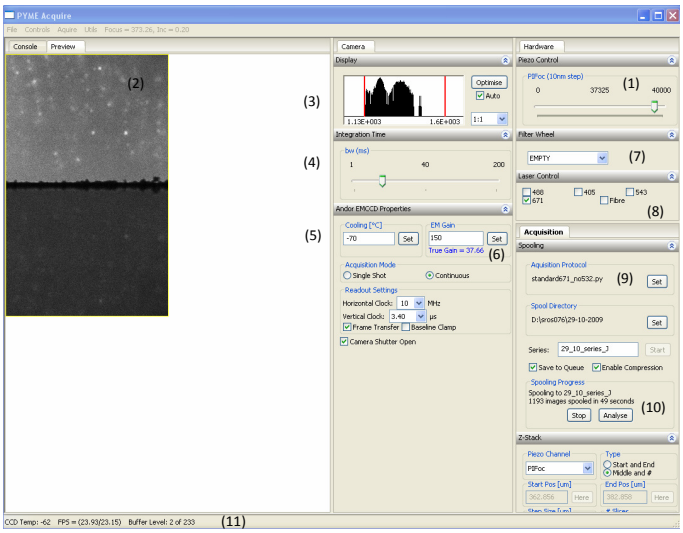

Figure 3.3: The fitting and analyzing software PYME written by Dr. David Baddeley (University of Auckland) provides a user friendly interface. All parameters for data acquisition can be easily set compatible to the respective application as well as analyzing parameters. Numbers are referring to further explanations in the text.

down to -70°C to reduce the read-out-noise and to avoid thermal photons as much as possible.

Before starting the high-resolution imaging sequence a wide field image is saved for comparison with later acquired high resolution images. For this purpose a high neutral density filter (7) is chosen because of reasons mentioned above. The widefield images are typically acquired with an integration time of $\backsim$ 300 msec, a suitable electron multiplying gain (em-gain) and then saved as a kdf file (khoros data format). Additionally, before starting any recording, the laser intensity is checked with a power-meter in the beam path to ascertain a repeatable laser intensity for all measurements.

The following procedure describes a typical image acquisition: A 'prebleaching' of the fluorophores with a filter setting on empty (7) is essential before starting the recording. For this purpose no em-gain is applied and the sample is exposed to the full laser power, which will be applied in the recording. The laser control panel (8) allows the user to select between different lasers - each suitable for certain fluorophores. This step is necessary before the CCD-chip is exposed to the fluorescent light with a high em-gain in order to avoid over-saturating the chip.

Then several settings have to be done before the actual acquisition. Integration time (4) and em-gain (6) are chosen after taking the 'blinking-behavior' of the fluo-

rophores in account. The integration time is chosen according to the typical 'on-time' of a fluorophore, which is generally 27 msec or 40 msec depending on the laser power as well as on the chemical environment. The em-gain is set to 150, which is an actual multiplying factor of $\backsim$ 33 (see chapter 4: results and discussion).
After the 'prebleaching' and adjusting the final settings, a protocol (9) can be selected. When starting the acquisition this protocol automatically saves necessary information about the settings needed for analysis of the data. Frames are stored consecutively in an HDF5 file (Hierarchical Data Format) a format, which is used to store scientific data ([HDF5Group, 2009]). Besides the raw data this format also saves supporting metadata as well as events, which happen during the recording (for example: focus changes). A typical acquisition takes a minimum of 10,000 frames to a maximum of 20,000 frames, where the original rate of 'blinking' fluorophores has generally dropped down to 5 %. Usually around 5 min are needed to achieve a good high resolution image.

Data Analysis and Image Reconstruction

The real-time analysis is automatically started by the chosen protocol or by pressing the 'analysis'-button on the software interface (10). It is also possible to analyze the data offline. Each frame including all its detected events is analyzed individually. Background values for each event are evaluated by averaging over 10 frames before an event occurs and then subtracting this value. A bandpass filter, whose frequency is chosen according to the expected frequency spectrum of the fluorophores (spot size: FWHM of the Gaussian) smooths the difference image. Then a local variable threshold is applied to the image to isolate the single molecule events. This threshold is an estimate of the photon-counting-noise in each pixel (standard deviation of the Poisson distribution) multiplied with a scale factor chosen by taking integration time and em-gain into account (see figure 3.4 (2) and [Baddeley et al., 2009b]).
A standard labeling algorithm selects the events from the thresholded image, numbers those consecutively and calculates the center of intensity, which gives the starting coordinates for the fitting process. The localization of each fluorophore is then estimated by fitting a Gaussian model function:

$$f(\vec{x},\vec{y}|A,\sigma,x_0,y_0,b,b_x,b_y) = A\cdot e^{-\frac{(x-x_0)^2+(y-y_0)^2}{2\sigma^2}} + b + \frac{\delta b}{\delta x}(x-x_0) + \frac{\delta b}{\delta y}(y-y_0) \quad (3.1)$$

with $b_x = (\frac{\delta b}{\delta x})$ and $b_y = (\frac{\delta b}{\delta y})$. The fitting function $f(\vec{x}, \vec{y}|\vec{p})$ consists of a 2D Gaussian term and is extended with three additional terms. The first one is a constant describing the background level, followed by two terms taking weak gradients of the background into account.
This model function is fitted to a 15 x 15 pixel ROI extracted at the position of each detected event. The fit is performed using the Levenberg-Marquardt algorithm ([Levenberg, 1944],[Marquardt, 1963]) implemented in Scipy to solve the weighted least squares problem ([PythonSoftwareFoundation, 2009]):

$$\left|\left| \frac{f(\vec{x}, \vec{y}|\vec{p}) - \vec{d}}{\vec{w}} \right|\right|^2 \tag{3.2}$$

with $\vec{p} = (A, \sigma, x_0, y_0, b, b_x, b_y)$ and $\vec{d}$ representing the raw data. The numerator is the difference between the intensity values generated by the model function and the actual data intensity values. The whole expression is 'weighted' by the vector $\vec{w}$, which is the standard deviation of each pixel:

$$\vec{w} = \sigma_{readout-noise} + \sigma_{photon-counting-noise} + \sigma_{electron-multiplying-noise} \tag{3.3}$$

The error introduced by each pixel consists of two components: 'Read-out-Noise' and 'Photon-Counting-Noise', which is assumed to be Poisson distributed. Therefore $\sigma_{poisson}$ is replaced by $\sqrt{N_{Photons}}$, the standard deviation of the Poisson distribution. Minimizing this expression leads to a Gaussian intensity distribution, whose center approximately localizes each single molecule event.
The starting values for the fit are calculated as follows: The position values are obtained by the center of intensity calculation. The intensity amplitude A is the maximum value subtracted by the minimum value. The starting value for the background is the minimum intensity value. Gradients in the background level are assumed to be zero. Sigma is the expected standard deviation of an $\backsim$ 250 nm spot.

Figure 3.4 shows the real time analysis of the recorded data (1). Before starting the analysis the fitting algorithm described above is chosen (3) as well as the scale factor (2), a number that adjusts the threshold level. The event detection rate drops quite

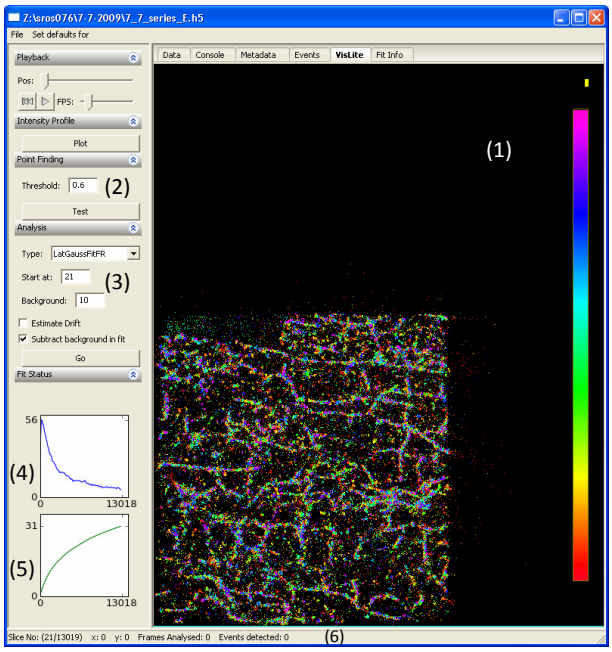

Figure 3.4: Time delayed analysis of the original data. Single molecule events are analyzed by a least squares function, which fits a Gaussian model function to each event (LatGaussFitFR). A suitable scale factor has to be chosen beforehand. In the bottom line the sum of all detected events is placed just as the number of already analyzed frames (6). Numbers are referring to further explanations in the text.

fast at the beginning of the recording due to photobleaching, but then the decay slows down distinctly. When the cumulative event detecting reaches a plateau (5) the image acquisition is terminated. Typically 10^5 to $2 \cdot 10^5$ events where recorded at this stage.

Further analyzes are done offline. Data can be filtered by choosing appropriate boundaries for each variable of the fitting process (see figure 3.5, filter panel). This leads to images, which exclude erroneous data points. The display shows the distribution of the variable selected for each detected single molecule event, which are color coded (see color bar on the right side). The yellow bar in the magnification presents 200 nm.

After applying the filter process fluorophore density images are reconstructed from the evaluated coordinates of the single molecule events. As the analyzed data, which is sampling limited, shows only the distribution of the single molecule positions (see

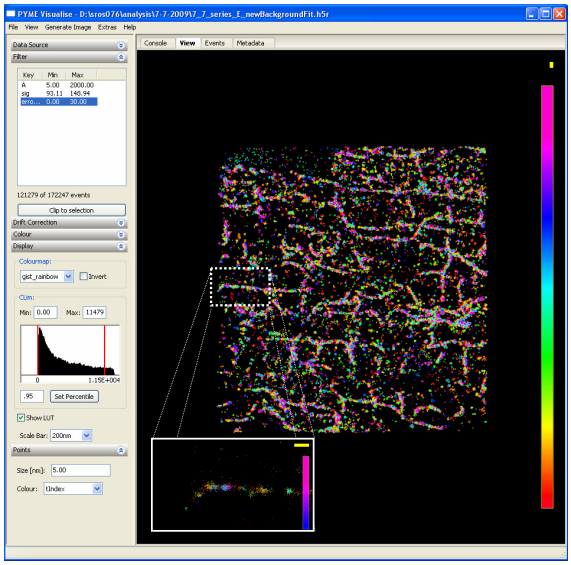

Figure 3.5: The analyzed data can be edited by filtering. Depending on the chosen filter, the display shows a distribution of the selected variable for each event. Here the variable 'tindex' is selected, which shows the appearance of the events over the time of acquisition. The filtering process is demonstrated with labeled β-tubulin (Alexa 680) in ventricular myocytes.

figure 3.5). A better visualization can be achieved by translating the analyzed coordinates into a conventional image. For this purpose a number of visualization methods are available. The most widely used visualization method is a Gaussian rendering. Each analyzed single molecule position is rendered by a Gaussian, which has its intensity peak at the fluorophore position and a width equal to the localization error. This results in intensity images, where intensity is translated into density of the fluorophores detected in this area. Further details and disadvantages of this method are explained in [Baddeley et al., 2009a]. An example for Gaussian rendering is demonstrated in figure 3.6 on the left side. Gaussian rendering is applied to the same data set as shown in figure 3.5: β-tubulin is labeled with Alexa 680 in ventricular myocytes. The width of the Gaussian is then $FWHM = 2.35 * \Delta x$, where Δx is the localization error.

Another method generally used during this project and preserving a better effective resolution is Delaunay triangulation, which is applied to the data points connecting those by triangles. Then the intensity of each triangle is calculated according to the area included by the triangle. The smaller the area, the higher the intensity, which is translated to a higher localization accuracy ([Baddeley et al., 2009a]).

An example image after triangulation is shown in figure 3.6 on the right side. De-

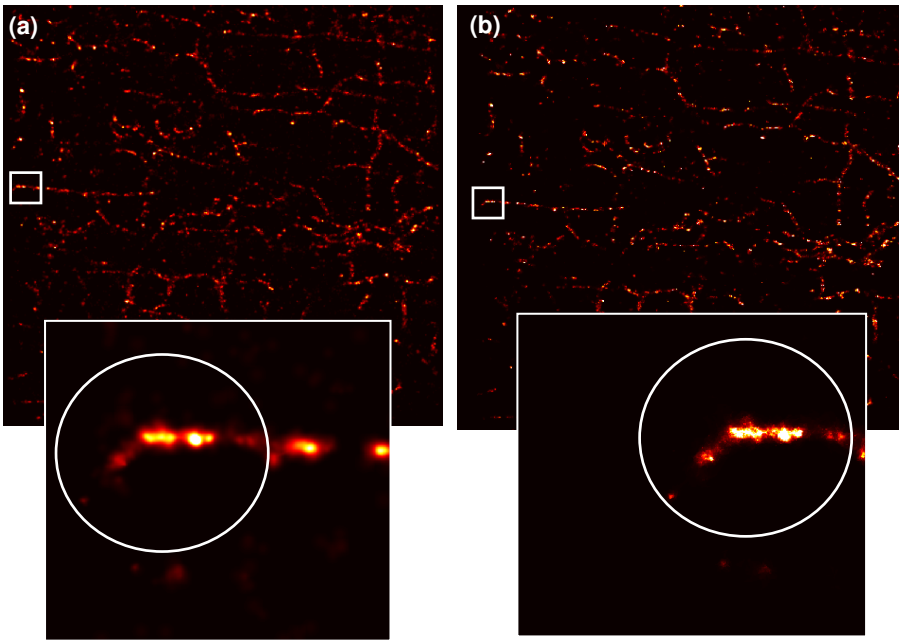

Figure 3.6: The two different visualization methods explained in the text are demonstrated on β-tubulin labeled cells. The left side shows the Gaussian visualization method. The image is generated by rendering each event as a Gaussian with a standard deviation equal to the localization error Δ_x. In comparison on the right side the triangulation method is demonstrated by rendering the molecule coordinates with mean neighboring distance. Smoothing is done by an adaptive jittering method ([Baddeley et al., 2009a]).

launay triangulation was applied to the same data set as used for the Gaussian rendering. After the triangulation process the image was rendered with the median of the distances to the nearest neighbor evaluated in the triangulation process.
Smoothing of the sharp intensity transitions between triangles is done by an adaptive jittering method. This is a simulation method, which jitters each point randomly by half of the mean neighboring distance and ten differently jittered images are averaged. Very dense packed areas of single molecule events are therefore much less jittered than areas, where only a very sparse number of events is detected. The result is less blurring in areas of higher molecule density, which maintains the local resolution, whereas in areas of lower sampling higher blurring translates automatically into sampling limited accuracy ([Baddeley et al., 2009c] and [Baddeley et al., 2009a]).

Chapter 4

Results

As single molecule detection and the localization precision are very sensitive to every introduced noise source, a brief analysis of the noise characteristics of the CCD-camera, used for all experiments carried out, is presented. These results are taken into account to estimate the localization error correctly. Achieved localization precisions are compared to expected values calculated on the basis of a formula given in the literature.
With the goal of multi color imaging several commercial available Alexa fluorophores are tested for their applicability in RPM. Based on the results of this study, changes on the RPM setup have been conducted in order to enable visualizing two different protein distributions in immunolabeled cardiac myocytes. The changes in the microscope setup and the necessary adaptations in the analysis software are explained. The methodological as well as the biological results will be presented.

4.1 CCD-Camera Characterization

Single molecule detection circumvents the diffraction limit and may lead to a ∽ten times higher resolution, but there are still limiting factors that influence the localization accuracy. As high resolution microscopy deals with low light intensities, any noise affects the localization precision negatively. Besides background noise (out-of-focus fluorescence, autofluorescence), which produces an offset in the first place, the detection of the photons on the CCD-chip and the following read out process introduces additional noise. Since the mean magnitude of a noise source is always equal to zero, noise is qualified as the standard deviation of the fluctuations.

Noise sources of a CCD can not be eliminated completely, it is therefore important not to neglect those factors, but to estimate them correctly in order to evaluate a correct localization accuracy of single molecule events. Read-out noise and electron multiplying noise are measured and the obtained values are used in later analyses. The dark current, a noise source as well, is typically insignificant in comparison with the two other noise sources, while cooling the CCD-chip at -70°C as it was performed for all measurements. A new calibration of the electron multiplication gain will be performed as well.
Photons detected by the CCD-chip are converted into counts during the read-out process. Counts translate into intensities resulting in a generated intensity image. As the error estimates in the fit algorithm are based on the actual number of photoelectrons detected, a conversion from the number of counts per event into the number of detected photoelectrons is conducted. For this purpose the conversion factors specified in the CCD manual ([AndorTechnology, 2005]) are used (see table 4.1). The additional factor 2.4 is caused by a preamplifier setting of 2.4. Before

Table 4.1: Conversion of counts evaluated by the CCD read out process into electrons and photoelectrons at a preamplifier setting of 1.

1 A/D-Count	=	$2.4 \cdot 27.32 = 65.57$ Secondary Electrons
1 A/D-Count	=	$\frac{2.4 \cdot 27.32}{EM-Gain}$ Photoelectrons

calibrating the electron multiplying gain as well as evaluating the noise characterizations in the following section, recorded data is always converted into photoelectrons or electrons, depending where the noise occurs during the read-out process.

This part of the thesis characterizes the noise sources of the CCD camera used in all experiments and their importance for detection are evaluated.

Read-Out Noise

Read-out noise is introduced in the conversion of a analog signal consisting of photoelectrons (voltage) into a digital signal (counts). Reading out the same pixel twice will produce slight variations in the absolute values. To estimate the read-out noise a series of 100 frames is recorded using an integration time of 27 msec while the

camera shutter is closed. No electron multiplication was used during the measurement. Counts are converted into electrons according to table 4.1. A mean image is generated by averaging each pixel over 100 frames and then calculating the standard deviation for each pixel, which is equal to the read-out noise. The mean read-out noise for all pixels (mean of all standard deviations) is listed in table 4.2.

The CCD manual quotes a maximal variation of 109.8 electrons in the total number per pixel for each read-out process. The calculation shows only a slightly higher number of electrons and is therefore in good agreement with the value measured by the manufacturer. The dark current mentioned in the theory (see section 2.1.7) can

Table 4.2: The calculated read-out noise per pixel is slightly higher than the value quoted in the CCD manual. All further analysis in this thesis are conducted with this evaluated read-out noise.

Read-Out Noise/Pixel	
CCD Manual	109.8 e^-
Calculation(1)	146.87 e^-

(1): value used in all further analysis

be neglected, because it ranges in dimension far below the read-out noise (0.000438 electrons/pixel/sec at -50 °C [AndorTechnology, 2005]).

Electron Multiplying Calibration

For conversion of A/D-Counts into photoelectrons the 'True EM-Gain' needs to be calibrated. The software setting of 150, which is used for all imaging performed, is translated by the camera hardware into a gain-register voltage and is not the actual electron multiplying factor.
To evaluate the correct multiplication factor a series of 100 frames with a constant illumination source were recorded - once with an em-gain setting of 0 and once with a setting of 150. To estimate the A/D-offset the same series was recorded again, but this time with the camera shutter closed. It was assured that operating temperature and integration time are the same for each measurement. The offset was evaluated by generating a mean image over the 100 frames recorded with the camera shutter closed and calculating the mean pixel value. The A/D-offset for the different em-gain settings are listed in the table 4.3. The offsets are subtracted from the data recorded with a constant illumination. For the calibration of the electron multiplying factor a

Table 4.3: This table lists the A/D-offsets evaluated once for an em-gain setting of zero and once with 150.

Software Setting	A/D-Offset [counts]
0	1058
150	1089

conversion into photoelectrons is not necessary. The mean images are generated over a series of 100 frames for both em-gain settings. The ratio of the given mean values calculated from the mean images (em-gain setting 0 and 150) is the em-gain. The evaluated electron multiplying gain, shown in table 4.4, is 33 secondary electrons per detected photoelectron. Read-out noise occurs after the multiplying process in the CCD-camera and is therefore less relevant(see section 2.1.7).

Table 4.4: The calibration of the em-gain maintained a electron multiplication factor of 33 secondary electrons per detected photoelectron. The evaluation is explained in the text.

Software Setting	EM-Gain
150	33

Electron Multiplying Noise

The disadvantage of electron multiplication is that this process also introduces noise. The noise factor F is defined by the ratio of the variances of the output signal divided by the input signal multiplied with the mean electron multiplying gain M ([Robbins and Hadwen, 2002]):

$$F^2 = \frac{{\sigma_{out}}^2}{M^2 {\sigma_{in}}^2} \tag{4.1}$$

If the electron multiplication process introduces no noise, the noise factor F will be unity, but it has been established that a noise factor of $F = \sqrt{2}$ occurs ([Robbins and Hadwen, 2002]).

To check the electron multiplication noise factor a graphical solution is presented. The same series recorded for calibrating the em-gain is consulted. Likewise the A/D-offset (see table 4.3) is subtracted and counts are converted into photoelectrons according to formula shown in table 4.1 with a value of 33 for the em-gain

evaluated beforehand (see table 4.4). A pool of pixels with nearly the same amount of photoelectrons collected, is selected out of the data. The distribution is shown as a histogram in figure 4.1 (blue).

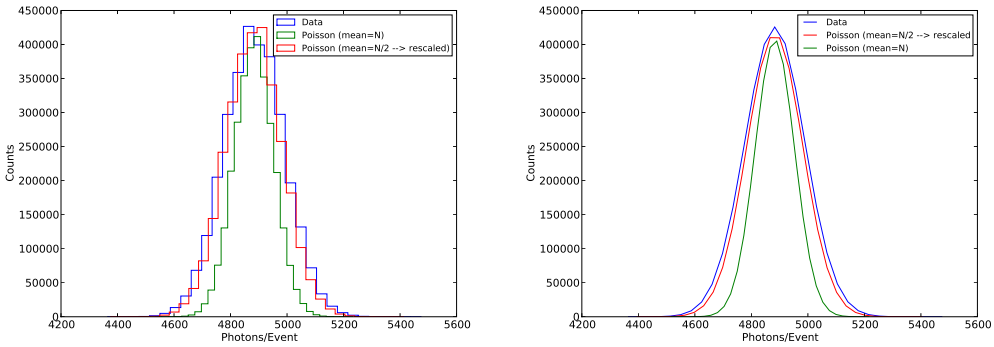

Figure 4.1: The actual data is compared with a generated Poisson distribution once with the same mean value of photoelectrons and once with half the number of photoelectrons (rescaled with a factor 2). It is clearly that the noise factor F is not unity but approaches a value of 1.4 very well. The still slightly broader FWHM is assumed to be due to read-out noise and noise introduced by flickering of the illumination source during the recording, which can be correlated. For better illustration the curves fitted to the histograms are extracted into a separate diagram.

Noise can be modeled as a Poisson distribution (see section 2.1.7). Therefore a theoretical Poisson distribution with the same mean value as the data can be generated (green) and compared with the recorded distribution. For better illustration a curve is fitted to the histograms and extracted into a separate diagram also shown in figure 4.1. Noise always results in a broader distribution, because the variances of the fitted distribution and the introduced noise sum up. Thus the em-gain noise can be estimated by subtracting the variances of both distributions and extracting the square root.

If no noise was introduced by the electron multiplying process, the curves would overlay. If the noise factor was unity, the distribution of the data (blue curve) would have the same standard deviation of 70 as the generated Poisson distribution (green curve). To consider a factor of $F = \sqrt{2}$ a Poisson distribution with a mean value of half of the photon number was generated ($\frac{N}{2}$) and rescaled (red). This distribution (red curve) agrees much better with the data (blue curve). To compare the curves more accurately the standard deviations of the three distributions were calculated and listed in table 4.5.

The ratio of the standard deviations is an estimation for the electron multiplying noise: $\frac{\sigma_{Data}}{\sigma_{Poisson}} = 1.52$. The ratio for the standard deviations of the two generated

Table 4.5: Evaluation of the electron multiplying noise. Assumed noise factors of unity and 1.4 are compared with the measured data by simulating a Poisson distributions, which take those into account. A noise factor of 1.4 approximates the measured standard deviation the best. The remaining difference is assumed to be due to read-out noise and noise introduced by flickering of the illumination source during the recording, which can be correlated.

Mean(1)	Standard Deviation(1)
Data Distribution ($\overline{N}$)	106.12
Generated Distribution ($\overline{N}$)	70
Generated Distribution ($\frac{\overline{N}}{2}$)(2)	98.76

(1): data in photoelectrons
(2): rescaled with a factor 2

Poisson distributions is close to a factor of $\sqrt{2} = 1.4$ as expected ($70 * \sqrt{2} = 98.76$ photoelectrons). A good agreement is shown, when comparing the standard deviations of the generated Poisson distribution, which includes the noise factor, and the data. The slightly difference may be explained by noise introduced by flickering of the illumination source during the recording, which is not taken into account in this consideration.

Read-out Noise, the calibrated electron multiplication gain and electron multiplication noise, gained in these analyses, are included into the fitting algorithm explained in section 3.5.

4.2 Event Analysis of the fluorescent Alexa Dyes

Fluorophores used in single molecule detection need to fulfill a range of requirements to be suitable for imaging techniques like RPM and STORM. Here a range of commercially available Alexa fluorophores were tested for their 'blinking-behavior', the compatibility in a oxygen depleted environment and which combinations can be used for multicolor labels. The labeled structures were Caveolin and RyRs in ventricular myocytes.
As described in section 3.3 cover slip and slide were washed before use for imaging. This cleaning process was necessary as high fluorescent background was observed on uncleaned cover slips. The washing removes most of the fluorescent contaminations, which are suspected to be dust or coating chemicals due to manufacturing.

Afterwards the background fluorescent level was highly reduced compared to measurements excluding a washing step in the sample preparation.
Sometimes cells were only mounted in PBS for fluorescence microscopy use. Alternatively glycerol was used, because it matches the refractive index of the immersion oil and the cover slip better. In recent publications it was suggested to use an oxygen depleted environment ([Heilemann et al., 2008]) for single molecule detection. To test, which environment favors the 'blinking-behavior' of the fluorophores, a few different mounting media were tested using the Alexa fluorophores 488 and 647.
PBS only mounted slides showed less single molecule events and a rapid decay in the 'blinking-rate' (data not shown). After 1000 frames nearly no event was detected anymore. Glycerol only mounted samples provided a reasonable 'blinking-rate' for Alexa 488, but seemed to have little effect on Alexa 647. A chemical environment, which is PBS based, but containing the oxygen scavenger glucose oxidase and catalase and additionally the reducing agent β-mercaptoethylamine as suggested in [Heilemann et al., 2008] provided a very good compatibility with Alexa 647. Alexa 488 was also showing a good 'blinking-behavior' but the switching between a bright (on) state and a dark (off) state was much faster than for Alexa 647. Mixing oxygen scavenger and reducing agent with glycerol provided a satisfying chemical environment for both Alexa dyes. Photobleaching was highly reduced. Therefore for all further experiments the chemical environment was the glycerol based oxygen depleted solution described in section 3.3.
After deciding, which mounting medium will be chosen for further experiments, the 'blinking-behavior' of the different Alexa dyes was analyzed. For this purpose single molecule events were recorded all with the same microscope setup. Only the dichroic and emission filters were swapped depending on the excitation and emission spectra of the fluorophores and an appropriate laser source was chosen to excite the dyes (see section 3.4 table 3.1).
The raw data series were resliced in ImageJ, an image processing program. The generated 8 bit images show x-position against time. A representative selection of the data for each Alexa fluorophore is shown in figure 4.2. As the far-red dyes show a similar 'blinking-behavior', only Alexa 647 is illustrated representatively. Typical events were selected and their profiles are plotted against time. An offset is estimated and subtracted. The duration of a single molecule event is given by the profile width at half peak height (FWHM).
An example of Alexa 647 is illustrated in (4.2 (I)). Multiple events of the same

fluorophore are clearly separated from each other and therefore well detected. The 'on-time' is consistent with the integration time (27 msec) and provides high photon numbers, which let those stand out clearly from the background. Generally one event lasts 1 to 3 frames, which is equal to 27 to 81 msec. Similar results have been obtained for Alexa 680, 700 and 750 Alexa 647, but are not shown here.
In comparison with Alexa 647 the other tested Alexa dyes (488, 532, 568, 594) indicate different characteristics. Alexa 488 (4.2 (II)) blinks so fast that one event mostly does not last a frame. This is problematic in terms of detection when using an integration time of 27 msec. The measured intensity will likely be drowned in the background fluorescence. Another disadvantage that occurred is the fast bleaching of the dye, especially when not mounted in a glycerol based solution. It is impossible to extract an event for Alexa 532 (4.2 (III)) in the used chemical environment and the underlying labeling procedure. The dye molecules seemed to stay 'on'. But the detection relies on recognizing 'blinking', not a permanent bright fluorophore. Additionally high autofluorescence in fixed cardiac myocytes, which produces a yellowish background, makes it even more difficult to extract a signal for Alexa 532. The conclusion is that Alexa 532 is not very useful for single molecule detection at last with the media tested here. Alexa 568 and 594 exhibit a mixture of the two phenomena. Fast 'on' and 'off' switching seems to be combined with events, which stay in a bright state for quite a lot of frames. This observation is illustrated in figures (4.2 (IV)) and (4.2 (V)).

In summary Alexa 647 and the other far-red dyes seem to be promising choice for the purpose of single molecule detection and two color imaging, especially the fact that all far red dyes can be excited with the same laser line. All other Alexa dyes cause more problems in the detection. Whether the events are staying on for a long time or switching too fast between 'on' and 'off' can not be distinguished based on the data. However, the acquisition we used in the current analysis is not able to detect these events. An additional problem in the detection may be the autofluorescence caused by the cell fixation, which is excited by the same wavelength as for example Alexa 532. Autofluorescence is generally highly reduced using a far-red excitation, which leads automatically to better localization precisions.

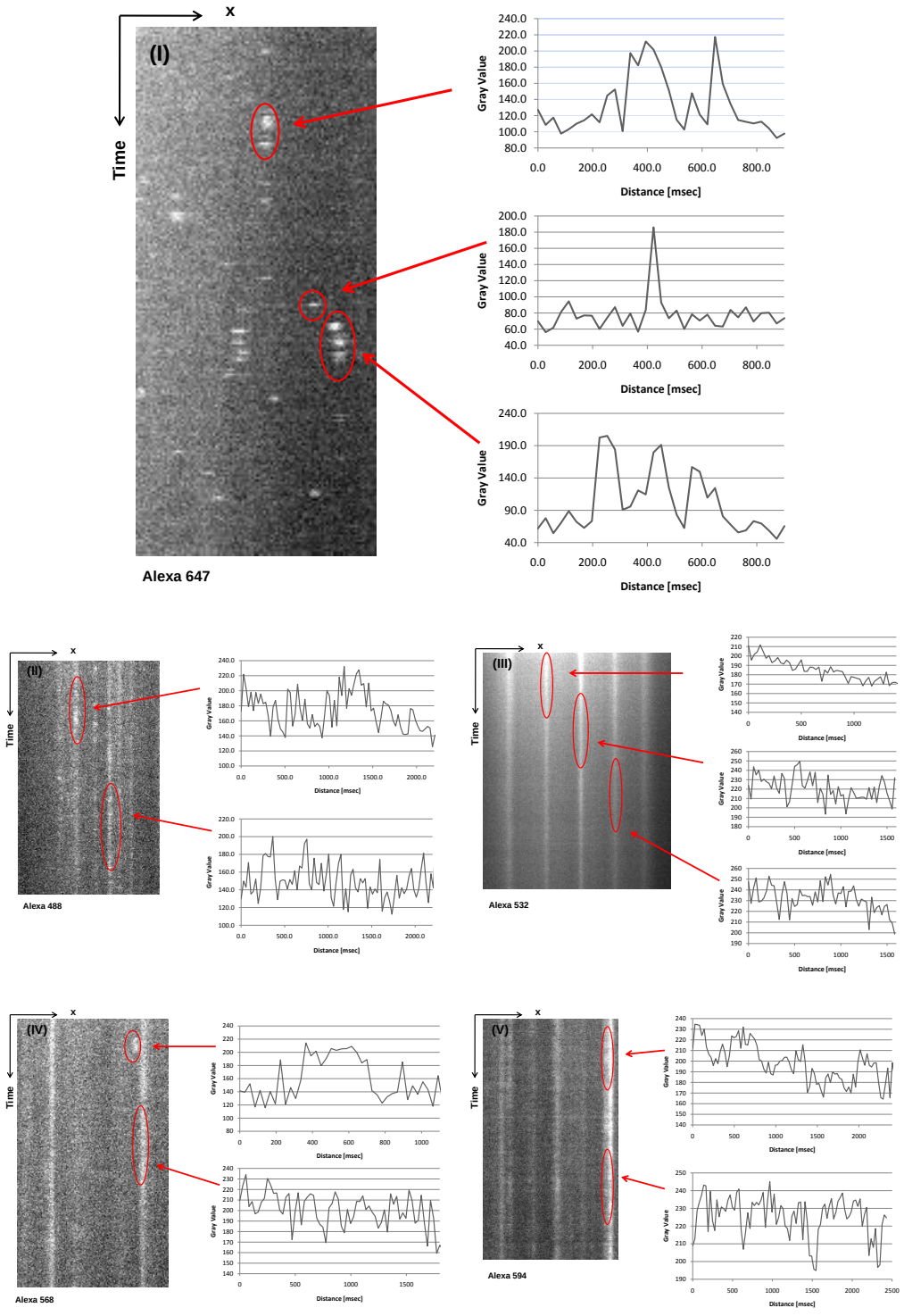

Figure 4.2: A representative selection of each Alexa fluorophore is shown. The original data is resliced in ImageJ. The x-y axis plotted against time. Each pixel is equal to 27 msec on the time axis. Single molecule events occur as bright pixels. Depending on how many frames an event last, it is spread over several pixels. Typical events of each fluorophore are selected and their profiles plotted. The FWHM of a single molecule event specifies its duration. As the far-red dyes show similar characteristics, only Alexa 647 is presented.

4.3 Localization Accuracy

As the infrared dyes have shown the best 'blinking-behavior' in the previous section, further analysis was conducted. In this section the characteristics of the far-red dyes will be worked out in terms of localization accuracies, photon numbers per event and background that can be expected.

In section 2.1.6 a theoretical localization prediction for single molecule events was explained. To check how good the localization prediction of the Gaussian fitting algorithm and the formula 2.16 agree, 10 representative events were selected from a raw data set. Three representative frames of the raw data set, which will be analyzed in this section, are extracted from the raw data and presented in figure 4.3. The first one is extracted out of the first recorded frames, where the structure is still visible and many single molecule events are in the bright state at the same time. For single molecule detection less events are preferable, whose PSFs do not overlap. Otherwise these can not be separated and the detection will recognize them as one event. Frames with event densities too high for separation of single molecule events are typically removed from the analysis. The second and third image show frames at a later stage. Clearly visible single molecule events can be extracted.

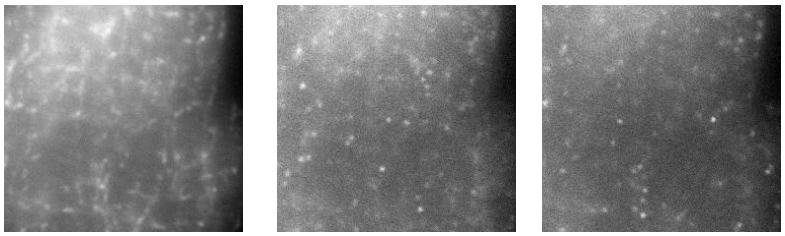

Figure 4.3: Representative frames are extracted out of the raw data analyzed in this section. The first image is an earlier frame, whereas the other two are presenting frames at a later stage of the recording. In the early frame is the structure labeled still visible, which is due to many fluorophores are in the bright state at the same time. For a successful single molecule detection less events, whose PSFs do not overlap, are preferable. This is illustrated in the later frames.

To evaluate these events the frame is read into ImageJ. An offset of 1089 counts (see table 4.3) is subtracted and counts are converted into photoelectrons (see table

4.1). The offset was evaluated immediately before the data was recorded. A profile plot of the event was used to estimate the FWHM and the resultant σ_{PSF} (see equation 2.17). After the conversion intensity measurements yield photon numbers per event and background photons per pixel. The values estimated for photoelectrons, background and σ_{PSF} are then imported into formula 2.16. The results for the localization error and the corresponding photon numbers per event are then plotted in figure 4.4 (red: theoretical results based on measured values in imageJ). The values estimated by the fitting algorithm are also read into the formula and plotted for comparison (green: theoretical results based on the estimated fit values) as well as the fitting results themselves (blue: fit results). A least squares fit ([Scipy, 2009]) was performed for each data set for better illustration. The results of the theory (red and green line) are nearly always lower than the estimated fitting error (blue line), but the tendency is nearly the same. Further evaluations are not possible with this small amount of data points. The purpose of this analysis is to illustrate that the fitting algorithm achieves similar results as a manual evaluation would achieve.

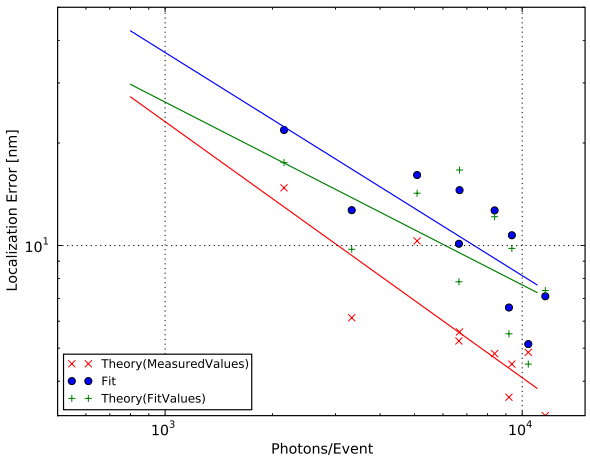

Figure 4.4: A selection of events is evaluated in ImageJ in regard to photon numbers per event, background and FWHM. Based on these values the theoretical localization prediction is calculated using formula 2.16 (red). In comparison the results of the fit algorithm are shown (blue) and additionally the results of the theoretical calculation based on the data gained in the fitting process is plotted (green). A least squares fit ([Scipy, 2009]) was performed for each data set to illustrate the tendency of the localization error in dependency of the photon number per event. A more detailed explanation can be found in the text.

As the evaluation of the characteristics of the fitting process should be based on more than 10 data points, a whole data set was analyzed and evaluated in terms of

localization precision, photon numbers per event and background influences on the detection.

Two parameters, photon number and background fluorescence are the most critical in determining whether single molecule events can be detected and influence the subsequent estimated localization error mainly. The data, analyzed in PYME (see section 3.5) automatically saves all information for every detected event. This includes estimations of photoelectrons per event, estimated error in localization, background values and time dependency. A short script, written in python, was developed to extract the distribution of interest from the analyzed data and compare those with expected distributions. The evaluated amount of photoelectrons per event, background photoelectrons per pixel and the standard deviations of the PSFs are automatically read into equation 2.16 after the count-to-photoelectron conversion (see section 4.1). The background b in this equation is estimated by formula 2.18, where read-out noise and em-gain are replaced by the values shown in table 4.2 and 4.4.

For the evaluation of the characteristics of the fitting algorithm a representative data set of Alexa 680 was selected and evaluated. The structure labeled was β-tubulin in cardiac myocytes, which has proven to be a robust labeling antibody and therefore was used for all measurements, which deal with the characteristics of the fitting process. Figure 4.5 illustrates the most important factors for the fitting procedure, extracted from the data as mentioned above. The histograms in the first row show the distribution of the localization error for the single molecule events given by the fitting algorithm (a) and the predicted localization accuracy (b). (c) and (d) illustrates the distribution of photoelectrons per event and the background per pixel. The marked area in (c) displays that $\frac{1}{3}$ of all detected events consists of more than 4000 photons. Similar distributions have been extracted from the analyzed data for the other far-red Alexa dyes. A comparison of all far red-dyes will be given in later sections.
The mean values and the corresponding standard deviations are calculated from these distributions. Table 4.6 lists the results of the evaluation. A mean estimated fit error in localization of 14.95 nm results in a resolution of $\Delta x \cdot 2.35 = FWHM = 35.13\,nm$. In contrast a theoretical mean error of 11.34 nm would provide a resolution of $\Delta x \cdot 2.35 = FWHM = 26.65\,nm$. This is at least a difference of $\backsim$ 10 nm or

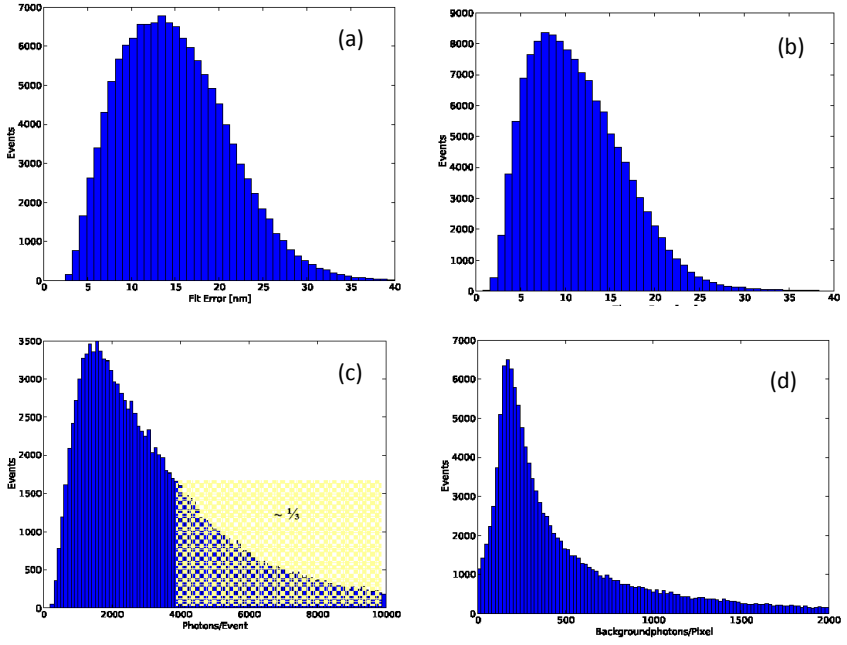

Figure 4.5: Characterization of Alexa 680: Histogram (a) shows the distribution of the localization error given by the fitting. In comparison (b) shows the predicted localization accuracy calculated with the formula. The achieved photo-electron numbers are illustrated in (c). The colored area displays $\backsim \frac{1}{3}$ of the events, which have photon numbers ≥ 4000. (d) shows the background photons per pixel.

a estimated fit error, which is $\backsim 24.15\,\%$ higher than the predicted error. Therefore a direct comparison between the theoretical error in localization and the error evaluated by the fitting process is shown in figure 4.6. For better illustration a regression line is fitted to the data by performing a least squares fit ([Scipy, 2009]). The color represents density. Most of the detected single molecule events are located in the red area. The theoretical approach results in an estimate, which is smaller than the error estimated in the fit algorithm, reflected in a gradient smaller than one.

In figure 4.7 the same data is presented, but this time the localization error in dependency of the photon numbers. The upper density plots show the error distribution of the data and the theory in dependency of the photon number per event. Again the red area represents a high density of detected single molecule events, whereas less events are represented in the bluish marked areas. The lower plot shows the

Table 4.6: The values extracted from the data analysis of Alexa 680 are shown in this table. The correlated distributions are shown in figure 4.5.

Event-Analysis Alexa 680	
$\overline{N}$/Event	3871 ± 3505
$\sigma(PSF)$ [nm]	119
$\overline{\Delta x_{Th}}$ [nm]	11 ± 5
$\overline{\Delta x_{Fit}}$ [nm]	15 ± 6
$\overline{N}_b$/Pixel	641

regression lines fitted to the error distributions based on the same fit used in figure 4.6. The higher the photon numbers the smaller the error in localization - as expected - can also be retrieved from the negative gradient of the regression lines. The lines have nearly the same gradient and only differ slightly in the absolute value for the localization error.

Generally the predicted localization error is lower than the estimated fit error. One reason can be considered to explain this discrepancy: The fitting procedure does not take into account the correct photoelectron numbers. The factor 2.4 due to the preamplifier setting of 1 is not considered in the conversion from counts into photoelectrons. Therefore the fit algorithm is running with a lower photon number than actually correct, which could be the reason for slightly higher localization errors. The effect of this missing factor on the localization precision is not evaluated yet - a change in the fitting algorithm may be considered in future. It should be a small correction and will effect the estimated error to be larger.

Furthermore it should be considered that the derivation of the theoretical equation for the localization accuracy is based on various assumptions, which have been done beforehand. Detailed explanations concerning the derivation of the formula can be found in [Thompson et al., 2002], where restrictions of applying the formula are discussed.

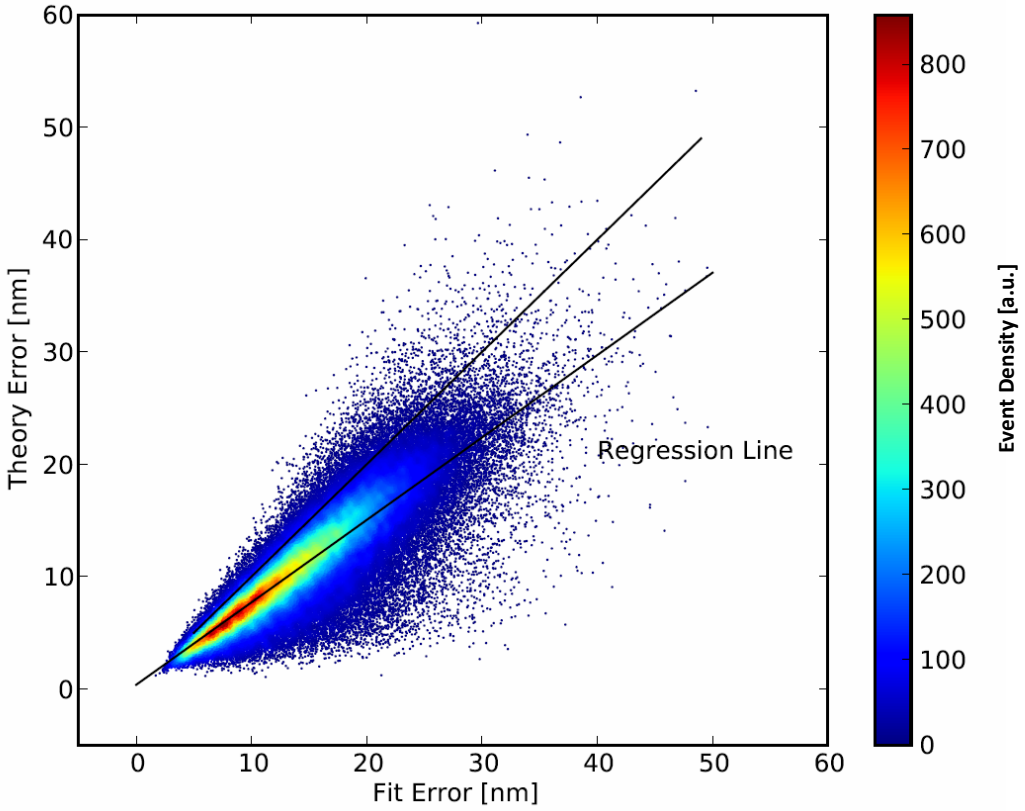

Figure 4.6: For better comparison the fit error is plotted against the error predicted by the theory. A regression line is fitted according to a linear least squares fit. The theoretical error is generally lower than the estimated fit error. Possible explanations for this result can be found in the text. Color represents the density of events, which occur with a certain error.

Correlation of Localization Error and Time

Surprisingly the localization error was observed to vary during the course of an acquisition. The time-dependence of the localization error is demonstrated in figure 4.8. The evaluation is based on the same data set analyzed in figure 4.5. Three periods of time are selected from the acquisition time and the corresponding error distributions are plotted against photon numbers per event. The red dots illustrates the error distribution at the beginning of the recording. It is obvious that higher photon numbers per event are dominant in the detection. This observation can be due to a good matching excitation cross-section and orientation of the bright fluorophores with the laser. Another possibility is that the very bright events are actually two events next to each other thus the detection is not able to separate

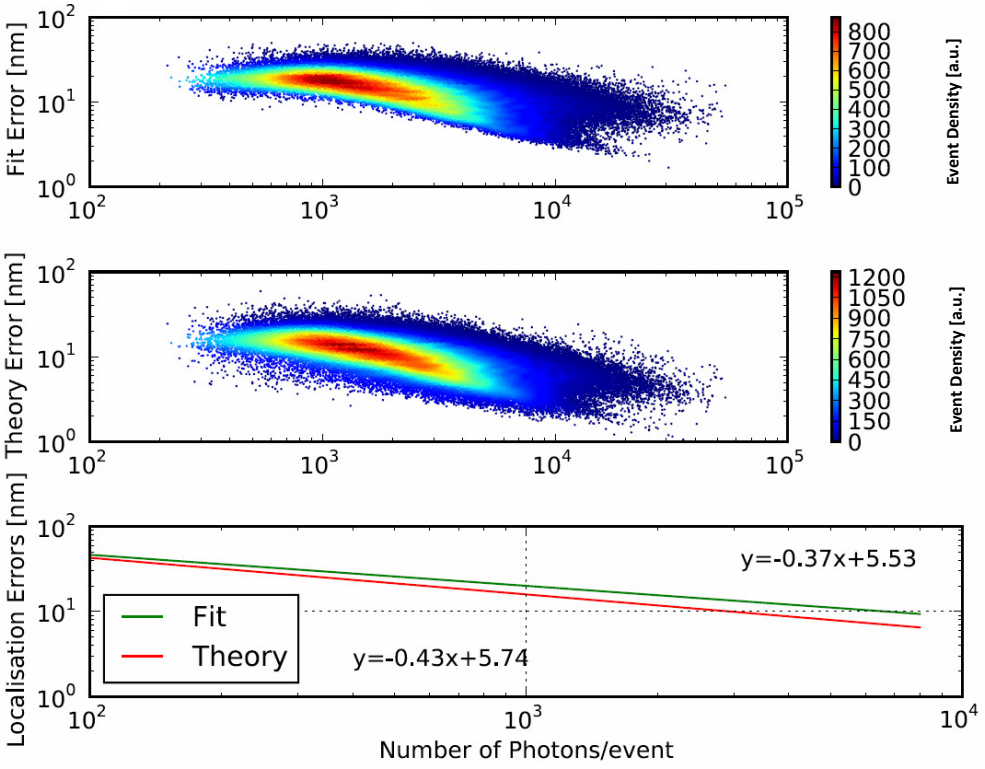

Figure 4.7: This diagram shows the fit and theoretical error distribution for the analyzed data set, but this time in dependency of photon numbers detected per event. A regression line is fitted to the data based on the same linear least squares fit as used before. A direct comparison is thereby given in the lower plot. The error in localization drops with higher photon numbers as expected. The theoretical error is in general lower as the estimated fit error, already evaluated previously in this section. Again, color is representing the density of events.

these. It is possible that events of lower intensity are drowned in the relatively high background at the beginning of the recording (background data not shown). The high background also influences the localization error negatively, which is obvious when taking the high photon numbers per event into account and still achieving a localization error $\backsim$ 15 nm. The arrows should visualize the tendency of fit error in correlation to photon numbers per event as well as with the proceeding time.
The green dots are events detected during the middle of the recording. The photon number per event clearly shifts to lower numbers. Out-of-focus fluorescence is mainly bleached at this stage, which leads to an improvement in the localization accuracy. Furthermore the density of weaker events detected increases distinctly. The very bright events are either already bleached in the these frames, which is possibly due

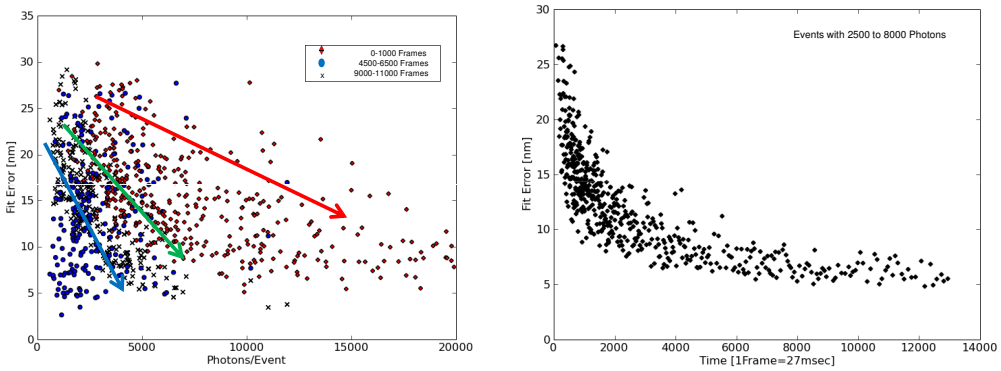

Figure 4.8: The left plot demonstrates the correlation of the fit error to photon numbers per event during the proceeding recording. Three different periods of time are selected from the recorded data. Photon numbers tend to smaller values as well as the fit error. The right shows the development of the fit error during the data acquisition for events consisting of 2500 to 8000 photons. This distribution also shows a better localization accuracy during later frames.

to the better cross-section with the excitation laser line or double detections are avoided, because of a decreasing number of molecules, which are in the bright state at the same time. The blue dots illustrate the events recorded at the end and their correlated fit errors. Here the same tendency as for the green dots is obvious. The fit error shift further to smaller values as well as the photon numbers.
Additionally the dependency of the fit error over time is shown. For this purpose only events consisting of 2500 to 8000 photons are selected. This corresponds to $\backsim$ 20 % of all detected events. This figure supports the statements made before. The localization error is higher at the beginning and drops at $\backsim$ 4000 frames under 10 nm. Agein high background fluorescence in the beginning of the recording seems to be the explanation for this phenomen, as photonnumbers are several thousands per event. Double detections of two single molecule events as one can also lead to higher localization errors though the photon number is high. For further analysis it can be suggested to 'through away' a few frames in the beginning in order to avoid false information. Though the main limiting factor for the localization accuracy will remain the background fluorescence.

Analysis of the Limiting Factors of High-Resolution

This section deals with the limiting factors for the localization precision. In the previous chapter figure 4.7 showed the estimated localization error distribution compared to the predicted error. The predicted error is consisting of two terms - the

noise in background and the noise in signal (2.16). To demonstrate, which term restricts the resolution mainly, the same data as in figure 4.7 is used in order to evaluate the predicted localization accuracy depending on only one limiting factor. This time the theoretical calculation only includes either the noise in signal term or the noise in background term in the formula (see formula 4.2 and 4.3). Figure

$$\langle(\Delta x)^2\rangle = \frac{(\sigma_{PSF})^2 + \frac{a^2}{12}}{N} \qquad (4.2) \qquad \langle(\Delta x)^2\rangle = \frac{8\pi(\sigma_{PSF})^4 b^2}{a^2 N^2} \qquad (4.3)$$

Figure 4.9: The theoretical localization error taking either only noise in signal or only noise in background as a limiting factor for resolution into account.

4.10 illustrates what the error distribution looks like taking only one localization limiting factor into account. The plots in the first row of each diagram show the error distributions evaluated in the fitting process. The second row shows the theoretical prediction for the error, but ones the formula only includes the noise in signal term (upper plot) and once only the noise in background term (lower plot). Moreover, a regression line is fitted to each distribution evaluated with a least squares fit ([Scipy, 2009]).

Table 4.7: The theoretical localization error is calculated by using formula 2.16. To extract the limiting factor for localization the same calculations are performed, this time only taking either noise in background or noise in signal into account (see equation 4.2 and 4.3)

	Δx [nm]	%	FWHM [nm]
Error Theory	11 ± 5	100	27
Only Noise in Signal	3 ± 1	∽5	8
Only Noise in Background	10 ± 5	∽95	25

Obviously the background is the predominant noise source, which mainly influences the resolution.
Without any background a theoretical resolution of ∽ 5 nm could be achieved, assuming a mean spot size of 120 nm (standard deviation) and a mean photoeletron number of 4000 per event (see table 4.6):

$$\Delta x = \frac{\sigma_{PSF}}{\sqrt{N}} = \frac{120nm}{\sqrt{4000}} \approx 1.9\,nm \qquad (4.4)$$

which leads to an estimated resolution of $FWHM = \Delta x \cdot 2.35 \approx 4.46\,nm$.

Therefore it is still desirable to reduce the background in order to achieve high resolution images, which are not background limited.

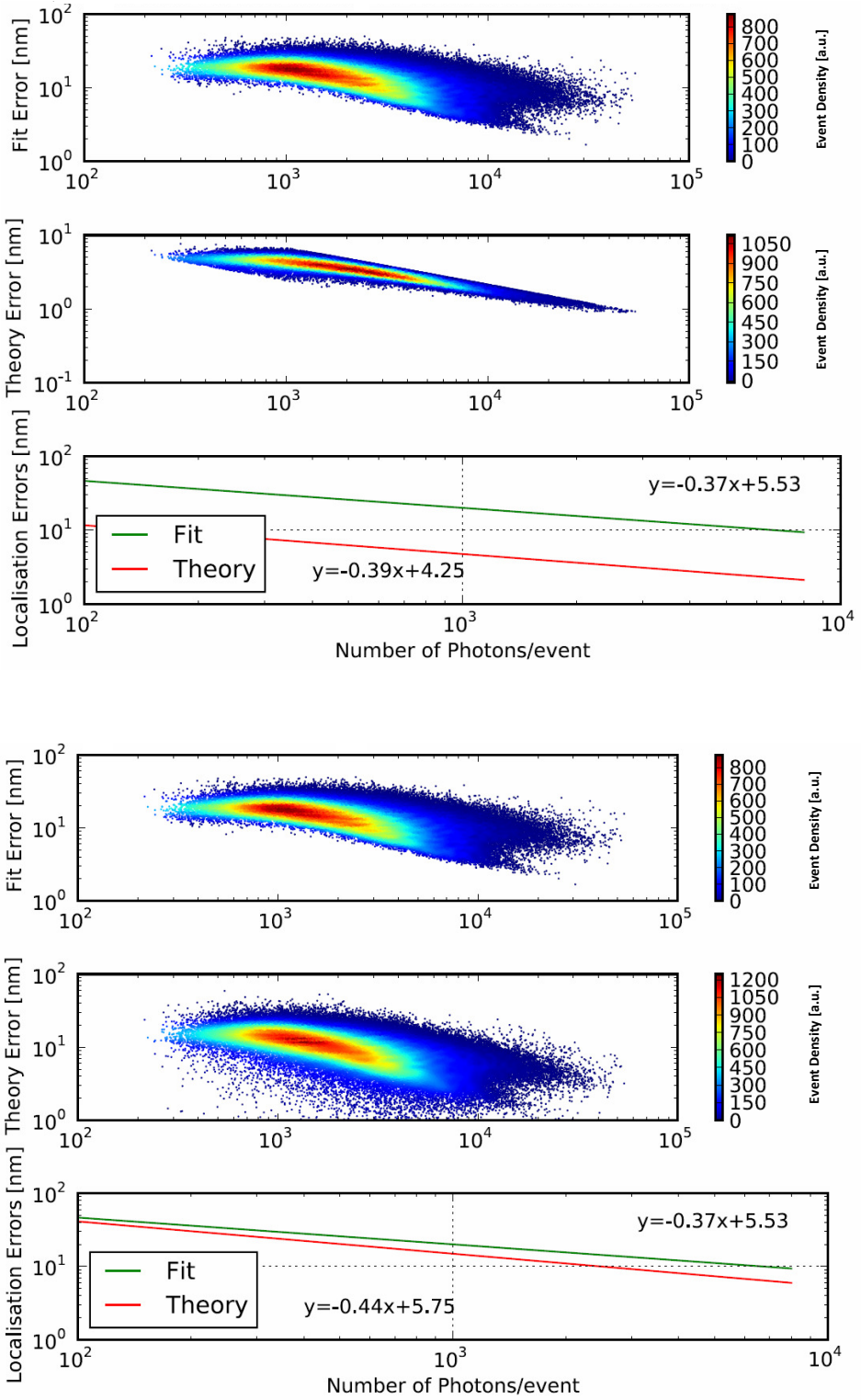

Figure 4.10: The two main noise sources are plotted independently. The upper plot shows the localization accuracy limited only by noise in the signal. The lower diagram illustrates a localization error only caused by background fluorescence. The third plot shows the regression lines fitted to the distributions above with a least squares function. It is obvious that the background noise is the main reason for a limited resolution. The event density is represented in the colorcode.

4.4 Comparison of the far-red Alexa Dyes

An overview of the far-red Alexa dyes is given in table 4.8. For these measurements new labeled cells and freshly mounted have been imaged to assure a good comparison. At this stage control measurements of the laser power with a power meter have been established, because it was recognized that the scale on the control component for the laser does not correctly translate into laser power. When the data, presented in this section, has been recorded a laser power of $\backsim$ 200 mW was established. The data presented in the previous sections might be recorded with less laser power.
Another change in the setup is needed to image the longer far-red dyes. A new blocking filter is chosen (XF3104,690ALP, Omega Optical), because the emission filter chosen in previous experiments (HQ710/50, Chroma Technology) - a bandpass - is not able to transmit the longer far-red dyes Alexa 700 and 750.

Table 4.8: The table shows a comparison between the tested Alexa dyes. The first row shows the expected localization accuracy predicted by the formula explained in the text. The following values are obtained by the fitting algorithm. Listed are the mean values calculated of the recorded data and the related standard deviations. All data is presented in [nm]. The variables N and N_b show the number of photoelectrons detected.

Fluorophore	Alexa 647	Alexa 680	Alexa 700	Alexa 750
$\overline{N}$/Event	4173 ± 3265	6343 ± 4725	6370 ± 4574	3037 ± 1734
$\sigma(PSF)$ [nm]	125	123	126	133
$\overline{\Delta x_{Th}}$ [nm]	13 ± 5	11 ± 5	11 ± 5	15 ± 5
$\overline{\Delta x_{Fit}}$ [nm]	16 ± 6	14 ± 6	15 ± 7	19 ± 6
$\overline{N}_b$/Pixel	1028	1111	1255	688

The theoretical calculation for the localization error - listed in the first line - includes em-gain noise, read-out noise and a preamplifier factor for the conversion of counts into photoelectrons. The fit is not taking the preamplifier factor into account as mentioned in previous chapters. The mean photoelectron number per detected single molecule event for Alexa 680 is 39 % higher than in section 4.3. This can be explained by the variations in the laser intensity as explained above. Slighly lower laser intensities can already result in much lower photon numbers per event.
The photon numbers for Alexa 680 and 700 are nearly similar as expected, because

their peaks in the excitation spectrum differ only by 20 nm and therefore are both likely to be excited very well by the 671 nm laser line. Only $\backsim$ 50 % of photons per event are recorded for Alexa 647 and 750. Their cross-section of the excitation spectrum with the 671 nm laser line is less and therefore the results are according to expectations. But still the mean photon number per event is high enought to lead to a localization accuracy on the nanometer scale. The localization errors are again higher than the theoretical predicted error, which was discussed in the previous chapter. The fit error of Alexa 750 is slightly larger, which is due to the longer wavelength. The background values are higher compared to the measurement presented in the analysis in section 4.3. The cells labeled for this measurement probably had more unspecific labeling or more unbound secondary antibodies, which were diffusing during the measurement. The higher laser intensity used for this measurement could also be the reason. With a higher laser intensity automatically more fluorophores, which are out-of-focus fluorescence, can be excited. Only Alexa 750 shows background values similar to measurements in the previous analysis. But this also can be due to less efficient excitation with the 671 nm laser line.
σ of the PSF has remained quite stable. It increases slightly due to the longer wavelength, which leads to a broader intensity distribution. In general it is possible to achieve a resolution down to $\backsim$ 30 nm with the RPM method presented in this thesis under the described circumstances. This resolution is ideal to image protein distributions within cells.

Photon numbers per event published for Alexa 647 in the recent years show similar results. [Heilemann et al., 2008] and [Huang et al., 2008] both achieved photon numbers of several thousands per 'on-cycle' and are therefore in good agreement with the results presented in this work. The main improvement in this work is the shorter time-acquisition needed to achieve high photon numbers per event. In general 27 msec are enough to gain several thousand photons per event, whereas in [Heilemann et al., 2008] several frames (each 50 msec) are needed to achieve such a high number of transitions, even though the experiments were performed in the same oxygen depleted solution including a triplet state quencher as in the measurements performed in this thesis (see section 3.3). This is probably due to the low laser intensity of $\backsim$ 15 mW, which was applied in their experiments. In comparison RPM is demonstrated with much higher laser intensities ($\backsim$ 200 mW), which probably explains the shorter time to collect a similar amount of photons.

Cy 5.5, a dye assumed to have a similar structure as Alexa 647, has also been explored concerning its physical abilities in single molecule detection. This dye was reported to stay in a bright state for only a very short time ($\leq 2\,\text{msec}$), resulting in only a few hundred photons per single molecule event([Steinhauer et al., 2008], [Bock et al., 2007]). In [Steinhauer et al., 2008] all tests were performed in an oxygen depleted solutions including the supposed triplet quencher ascorbic acid (AA), whereas in [Bock et al., 2007] all experiments were done using the triplet state quencher β-mercaptoethylamine, but no oxygen scavenger. If it was somehow possible to extend the 'on-time' of the Cy 5.5 dye, the collected photon number would also result in a few thousands per detected event.
There are no studies regarding the other far-red Alexa dyes at present.

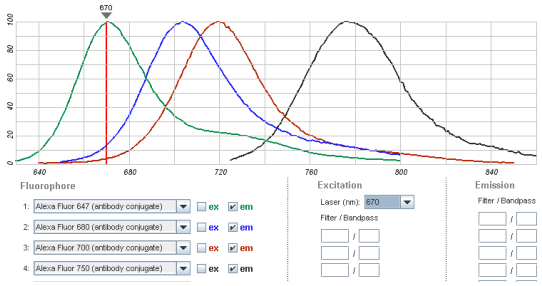

Figure 4.11: Emission spectra of the far-red dyes in the Invitrogen Database ([Invitrogen, 2008]). With suitable filters the spectra can be well separated in terms of two-color imaging or also three-color imaging (see section 4.5).

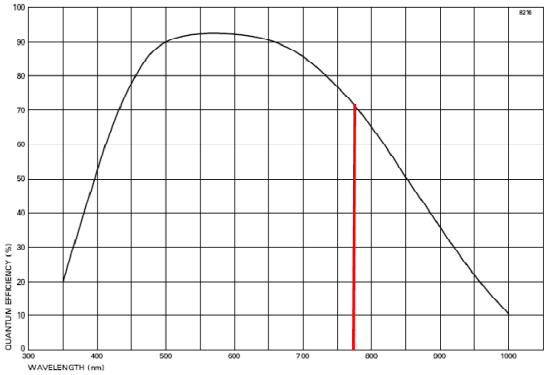

Figure 4.12: The typical quantum efficiency of the Andor IXon DV887DCS-BV electron multiplying charge-coupled device camera at a temperature of -20°C. The red marker shows the peak of the emission spectrum of Alexa 750 - the dye, which has the emission spectrum with the longest wavelengths of the here tested Alexa dyes. As the quantum efficiency is still more than 70 %, imaging of Alexa 750 is possible without a too great loss in photon numbers.

In terms of multicolor imaging the emission spectra of tested Alexa 647 and 700 dyes as well as Alexa 680 and 750 dyes can theoretically be well separated using a suitable dichroic and emission filter (see figure 4.11 and section 4.5). Moreover, the CCD-camera is still able to collect more than 75% of all photons emitted by Alexa 750, the dye with the longest wavelengths in the emission spectrum (see figure 4.12). This is more than enough for a sufficient single molecule detection.

4.5 Multi-Color Imaging

The main goal of this project is to perform imaging of two different protein distributions within cells, each labeled with a different color. For this purpose several changes in the microscope setup and in the analyzing software have to be conducted, which will be explained in this section. Images recorded with this extended setup will be presented and a few biological applications will be presented.

Changes in the Microscope Setup

To perform multi-color imaging it is intended to detect each color separately. As only one CCD-chip is available in the used microscope setup, the CCD-chip is split into two halves, in order to detect one color on each. Therefore a few changes on the microscope setup are conducted. The setup is extended with a 'splitter' constructed according to [Bossi et al., 2008] by Dr. David Baddeley (see figure 4.14 and 4.13). The purpose of the splitter is to separate two colors on the CCD-chip, which are mixed in the fluorescent light emitted by the sample. This is illustrated in figure 4.13, a detailed schematic of the beam path: Originally the CCD-chip was placed in the image plane. Now a slit, acting like a field stop, is positioned exactly where the CCD-chip was and crops the size of the beam, because the extension of the CCD-chip is reduced to half of its actual size as one half is used for each channel. Then one CCD-half consists of only 512 x 256 pixels instead of 512 x 512 pixels. After passing through the image plane the fluorescent light is re-collimated by a second lens and impinges on a second dichroic beamsplitter. This dichroic beamsplitter will split the fluorescent light, which contains two colors, into two separate beams. Finally additional optics (mirrors) direct the beams to the camera, where two lenses focus each beam on one CCD-half. A coarse alignment of the two CCD-halves on the computer screen can be performed using the optics (~ 300 nm) of the splitter. A later applied shift field, which will be explained in detail later in this section, takes care of the finer adjustments.

Multi-color imaging is performed with the far-red dyes presented earlier in this work. Therefore the 671 nm laser line is used for excitation as well as the appropriate dichroic beamsplitter used before in the microscope setup (Semrock, Q680LP). The emission filter also stays the same (XF3104-690ALP, Omega Optical). The sec-

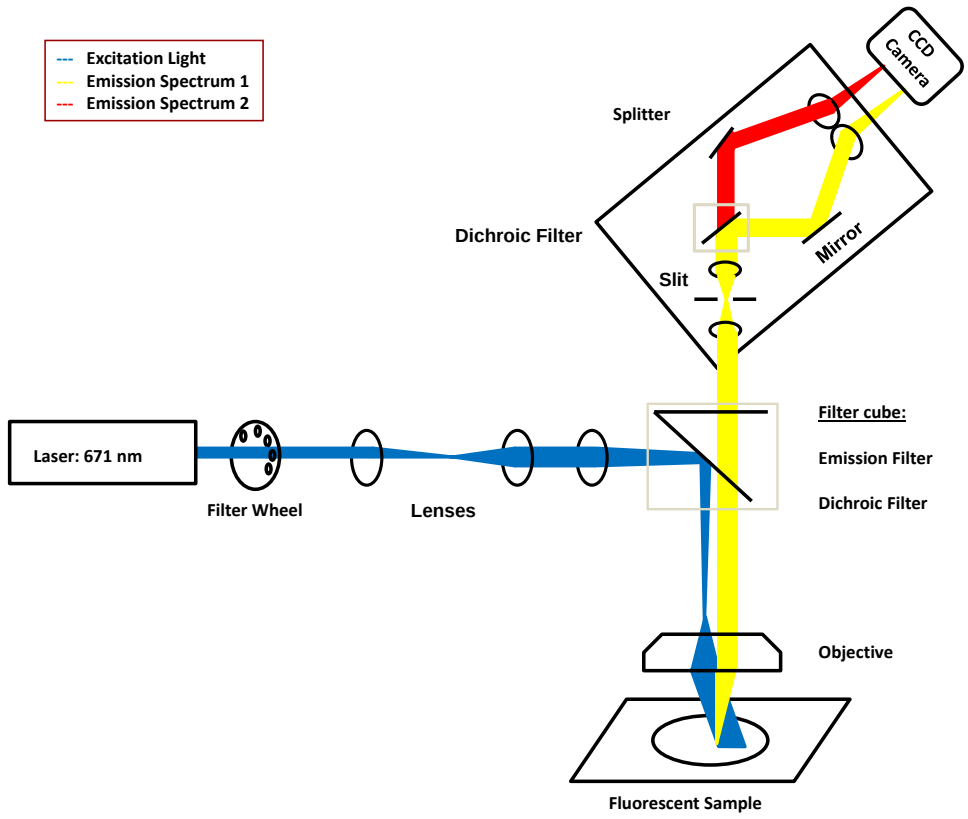

Figure 4.13: The schematic shows the beam path in the extended microscope setup to perform multi-color imaging. A slit is placed in the former position of the CCD-chip, which crops the beam to a size fitting half of the CCD-chip. A second dichroic filter splits the fluorescent light emitted by the sample into the different colors. Additional optics direct the two beams to the camera focused by an extra pair of lenses.

ond dichroic beamsplitter in the beam path is selected from a range of commercially available products by taking the fluorophore emission spectra into account.

Generally it is not possible to detect a single molecule event in only one channel. A dichroic beamsplitter is never able to reflect or transmit 100 % of the photons belonging to one wavelength and the stepness of a filter is never infinite. As one event consists of several thousand photons, a certain amount of those will be either reflected or transmitted. As a result the ratio of the transmitted and reflected fraction will include the information, which color the detected event belongs to.
The second plot in figure 4.15 shows the emission spectra of the far-red Alexa dyes measured with the spectrometer, after they passed through the first filter cube (Dichroic beamsplitter: Q680LP, Chroma Technology; Emission Filter: XF3104,690ALP,

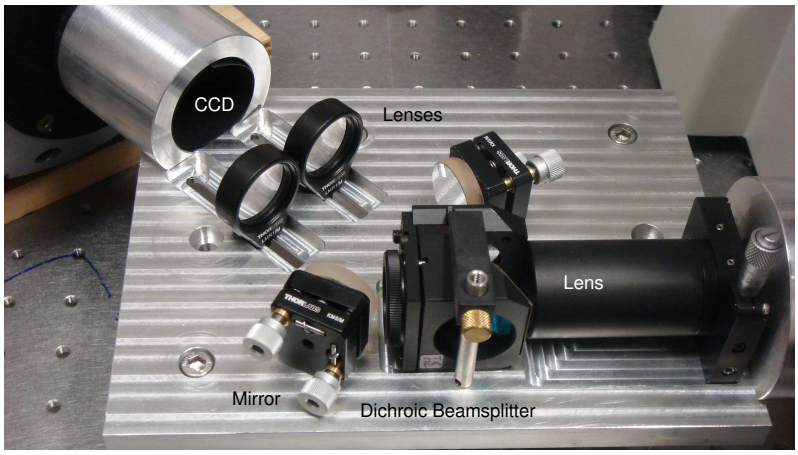

Figure 4.14: This construction is constructed by Dr. David Baddely based on the same principle published in [Bossi et al., 2008]. For further details see the schematic in figure 4.13. In practice the splitter is covered to avoid any external light sources reaching the CCD-chip.

Omega Optical). Based on these emission spectra a range of commercial available dichroic beamsplitter were tested according to the fractions of transmitted and reflected photons they would provide for each far-red Alexa dye. The ratios were compared in order to achieve the best separation for two and three colors.

At the end two dichroic beamsplitter were selected, based on the calculations of the ratios. For two color imaging a dichroic beamsplitter with a cut-off at 741 nm was selected (FF741-Di01, Semrock; see left plot in figure 4.15). Table 4.9 lists the evaluated ratios for all far-red Alexa dyes, which would be achieved using the FF741-Di01 dichroic beamsplitter. The first column presents the theoretical calculations based on the spectra given by the company, whereas the calculations in the second column are based on the actual measured spectra of the dichroic beamsplitter. Reflection and transmission are evaluated in percentage. Performing two color imaging Alexa 750 needs to be one of the dyes chosen for the double labeling, because 86.57 % of the photons will be detected in the transmitted channel. In comparison $\backsim$ 80 % of the photons emitted by the other dyes per event will be reflected and therefore detected in the other channel. Slight variations between the theoretical calculations and calculations based on the actual measured spectra appear, when comparing those. But this is no disadvantage in terms of two color imaging due to

the fact that Alexa 750 and one of the other dyes can be still separated very well.

For potential three color imaging a XF2083, 708DRLP (Omega Optics) dichroic beamsplitter was selected. The expected percentage of transmission and reflection are listed in table 4.10 as well as the measurements. Here a clear discrepancy can be seen. The theory would allow to separate three Alexa dyes 647, 700 and 750 quiet well. The actual measured spectrum of the dichroic beamsplitter shows a different separation of the dyes. This could lead to a potential overlap overlap of Alexa 647 and 700. This observation will be demonstrated in practice in the next section.

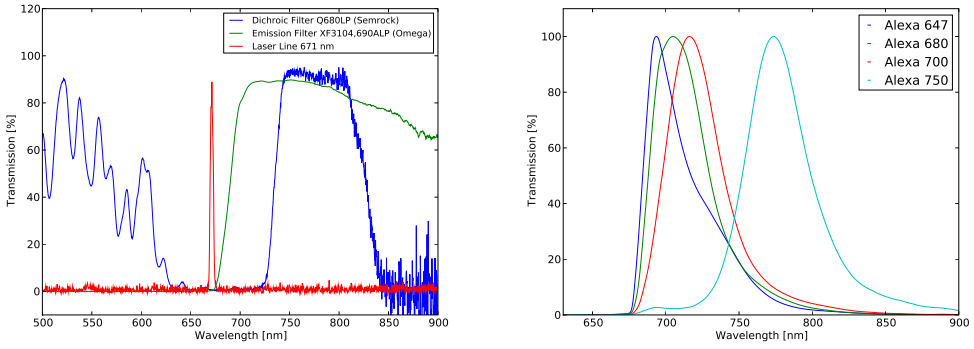

Figure 4.15: The left figure illustrates the actual reflection and transmission capabilities of the selected dichroic beamsplitter and emission filter. The laser line 671 is also measured. Emission spectra of the far-red dyes after the fluorescent light passed the dichroic beamsplitter(Q680LP, Semrock) and the emission filter (XF3104-690ALP, Omega Optics). The spectra were measured with a spectrometer and analyzed with the software 'Oceanoptics'.

Table 4.9: Two color imaging is performed with the FF741-Di01 dichroic filter (Semrock), chosen out of a range of commercial available filters. This table shows the expected percentage for reflection and transmission for each far-red Alexa dye (first column). In comparison the same calculations were performed using the actual measured spectrum of the selected dichroic beamsplitter. Variations can be found, but are not effecting the separation of two colors negatively.

	Dichroic Beamsplitter	Semrock FF741-Di01	
Dye	[%]	Theory	Measurement
Alexa 647	Transmission	16.53	22.6
	Reflection	83.47	77.4
Alexa 680	Transmission	17.02	20.82
	Reflection	82.98	79.18
Alexa 700	Transmission	22.21	28.52
	Reflection	77.79	71.48
Alexa 750	Transmission	86.57	77.36
	Reflection	13.43	22.64

Table 4.10: The dichroic beamsplitter presented in this table (XF2083-708DRLP, Omega Optics) can be used either for two or three color images. Theoretical calculations of transmission and reflection are compared to calculations based on the spectrum of the dichroic beamsplitter measured with the spectrometer. Slight variations are also found in this evaluation, which lead to problems in detecting three colors. Two color imaging is not negatively affected .

	Dichroic Filter	Omega Optics XF2083-708DRLP	
Dye	[%]	Theory	Measurement
Alexa 647	Transmission	52.76	47.99
	Reflection	47.33	52.01
Alexa 680	Transmission	54.69	50.43
	Reflection	45.31	49.57
Alexa 700	Transmission	71.88	60.13
	Reflection	28.12	39.87
Alexa 750	Transmission	88.89	82.48
	Reflection	11.11	17.52

Changes in the Analysis Software and Shift Correction

The fitting process provided by the analysis software PYME stays nearly the same. As explained in the previous section the separation of the different colors is relying on the ratio of the photons detected in each channel. Before deciding whether an event has to be assigned to one color or another, the fractions of each single molecule event are evaluated independent from each other. First of all one CCD-half is flipped, which results in an overlay of both halves. Then two Gaussian distribution are fitted in both channels, which evaluates the coordinates of the center of intensity as follows:

$$f_G(\vec{x},\vec{y}|A_G,\sigma,x_0,y_0,b) = A_G \cdot e^{-\frac{(x-x_0)^2+(y-y_0)^2}{2\sigma^2}} + b_G \tag{4.5}$$

$$f_R(\vec{x},\vec{y}|A_R,\sigma,x_0,y_0,b) = A_R \cdot e^{-\frac{(x-x_0-\Delta x)^2+(y-y_0-\Delta y)^2}{2\sigma^2}} + b_R \tag{4.6}$$

The fittings in the reflected (green) channel and the transmitted (red) channel differ only in the exponent of the Gaussian distribution (additional Δx and Δy see formula 4.6) and each channel is associated with a different background level (b_G and b_R). Δx and Δy are the correction of the relative positions on the two CCD-halves. Due to differences in the beam paths and alignment issues of the CCD-halves a relative shift in x-y-direction is introduced. If this shift is not corrected events detected in one channel appear in a slightly different position in the other channel. The evaluation of the shift will result in a shift field, which is applied in the fitting process and corrects the relative positions on the two CCD-halves. This shift field is able to determine any position on one CCD-half relative to the other. Figure 4.16 shows

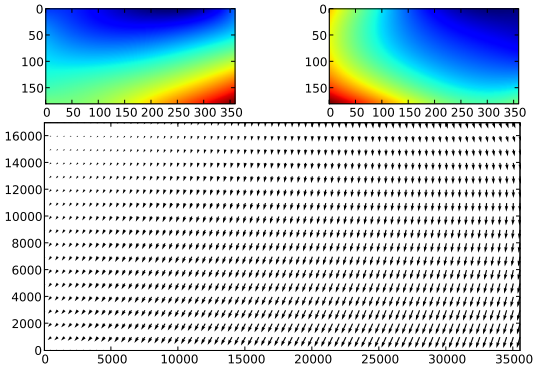

Figure 4.16: To match the positions on the two CCD halves a vector shift field is recorded which is able to translate one position on the CCD into the correlated position on the other CCD-half.

an example of a shift field. The colored diagrams reflect the absolute value of the x-shift on the right side and the y-shift on the left side. Red is translated into a greater shift, whereas blue represents small relative shifts. This is also reflected in the length of the arrows. To confirm that shift variations over time are not a possible problem in analyses, several vector fields were recorded over time. Changes are ranging in dimensions of the resolution. The mean shift values calculated for changes in the relative shift correction over time are listed in table 4.11. The mean change in x-direction is only 6 nm ± 4, whereas in y-direction a higher shift of 14 ± 6 shift is recorded.

Table 4.11: The mean values for changes in the x-y-shift occurring over time, are evaluated. The shift in y-direction is higher than in x, but still below the resolution limit.

$\overline{\Delta x}$ [nm]	6 ± 4
$\overline{\Delta y}$ [nm]	14 ± 6

After the fitting procedure each event has a position parameter and two intensity values A_G and A_R. Based on these two intensity values it can be decided whether the event belongs to one or the other color:

$$Ratio = \frac{A_G}{A_G + A_R} \tag{4.7}$$

The separation of two colors in practice is demonstrated in figure 4.17 and 4.5.
The first example is the separation of Alexa 680 and 750 shown in figure 4.17.RyR was labeled with Alexa 680 and Caveolin-3 with Alexa 750 in isolated cardiac myocytes. The x-axis is the reflected (green) channel on the CCD-chip and the y-axis is the transmitted (red) channel. The plotted data represent therefore the ratios of reflection versus transmission. A clear separation of the colors can be achieved. The blue cloud consists of all events, which are assigned to be Alexa 680. The red cloud represents all events assumed to be Alexa 750. The lines drawn through both distributions shows the expected fraction of photons, which are reflected by the dichroic beamsplitter (see table 4.9) evaluated by formula 4.7. It is clear that calculation and measurement are in good agreement and provide a good separation for the two Alexa dyes. The small plot shows all detected events depending on the

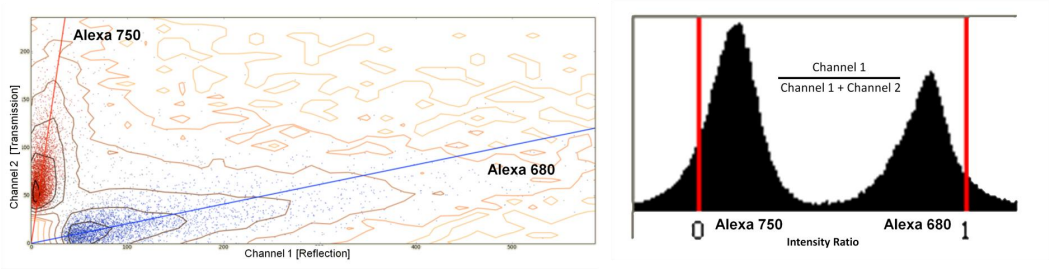

Figure 4.17: The upper left plot illustrates the color separation of Alexa 680 and 750 with the FF741-Di01 (Semrock) dichroic beamsplitter, which is based on the intensity ratios in both channels. The labeled structures were Ryr (Alexa 680) and Caveolin-3 (Alexa 750) in isolated cardiac myocytes. The x-axis represents the intensity detected in the reflection channel, whereas the y-axis is the intensity detected in the transmission channel. The ratios of reflection versus transmission are plotted. The lines show the expected ratios of reflected light for the two colors. These values are extracted from the theoretical calculation, which can be found in table 4.9. The upper right diagram show the intensity ratios - each bump representing one color. A clear separation of the two colors can be achieved with little spectral overlay.

ratio of transmitted and reflected photons. Events with small ratios present Alexa 750, whereas events with higher ratios are assigned to Alexa 680.

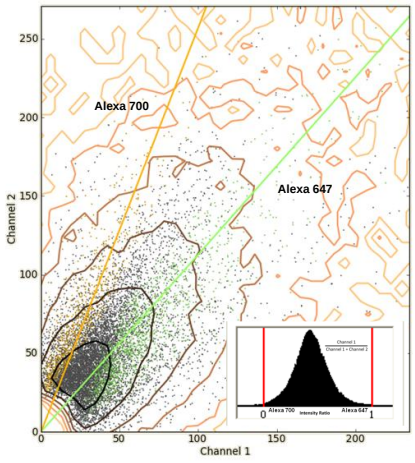

Figure 4.18: The 'separation' of Alexa 700 and 647 is demonstrated using the XF2083-708DRLP (Omega Optics). The structures labeled for this measurement were RyR (Alexa 700) and Caveolin-3 (Alexa 647) in isolated cardiac myocytes. The x-axis represents the intensity detected in the reflection channel, whereas the y-axis is the intensity detected in the transmission channel. The ratios of reflection versus transmission are plotted. The lines show the expected percentage of reflected light for the two colors based on the theoretical calculation presented in table 4.10. The other small diagram show the intensity ratios - only one bump is visible. Therefore its nearly impossible to separate the two colors, which is in controversy to the expectation.

The separation of Alexa 647 and 700 using the XF2083-708DRLP (Omega Optics) beamsplitter is demonstrated in figure 4.5. RyR was labeled with Alexa 700, whereas Caveolin-3 was labeled with Alexa 647. These two colors are supposed to be well separated with this dichroic beamsplitter. The measurement shows results, which disagree with the calculation. It is nearly impossible to distinguish the two distri-

butions. They appear as one color. The theoretical predicted ratios (see table 4.10) are plotted as a line, which differ from the actual data recorded. Therefore this dichroic beamsplitter will be useless in terms of three color imaging. But still two color imaging can be performed with this dichroic beamsplitter and it also indicates that three color imaging is possible, when using a suitable dichroic.

Comparison Single-Channel versus Two-Channel Detection

The two-channel detection varies slightly from the single-channel detection. Therefore further checks on the fitting procedure have been done. Again β-tubulin was labeled up with Alexa 680 in isolated cardiac myocytes, which provides the best 'blinking-abilities' of the far-red Alexa dyes with a single laser excitation at 671 nm. The recorded data set was analyzed once with the original single-channel fit, which produces after the analyzes two flipped images, and once with the two-channel fit algorithm. The mean values for photon numbers, localization accuracy and background compared. The dichroic beamsplitter used in the splitter for this measurement was the FF741-Di01 (Semrock), which should reflect 79.18 % as evaluated in table 4.9. of the photons and transmits only 20.82 %. The mean photon number detected in the single-channel fit is therefore reflecting only 80 % of the total number of detected photons (4.9). In table 4.12 contrast the single-channel detection and

Table 4.12: Alexa 680 was tested in a single channel and the two color channel microscope setup. The table shows the results of the two different fits. As only $\backsim$80 % of the photons are detected in the single-channel fit, the mean number of photons shown in this table includes also only 80 % of the total number. As a result the localization error is slightly higher in the single-channel fit.

	Single Channel	Two Channels
$\overline{N}$/Event	7387 ± 7319	8333 ± 7188
$\overline{\Delta x_{Fit}}$ [nm]	14 ± 7	12 ± 6
$\sigma(PSF)$ [nm]	129	132

the two color detection. The single-channel fit achieves a mean photon number of 7319 photons per event. Assuming that this number is only $\backsim$ 80 % of the total number, a recalculation leads to 9149 photons per event in the single-channel fit. This amount of photons per event is in good agreement with the two-channel fit,

which evaluates a mean photon number of 8333 per event. The slightly higher localization error in the single-channel fit is due to the lower number of photons detected in each event, because 20 % are lost in the other channel. Furthermore the spot size ($\sigma(PSF)$) and the estimated fit error (Δ x$_{Fit}$) lead to slighly variations in the absolute value, which are far below the resolution limit and therefore matching very well. This analyzis have proven a fitting algorithm that is able to achieve the same results as the already established single-channel fit. No deficiencies have appeared compared to the single-channel fit during the analyzis.

Chromatic Aberration

Another shift occurs due to chromatic aberration. Different layers are imaged as the focus for the different colors is in different depths. An overlay of two protein distributions imaged without correcting this, would not reflect the correct relative positions. Further corrections are therefore of need. A possibility of correcting this shift is a scan of the sample in z-direction during the recording. The result is an image consisting of different layers. In later processing of the data, a correction of the chromatic aberration can be applied. After evaluating the introduced chromatic shift, a layer of interest in one channel is corrected by this value and then overlaid with the corresponding layer in the second channel.
To evaluate the chromatic shift single antibodies of Alexa 680 and 750 were dried on a cover slip. Most of the antibodies are directly attached to the surface of the cover slip. While recording the focus was changed automatically by a step size of 200 nm. The result was a z-stack for each color consisting of ten steps. Most of the events for each color were recorded while the cover slip was in focus. Other layers in the z-stack consisted of lower event rates. The result was a histogram that shows two peaks at different z-position due to the chromatic shift (see figure 4.19). Shifting the z-stacks by $\backsim$300 nm leads to an appropriate correction of the chromatic shift. This procedure is also demonstrate in figure 4.19. The upper image shows an extract of a z-stack. The structure was β-tubulin labeled with Alexa 680 and 750 in isolated cardiac myocytes. Without a shift correction in the axial direction Alexa 680 shows the same structure as Alexa 750 only one image later in the stack. Therefore the stacks were shifted thus the images finally overlay. The resulting overlay is demonstrated below. The yellowish coloration supports that a good overlay of both colors can be achieved by correcting the z-shift as explained.

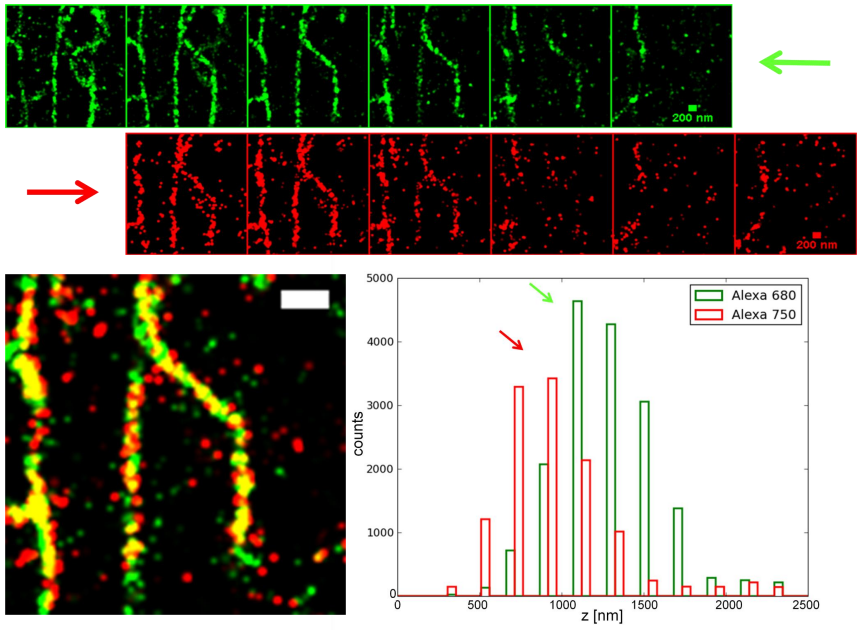

Figure 4.19: Chromatic shift correction: An axial chromatic shift of ∽300 nm was observed between Alexa 680 and 750. The shift was measured with single antibodies dried on a cover slip (see histogram). Most of the antibodies are directly attached to the cover slip and the peak therefore indicates the cover slip position. The difference in the peak location gives an estimate of the chromatic shift. z-stacks in 250 nm steps of β-tubulin, labeled with Alexa 680 and 750 , were recorded. A series of z-stack images is presented for each color (green: Alexa 680, red: Alexa 750). Shifting the stacks by one slice (∽ 250 nm) leads to an appropriate correction of the z-shift as is evident by the correspondence of structures. The lower image shows the final result after the correction where the yellowish coloration indicates a good overlay. Scale bar 200 nm.

At present state the correction is done in an offline analyses of the images in the image processing program ImageJ. In future an automated correction is considered in future.

Imaging and Results

To assure that both channels actually detect the correct structure, the same protein distribution was labeled with two dyes either in a competitive or tertiary labeling process. In the competitive labeling process both secondary antibodies with the different dyes attached can bind to the primary antibody, which marks the protein distribution of interest. In a tertiary labeling process the secondary antibody consists only of one color. The antibody marked with the dye of the other color is able to bind to the secondary.

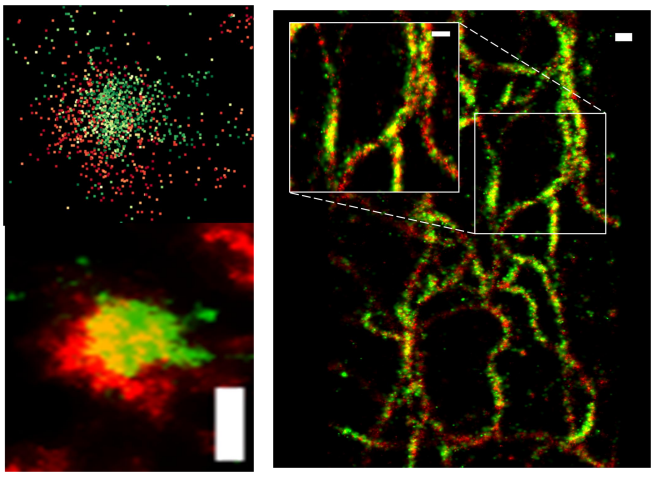

Figure 4.20: Left image: Ryanodine receptors (RyR) were competitively labeled with Alexa 680 and 750. One representative cluster is shown - the raw point data on the left, which clearly demonstrates an overlay of the single molecule events, and the visualized data on the right. A yellowish coloration can also be observed. Scale bar 200 nm. Right image: β-tubulin in isolated rat ventricular myocytes was labeled using an Alexa 680 secondary followed by an Alexa 750 tertiary antibody. Where the tertiary antibody has stained the sample it colocalizes with the Alexa 680 signal as expected (680: green; 750: red).

A tertiary and a competitive labeling is illustrated in figure 4.20. RyR's were competitive labeled with Alexa 680 (green) and 750 (red) in isolated rat ventricular myocytes. A representative cluster was selected (left image). The raw data points are shown on the top, which clearly demonstrate a good overlay of the single molecule events from each color. The bottom image shows the visualized data using Delauny's triangulation (see section 3.5). A yellowish coloration can be observed, though still a non-uniform coloration especially on the edges has to noted. A potential explanation for this differences in the labeling uniformity can be associated with antibody access, competition and specificity. The right image demonstrates a tertiary labeling of β-tubulin in isolated ventricular myocytes. Alexa 680 (green) was the secondary antibody, whereas Alexa 750 (red) functioned as the tertiary antibody. Where the tertiary antibody has stained the sample it colocalizes with the Alexa 680 signal as expected, which is illustrated by the yellowish coloration of the structure. Both images confirm that the two channels detect the same structure in the same position.

Supported are these observations by a colocalization analysis carried out by I. Dilshan (University of Auckland). A binary masc was created for the Alexa 680 labeling.

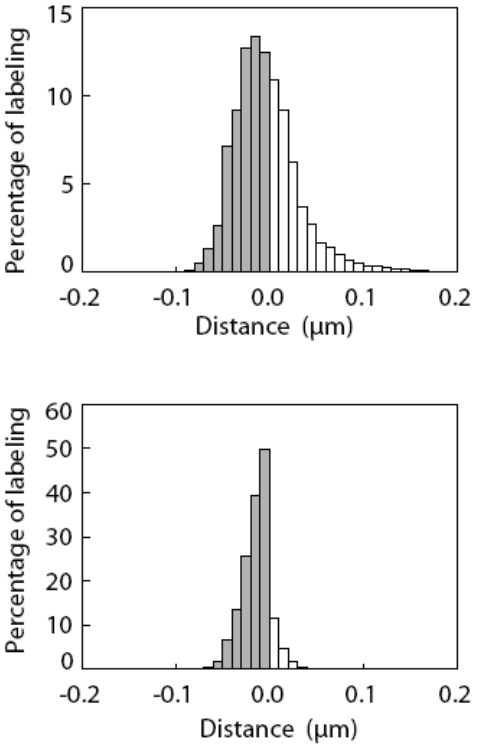

Figure 4.21: A colocalization analysis has been carried out for the data set presented in figure 4.20 in the left image. The upper plot shows the colocalization of Alexa 680. The gray colored area represents the percentage of Alexa 680 colocalized with Alexa 750. The calculation has shown an overlay of 59.5 %. The lower plot shows the colocalization of Alexa 750 with Alexa 680 (diagrams by I. Dilshan, University of Auckland), which leads to an overlay of 81.4 %. The difference in the overlay can be explained with the nature of the labeling process (see text). Negative values demonstrate an overlay of the two colors.

Based on the binary masc an euclidean distance map was created, which can was used to calculate the labeling as a function of distance. The value zero is related to the edge of the binary masc. Then the amount of Alexa 750 labeling within the masc and outside the masc can be evaluated (see also [Jayasinghe et al., 2009]). Negative distances represent labeling of Alexa 750 within the masc - it overlays with Alexa 680 - and positive distance values indicate no overlay. The same procedure was conducted for the colocalization of Alexa 750 with Alexa 680. This analysis was done for the data set presented in figure 4.20 for the right image, which shows β-tubulin labeled with Alexa 680 and 750 in a tertiary labeling process. The upper image illustrates the colocalization of Alexa 680 with Alexa 750. The gray coloration illustrates the percentage of overlay. 59.5 % correlation were evaluated. The lower plot shows the correlation of Alexa 750 with Alexa 680. Here an overlay of 81.4 % were calculated. The difference in the correlations is due to the labeling process. As Alexa 680 is the secondary antibody and Alexa 750 is the tertiary, more staining of Alexa 680 will be observed. This does not interfere with the purpose of this analysis. Where Alexa 750 has stained the sample over 80 % of Alexa 750 labeling colocalizes

with Alexa 680. This result supports that the two channel detection is analysing the data correctly and two color imaging of different stained samples can be conducted.

4.6 Biological Applications of Two-Color RPM

Finally biological applications of two color RPM have been conducted. Figure 4.22 shows the visualization of sodium-calcium-exchanger (NCX) in the surface membrane of isolated cardiac myocytes. NCX was competitive labeled with Alexa 680 (green) and 750 (red). A z-stack of 300 nm steps was recorded. The visualization

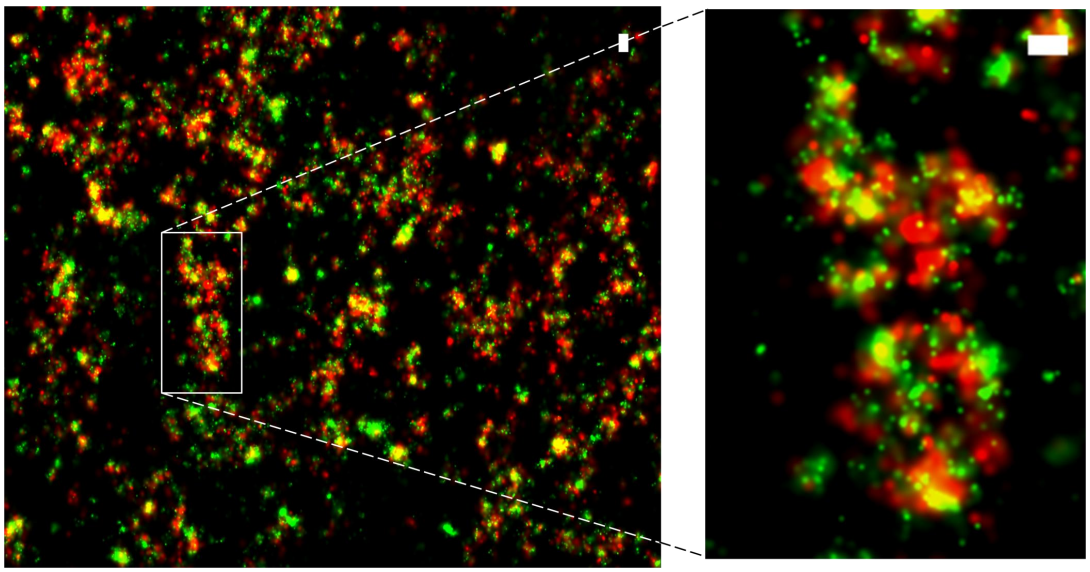

Figure 4.22: Visualization of sodium-calcium-exchanger (NCX) in the surface membrane of isolated rat cardiac myocytes competitively labeled with Alexa 680 (green) and 750 (red). Axial chromatic shift was corrected by recording a z-stack and performing an offline overlay of the corresponding layers. The magnification illustrates that both channels localize to the same structure, although significant small scale differences are observed, potentially a result of the competitive labeling process. The scalebar represents 200 nm.

was conducted by using a Gaussian rendering as explained in section 3.5. The axial chromatic shift was corrected in an offline analysis of the data in the image processing program ImageJ by aligning the corresponding layers. The magnification illustrates that both channels localize the same structure, although significant small scale differences can be observed. As explained in the previous section this observation in the labeling non-uniformity can be associated with antibody access, competition and specificity. But this example still demonstrates the usefulness of

using the far-red dyes in two color localization microscopy.

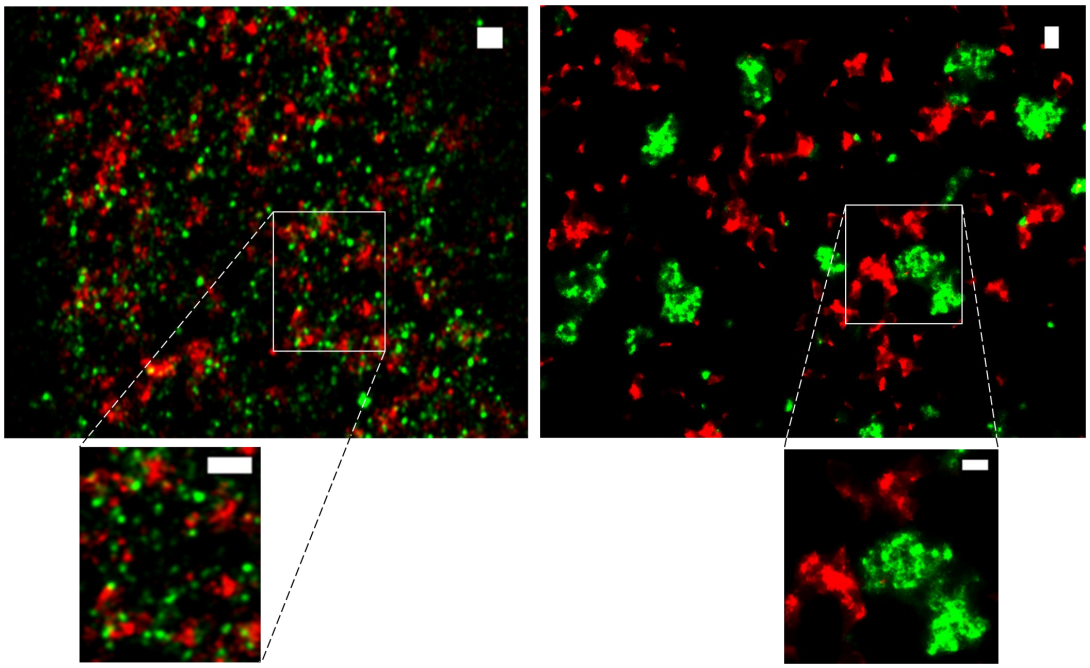

Figure 4.23: Two applications for multi color imaging are demonstrated: The left image shows the relative distribution of Caveolin-3 (green, labeled with Alexa 750) and NCX (red, labeled with Alexa 680) within an isolated rat cardiac myocyte. The right image shows the relative distribution of Caveolin-3 (red, Alexa 750) and RyR (green, Alexa 680). No obvious colocalization was observed. Scale bars 200 nm.

Actual two color images of different structures are presented in figure 4.23. The left image shows the relative distribution of the proteins NCX labeled with Alexa 680 (green) and Caveolin-3 labeled with Alexa 750 (red) with in isolated rat cardiac myocytes. The right image shows the proteins Ryr labeled with Alexa 680 (green) and Caveolin-3 labeled with Alexa 750 (red). In both images an obvious colocalization of the proteins could not be observed (see magnifications). To evaluate this observation further analyses need to be conducted.

Chapter 5

Discussion

After a brief analysis of the noise sources introduced in the detection process and their potential influence on the localization precision a detailed analysis of several commercially available Alexa dyes was conducted. As a result of this analysis the far-red Alexa dyes (647, 680, 700, 750) were chosen to perform all further experiments. Several advantages for single molecule detection were provided by using the far-red dyes. The autofluorescent background is substantially reduced by using a 671 nm laser line for excitation. Thus the yellowish autofluorescent background, suspected to be caused by the cell fixation, is highly reduced, which automatically translates into better localization precisions and also leads to a better detectability of week events. Moreover the 'blinking-behavior' is similar for all far-red dyes and they can be used with relatively consistent switching chemistry. Therefore all far-red dyes can be used in the same standard mounting medium, which was established for all experiments presented in this thesis. All other tested dyes were more difficult to detect with the acquisition settings used in this analysis. Another advantage of the far-red dyes are the high number of photons captured per 'blinking-event'. Several thousand photons per event have been detected for all far-red dyes. Alexa 680 and 700 provided the highest photon numbers due to the better excitation match with the 671 nm laser line. But Alexa 647 and 750 still provide high photonnumbers, which is still a good improvement compared to results published lately.
Improving the effective number of photons per 'blinking-event' and reducing the background leads to much higher localization accuracies. A comparison with the literature has shown a good agreement of the estimated fit error. A fit error of $\backsim$ 15 nm has been evaluated for all far-red dyes, though the error for Alexa 750

is slightly larger due to the longer wavelength. Localization errors predicted by a theoretical approach generally underestimated the fit error, which is due to various assumptions in the derivation of the theoretical approach. But theory and fit algorithm still agree with each other, which shows that the algorithm is working in an appropriate way and achieves good results in high resolution microscopy.
Surprisingly the analysis of the localization precision have shown a time-dependency of the estimated localization error during the course of an acquisition. Higher localization errors occur at the beginning of the recording as well as higher photon numbers per event. Higher photon numbers have been explained on one hand with a better matching excitation and on the other hand it was suggested that two event could be in a bright state at the same time within the diffraction limited area, which are detected as one event. Additionally higher background fluorescence was measured, which introduces a higher selection threshold and therefore weaker events are not detected. Though the photon numbers per event are higher in the beginning of the recording, a higher background fluorescence level and the possible detection of two events as one lead to less localization accuracy. Analysis at a later state of the recording have shown less background and smaller photon numbers per event, but also smaller estimated localization errors. This results supports the statement found in previous analysis of this thesis, that the background remains as the limiting factor for high resolution.

The analysis of the far-red dyes was conducted in order to use those for multi color imaging. The necessary changes in the analysis software and the microscope setup have been explained. To perform multi color imaging by using the far-red dyes a suitable dichroic beamsplitter needed to be selected, which is able to split the different colors emitted by the fluorescent sample. For two color imaging a dichroic beamsplitter from Semrock (FF741-Di01) was chosen, which is able to separate Alexa 680 and 750. The expected intensity ratios in each detection channel, which were the basis for the color separation, were in very good agreement with the theoretically expected ratios. Very good separation of these two colors have been demonstrated with the protein distributions of RyR, NCX and β-tubulin in isolated cardiac myocytes labeled either competitive or tertiary with the two dyes. The results of the detection in two channels were quite accurate and a localization accuracy of $\backsim$ 15 nm was achieved in this two color imaging method. Moreover the fitting algorithm for two channels was compared with the results evaluated by the

single channel fit in terms of photon numbers per event and localization accuracies. A good agreement could be demonstrated.

Besides the already mentioned advantages of the far-red dyes for use in localization microscopy additional improvements in order to perform multi color imaging have to be accentuated. Firstly, their emission spectra can be well separated and the CCD-camera is detecting well in the far-red range. Secondly, single laser excitation abolishes the need of aligning two different laser spots and it is possible to excite all far-red dyes with a common laser line (671 nm). And finally, simultaneous recording of two or more colors assures that no bleaching of the other color is performed and potential drifts during the recording are the same for all colors, which can be corrected during later analysis. The result of the analyses dealing with the chromatic shift have shown a shift in z-direction of 300 nm for the Alexa dyes 680 compared with 750. This shift can be corrected by recording z-stacks ideally with a step size of 300 nm, which allows overlaying the appropriate layers in a following offline analysis. Different integration times for each dye are not possible with this method, but as the far-red dyes provide similar characteristics, this possibility was not required. Differences in the labeling uniformity as observed in various images, where the same structures were labeled with two different colors, could be explained with differences in the antibody access into the cell, competition between the two colors and variations in the specificity of the antibodies. This observation may be a potentially limiting factor for super-resolution colocalization studies using immuno-labeling.

Three color imaging is in principle possible. For this purpose a second dichroic beamsplitter was selected based on the theoretical data from Omega Optics (XF2083-708DRLP) and tested. As presented in this work the actual transmission spectrum of the dichroic beamsplitter varies from the design spectrum. Different fractions of transmitted and reflected photons per event are detected, which results in a great overlap of the Alexa 647 and 700 dyes. It was impossible to separate these two colors and therefore three color imaging with the Alexa 647, 700 and 750 with this dichroic beamsplitter was not practical. But in principle it is still possible to perform three color imaging in future using an appropriate dichroic beamsplitter or by using another dye (e.g. Atto 725) with the current beamsplitter.

Applications of two color imaging using Alexa 680 and 750 have been presented. The relative distribution of NCX and Caveolin-3 has been demonstrated as well as the distribution of RyR and Caveolin-3 in isolated cardiac myocytes. Both images have been corrected for chromatic aberrations. The two colors can be clearly dis-

tinguished without much loss of events during the process of assigning one event to one color. Colocalization between the proteins have hardly been observed. In summery: Due to the advantages explained above two color reversible photobleaching microscopy using the far-red dyes can be a useful tool for future analyses of relative protein distributions within cells, which has a great potential to be extended for three color imaging.

Chapter 6

Conclusion

The aim of this thesis was to extend the developed reversible photobleaching microscopy method in various aspects in order to perform robust two color imaging. For this purpose a range of commercially available Alexa dyes have been tested and the far-red dyes have been identified to provide the best characteristics for high resolution imaging with the RPM-technique. They proved to be superior to the other dyes in terms of photon numbers, background and a relatively consistent switching chemistry. Background fluorescence is highly reduced as the emission spectra do not coincide with the autofluorescence spectrum caused by the fixation of the cells. The single laser excitation simplifies the application in terms of avoiding the bleaching of the second color while recording the first. Additionally a faster bleaching of one color compared to the other does not occur when using two far-red dyes excited by the same laser line and intensity. Axial chromatic aberrations can be corrected by a scanning process during the recording, which allows the appropriate layers to be overlaid. As a result different protein distributions within a cell and their localization with respect to each other can be studied. Despite the longer wavelength, the resolution we achieved (approx. 30nm), compares well with that obtained for dyes such as Alexa 488 or GFP.

The characteristics of the CCD-chip have been evaluated in order to understand the effects on the localization precision. The fitting algorithm implemented in the analysis process, was crosschecked with theoretically expected localization accuracies. It has been shown that the way of analyzing the data is in good agreement with the theory and leads to good high-resolution images.

A number of localization microscopy applications have been demonstrated. Partic-

ularly those applications dealing with specimens such as tissue samples or acutely isolated cells, which exhibit much higher autofluorescence and are thus more challenging than simple cell cultures or ultra-thin sections, will benefit from the use of dyes in the far red. Moreover, two color RPM has the potential to be extended for three color imaging and it will be in principle possible to record multi color images in 3D.

Protocols:

Cell Isolation:
developed by Dr.Nelly Kitaeff

Preparation:

1. Prepare the perfusion solution: 1 l of Ca-free Tyrode solution (TS)
    - 140 mM NaCl
    - 10 mM Hepes
    - 10 mM Glucose
    - 4 mM KCl
    - 1 mM $MgCl_2$ $6H_2O$
    - pH adjust with NaOH = 7.4 at room temperature
2. Prepare the perfusion apparatus - a modified Langendorf perfusion system:
    - switch on - oxygen
    - switch on - water bath 37°C
    - wash out then run 50-100ml of perfusion solution through the system4 mM KCl
    - add 50 ml of perfusion Ca-free TS to one reservoir
    - add 50 ml of TS with 100-200 μM Ca and enzymes to another reservoir:
        - 1.0 mg/ml Collagenase (Type2; Worthington Biochemical Corporation; Lakewood, NJ)
        - 0.1 mg/ml Protease (Type XXIV; Sigma-Aldrich; St. Louis, MO)

- eliminate air bubbles
- allow time to achieve correct temperature 37°C, check temperature

Heart cannulation and cell isolation:

1. ip inject ∽0.7 ml of anesthetic (0.15 ml of 300 mg/ml sodium pentobarbital in 0.55 ml Ca-free TS to give 140 mg/ml solution) to rat (200-300 g). Pinch the toe to ensure that the rat is fully anesthetized (∽2 min)

2. using scissors, enter into peritoneal cavity and cut upwards to neck, moving past diaphragm and ensuring no cutting of the heart. Quickly remove heart (pick the heart up between the index finger and thumb and cut the aorta below, about 2 mm from its entry into the heart) and immediately place in a weigh boat containing Ca-free TS at room temperature and wash briefly from the blood

3. mount the heart on the Langerdorff apparatus through the aorta using two pairs of forceps, clip and silk thread

4. perfuse the heart with 50 ml of oxygenated Ca-free solution approximately for 7 min to flush blood from the vasculature and remove extracellular calcium to stop contraction. Monitor the heart appearance: it should start looking pale and enlarged in size

5. switch Ca-free perfusion solution to the enzyme solution and perfuse for 10-15 min (digestion times can vary from heart to heart). Recycle the enzyme perfusate around 3 times until the heart looks glassy and the dripping becomes faster

6. cut ventricles from the hanging heart and place in culture dish with 150 μM Ca TS

7. chop (tear/mince/cut) gently into small pieces with fine scissors and slowly triturate/disperse the tissue, dissociate the heart tissue gently by wide-bore plastic transfer pipette

8. check the morphology and viability of the isolated cells: use for the experiment the rod-shaped cells with square edges and clear striation pattern

9. adding Ca back to 1.0 mM: let cell settle for 3-5 minutes

Cell Fixation:
developed by Isuru Dilshan

Solutions and Reagents:

- Phosphate-buffered Saline (PBS) (GIBCO, Invitrogen Corporation, Salbo10)
- PFA powder (GPR, Prod 294474L)
- 10 mM NaOH
- 10 % HCl

Fixation:

1. Making fixative 10 % PFA:
    - weigh 4 g of PFA powder into Petri dish under fume hood
    - heat 20 ml of fresh PBS to 60°C in a beaker while stirring
    - turn off the hot plate and let the temperature drop past 60°C
    - add 4 g of PFA powder (also weighed under the fume hood) when thermometer reading is $\backsim$ 58°-55°C and stir until all powder goes into solution
    - add 1-2 drops of 10M NaOH while stirring until the milky solution turns transparent while maintaining temperature $\backsim$ 45°C (solution typically goes clear in less than a minute)
    - once fully dissolved, add another 20 ml of fresh PBS and filter through filter paper into a bottle cooled in ice
    - adjust pH to 7.4 using (10 % HCl)
2. Before fixing isolated myocytes, dilute the above fixative 1:5 in PBS (to achieve a final concentration of 2 % PFA
3. Cells isolated into Tyrode's solution containing 200 μM Ca^{2+} should be gently spun down at $<$ 700 rpm for 2 min at room temperature in the 50 ml tube centrifuge and supernatant discarded without losing the cells

4. Immediately re-suspend the cells in 2 % PFA (use a volume like 20 ml per tube of cells); gently invert a few times if the cells have formed a pellet

5. Stand the tubes in room temperature for 10 min and then spin down for 2 min at 1200 rpm

6. Discard the supernatant containing the fixative and re-suspend the fixed cells in fresh PBS (to wash of any residual fixative); stand the tubes in room temperature for 10 more minutes

7. The cells may then be spun down again at 1200 rpm for 2 minutes and re-suspended in $\backsim$ 3-5 ml of the storage buffer (0.2 g BSA, 400 μl of 10 % NaN_3, 40 ml PBS; to avoid bacteria development)

Labeling:
developed by Isuru Dilshan

Solutions and Reagents:

- PBS (GIBCO, Invitrogen Corporation, Salbo10)
- Triton X-100 (Sigma Aldrich)
- Normal Goat Serum (NGS)
- Anti Ryanodine Receptor antibody (mouse pAb, Affinity BioReagents, IL, MA3-916)
- Anti Caveolin-3 antibody (rabbit pAb,ab2912-100, lot.490715, abcam)
- Alexa Fluor® 680 goat anti-mouse IgG (H+L) (*highly cross-adsorbed*, Molecular Probes, Invitrogen NZ)
- Alexa Fluor® 750 goat anti-rabbit IgG (H+L) (Molecular Probes, Invitrogen NZ)
- ProLong® Gold antifade reagent - Molecular Probes cat# P36930
- Incubation solution (PBS + 0.05 % Na Azide + 2 % Bovine Serum Albumin + 2 % NGS + 0.05 % Triton X-100)

1. Removal of storage solution:
    - obtain aliquots of unlabeled cells in BSA-containing storage solution into 500 μl tubes
    - spin down at 3000 rpm for 4 min and discard the storage buffer
2. Permeabilizing Cells:
    - add 250 μl of permeabilization solution (final concentration (final concentration 0.1 %) into tube and resuspend the pellet of cells gently by inverting the tubes a few times
      Permeabilization solution: (5 μl 10 % Triton-X100 in 495 μl PBS)
    - stand for 10 min at room temperature
    - spin down and remove supernatant
3. Blocking:
    - add Blocking buffer (final concentrations: PBS + 0.05 % Triton X-100 + 10 % NGS)
      Blocking solution: (5 μl Triton X-100 + 100 μl NGS in 900 μl PBS)
    - leave for one hour at room temperature
    - spin down and remove supernatant
4. Labeling with primary antibody:
    - remove liquid by spinning down
    - add 4 μl of RyR antibody (already diluted 1:1 in glycerol) to an effective dilution of 1:100
    - add 1 μl of Cav-3 antibody (already diluted 1:1 in glycerol) to an effective dilution of 1:500
    - re-suspend the pellets of cells and incubate the tube at 4°C overnight
5. Washing:
    - add 200 μl of incubation buffer into tube
    - add $\backsim$ 500 μl PBS and re-suspend the cells

- leave for 20-30 min at room temperature
- repeat washing steps two more times (i.e. three washes in total)

6. Labeling with secondary antibody:
    - add 200 μl incubation solution containing 1:100-diluted goat anti-rabbit Alexa 750 antibody and goat anti-mouse Alexa 680 antibody (4 μl of antibody per 200 μl)
    - re-suspend the cells and incubate at room temperature for 2 hour
7. Washing:
    - wash as in step 5

Switching Buffer:

1. Tube:
    - 1 ml PBS (GIBCO, Invitrogen Corporation, Salbo10)
    - 0.8 mg Catalase (from bovine liver, Sigma-Aldrich, C40)
    - 10 mg Glucose Oxidase (type III from Aspergillus niger, Sigma-Aldrich, G2133)
2. Tube:
    - 1 ml PBS (GIBCO, Invitrogen Corporation, Salbo10)
    - 0.2 g Glucose (99.5 % GC, Sigma-Aldrich, G7528)
    - 77.2 mg MEA (Cysteamine, $\backsim$ 95 %,Sigma-Aldrich, M9768-5G)

Mix ingredients 1:1 immediately before use $\rightarrow$ 500 mM Switching Buffer
Cleaning Solution:

- sodium hydroxide pellets (NaOH, AnalaR®, Prod 102525P, 40 g/mol)
- methanol (CH_3OH, Scharlan, ME03162500, 0.79 g/cm^3)

Bibliography

[Abbe, 1873] Abbe, E. (1873). Beiträge zur theorie des mikroskops und der mikroskopischen wahrnehmung. *Archiv für mikroskopische Anatomie*, 9:413–420.

[Alberts et al., 2008] Alberts, B., Johnson, A., Lewis, J., Raff, M., Roberts, K., and Walter, P. (2008). *Molecular Biology of the Cell*.

[AndorTechnology, 2005] AndorTechnology (2005). Andortechnology ccd camera.

[Baddeley et al., 2009a] Baddeley, D., Cannell, M. B., and Soeller, C. (2009a). Visualisation of localisation microscopy data.

[Baddeley et al., 2009b] Baddeley, D., Jayasinghe, I. D., Cremer, C., Cannell, M. B., and Soeller, C. (2009b). Light-induced dark states of organic fluochromes enable 30nm resolution imaging in standart media. *Biophysical Journal: Biophysical Letters*, 96:L22–L24.

[Baddeley et al., 2009c] Baddeley, D., Jayasinghe, I. D., Lam, L., Rossberger, S., Cannell, M. B., and Soeller, C. (2009c). Optical single channel resolution imaging of the ryanodine receptor distribution in rat cardiac myocytes. *Biological Science: Biophysics and Computational Biology*.

[Bates et al., 2008] Bates, M., Huang, B., and Zhuang, X. (2008). Super-resolution microscopy by nanoscale localization of photo-switchable fluorescent probes. *Current Opinion in Chemical Biology*, 12:505–514.

[Bers, 2002] Bers, D. M. (2002). Cardiac excitation-contraction coupling. *Nature*, 415:198–205.

[Betzig et al., 2006] Betzig, E., Patterson, G. H., Sougrat, R., Lindwasser, O. W., Olenych, S., Bonifacino, J. S., Davidson, M. W., Lippincott-Schwartz, J., and

Hess, H. F. (2006). Imaging intracellular fluorescent proteins at nanometer resolution. *Science Express*, pages 1–5.

[Bock et al., 2007] Bock, H., Geisler, C., Wurm, C. A., von Middendorff, C., Jakobs, S., Schönle, A., Egner, A., Hell, S. W., and Eggeling, C. (2007). Two-color far-field fluorescence nanoscopy based on photoswitchable emitters. *Applied Physics*, B88:161–165.

[Boron and Boulpaep, 2005] Boron, W. F. and Boulpaep, E. L. (2005). *Medical Physiology*. Elsevier Saunders.

[Bossi et al., 2008] Bossi, M., Fölling, J., Belov, V. N., Boyarskiy, V. P., Medda, R., Egner, A., Eggeling, C., Schönle, A., and Hell, S. W. (2008). Multicolor far-field fluorescence nanoscopy through isolated detection of distinct molecular species. *Biophysical Journal: Biophysical Letters*, 8 (8):2463–2468.

[Bundesamt, 2009] Bundesamt, S. (2009). Todesursachen in deutschland.

[Cummings, 2009] Cummings, B. (2009). Pearson education.

[Davidson, 2009] Davidson, M. W. (2009). Molecular expressions: Optical microscopy primer.

[Demtröder, 2004] Demtröder, W. (2004). *Experimentalphysik 2: Elektrizität und Optik*. Springer, 3 edition.

[Denk et al., 1990] Denk, W., Strickler, J., and WW., W. (1990). Two-photon laser scanning fluorescence microscopy. *Science*, 248(4951):73–76.

[Fölling et al., 2008] Fölling, J., Bossi, M., Bock, H., Medda, R., Wurm, C. A., Hein, B., Jakobs, S., Eggeling, C., and Hell, S. W. (2008). Fluorescence nanoscopy by ground-state depletion and single-molecule return. *Nature Methods*, 5(11):943–945.

[Gustafsson, 2000] Gustafsson (2000). Surpassing the lateral resolution limit by a factor of two using structured illumination microscopy. *Microscopy Journal*, 198:82–87.

[Gustafsson, 2005] Gustafsson, M. G. L. (2005). Nonlinear structured-illumination microscopy: Wide-field fluorescence imaging with theoretically unlimited resolution. *PNAS: Proceedings of the National Academy of Sciences*, 102:13081–13086.

[HDF5Group, 2009] HDF5Group (2009). Hdf5group.

[Hecht, 1998] Hecht, E. (1998). *Optics*. Third edition.

[Heilemann et al., 2008] Heilemann, M., van de Linde, S., Schüttelpelz, M., Kasper, R., Seefeldt, B., Mukherjee, A., Tinnefeld, P., and Sauer, M. (2008). Subdiffraction-resolution fluorescence imaging with conventional fluorescent probes. *Angewandte Chemie*, 47:6172–6176.

[Heintzmann et al., 2002] Heintzmann, R., Jovin, T. M., and Cremer, C. (2002). Saturated patterned excitation microscopy-a concept for optical resolution improvement. *Optical Society of America*, 19:1599–1609.

[Hell and Stelzer, 1992a] Hell, S. and Stelzer, E. H. K. (1992a). Fundamental improvement of resolution with a 4pi-confocal fluorescence microscope using 2-photon excitation. *Optics Communications*, 93:277–282.

[Hell and Stelzer, 1992b] Hell, S. and Stelzer, E. H. K. (1992b). Properties of a 4pi confocal fluorescence microscope. *JOURNAL OF THE OPTICAL SOCIETY OF AMERICA A-OPTICS IMAGE SCIENCE AND VISION*, 9(12):2159–2166.

[Hell and Wichmann, 1994] Hell, S. and Wichmann, J. (1994). Breaking the diffraction resolution limit by stimulated-emission - stimulated-emission-depletion fluorescence microscopy. *OPTICS LETTERS*, 19:780–782.

[Hell, 2007] Hell, S. W. (2007). Far-field optical nanoscopy. *Science*, 316:1153–1158.

[Hess et al., 2006] Hess, S. T., Girirajan, T. P. K., and Mason, M. D. (2006). Ultra-high resolution imaging by fluorescence photoactivation localization microscopy (fpalm). *Biophysical Journal*, pages 1–24.

[Huang et al., 2008] Huang, B., Wang, W., Bates, M., and Zhuang, X. (2008). Three-dimensional super-resolution imaging by stochastic optical reconstruction microscopy. *Science*, 319:810 – 813.

[Invitrogen, 2008] Invitrogen (2008). *Fluorescent Spectraviewer Invitrogen*. http://www.invitrogen.com/site/us/en/home/support/Research-Tools/Fluorescence-SpectraViewer.html.

[Jayasinghe et al., 2009] Jayasinghe, I. D., Cannell, M. B., and Soeller, C. (2009). Organization of ryanodine receptors, transverse tubules and sodium-calcium exchanger in rat myocytes. *Biophysical Journal*, 97:1–10.

[Kittel, 2006] Kittel, C. (2006). *Einführung in die Festkörperphysik*. 14. edition.

[Klar et al., 2000] Klar, T., Jakobs, S., Dyba, M., Egner, A., and Hell, S. (2000). Fluorescence microscopy with diffraction resolution barrier broken by stimulated emission. *PNAS: Proceedings of the National Academy of Sciences*, 97:8206–8210.

[Kong, 2007] Kong, C. H. T. (2007). High-resolution imaging and detection of calcium sparks in the heart. Master's thesis, School of Medical and Health Science.

[Koster and Klumperman, 2003] Koster, A. and Klumperman, J. (2003). Electron microscopy in cell biology: integrating structure and function. *Nature Review Molecular Cell Biology*.

[Lakowicz, 2006] Lakowicz, J. R. (2006). *Principles of Fluorescence Spectroscopy*. Springer, third edition.

[Lemmer et al., 2008] Lemmer, P., Gunkel, M., Baddeley, D., Kaufmann, R., Urich, A., Weiland, Y., Reymann, J., Müller, P., Hausmann, M., and Cremer, C. (2008). Spdm: light microscopy with single-molecule resolution at the nanoscale. *Applied Physics B: Laser and Optics*, 93:1–12.

[Levenberg, 1944] Levenberg, K. (1944). A method for the solution of certain problems in least squares. *Quart. Appl. Math.*, 2:164–168.

[Levsky and Singer, 2003] Levsky, J. M. and Singer, R. H. (2003). Fluorescence in situ hybridization: past, present and future. *Journal of Cell Science*, 116:2833–2838.

[Lipp et al., 1996] Lipp, P., J.Huser, L.Pott, and Niggli, E. (1996). Spatially non-uniform ca2+ signals induced by the reduction of transverse tubules in citrate-loaded guinea-pig ventricular myocytes in culture. *Jounal of Physiology*, 497:589–597.

[Marquardt, 1963] Marquardt, D. (1963). An algorithm for least-squares estimation of nonlinear parameters. *Journal of the Society for Indurstrial and Applied Mathematics*, 11:431–441.

[Marton, 1934] Marton, L. (1934). Electron microscopy of biological objects. *PHYSICAL REVIEW*, 46:0527–0528.

[Melan, 1995] Melan, M. A. (1995). *Methods in Molecular Biology: Immunocytochemical Methods and Protocols Overview of Cell Fixation and Permeabilization*, chapter 8. Lorette C. Javois.

[Müller-Erstel, 2004] Müller-Erstel, W. (2004). *Biochemie: Eine Einführung für Mediziner und Naturwissenschaftler*. Springer.

[Nikon, 2004] Nikon (2004). Nikon eclipse te2000.

[Nikon, 2009] Nikon (2009). Nikon microscopyu.

[PythonSoftwareFoundation, 2009] PythonSoftwareFoundation (2009). Python Programming Language–Official Website.

[Robbins and Hadwen, 2002] Robbins, M. S. and Hadwen, B. J. (2002). The noise performance of electron multiplying charge coupled devices. *IEEE Transactions on Electron Devices*.

[Rust et al., 2006] Rust, M. J., Bates, M., and Zhuang, X. (2006). Sub-diffraction-limit imaging by stochastic optical reconstruction microscopy (storm). *Nature Methods*, 3(10):793–795.

[Scipy, 2009] Scipy (2009).

[Steinhauer et al., 2008] Steinhauer, C., Forthmann, C., Vogelsang, J., and Tinnefeld, P. (2008). Superresolution microscopy on the basis of engineered dark states. *Journal of the American Chemical Society*, 130 (50):16840–16841.

[Thompson et al., 2002] Thompson, R. E., Larson, D. R., and Webb, W. W. (2002). Precise nanometer localization analysis for individual fluorescent probes. *Biophysical Journal*, 82:2775–2783.

[Vogelsang et al., 2008] Vogelsang, J., Kasper, R., Steinhauer, C., Person, B., Heilemann, M., Sauer, M., and Tinnefeld, P. (2008). A reducing and oxidizing system minimizes photobleaching and blinking of fluorescent dyes. *Angewandte Chemie*, 47:5465–5469.

[WHO, 2009] WHO (2009). World health statistics 2009.

[Wikipedia, 2009] Wikipedia (2009).

[Wilhelm et al.,] Wilhelm, S., Gröbler, B., Gluch, M., and (all Carl Zeiss Jena), H. H. *Die konfokale Laser Scanning Mikroskopie: Grundlagen.*

Acknowledgements

184 slides, 22563.94 air miles, lots of sleepless nights, thousands of cells, millions of antibodies and a infinite number of photons later, this thesis is finally done:

Therefore I would like to thank all those who made this thesis possible:

I have to thank **Prof. Dr. Dr. Christoph Cremer**, head of the applied optics and information processing research group (KIP, University of Heidelberg), for supporting an international designed diploma thesis and for encouraging collaborations in research.
Special thanks to **Associate Prof. Dr. Christian Soeller** (University of Auckland), my direct supervisor, who provided good teaching and supervision, as well as guidance and encouragement.
Thanks to **Prof. Dr. Mark B. Cannell**, head of the Biophysics and Biophotonics Research Group (Physiology, University of Auckland) for the opportunity to be part in his research group. Special thanks also to **Dr. David Baddeley** (University of Auckland) for all the thousands and thousands very good illustrated explanations, all the teaching in programming with python and for proofreading this thesis.
I want to thank my lab mates **Isuru Dilshan** for teaching fixing cells and sharing his labeling skills and **Cherrie Kong**, who provided the cells for all experiments. Many thanks to the whole **Biophysics and Biophotonics Group** (University of Auckland) for having taken me up in your group, the good food in our lab-meetings and for all the fun during work.

Lots and lots of thanks to my fellow sufferer and best friends **Julia** and **Maria** for all the great time either spending hours with our physics books at the swimming pool or studying through all the long nights before our exams.
Especially I would like to thank my parents **Claudia** and **Jörg**, who supported me

in every possible way. All your encouragement and support made this thesis possible in the first place. Also thanks to the rest of my family and friends, who supported me during my studies. Thank you **Sally** and **Dougal** for helping me out in so many ways and for always feeling welcome!!!
Special thanks to **Nico**, who helped me through all good and especially through all hard times during my studies. And lastly I would like to thank **Steffen**: Just thanks for everything, for always being there when needed and for all the laughs, which helped me through the good times as well as through the bad times!!!

Nothing is impossible! (All Blacks)

Erklärung:

Ich versichere, dass ich diese Arbeit selbstständig verfasst habe und keine anderen als die angegebenen Quellen und Hilfsmittel benutzt habe.

Heidelberg, den ....

(Sabrina Roßberger)